NTNU

Norwegian University of
Science and Technology

Structural loads on a free-falling lifeboat

Simen Groth

Marine Technology
Submission date: June 2017
Supervisor: Marilena Greco, IMT
Co-supervisor: Sebastien Fouques, Sintef
Andrea Califano, DNV-GL

Norwegian University of Science and Technology
Department of Marine Technology

MASTER THESIS IN MARINE TECHNOLOGY

Spring 2017

FOR

Simen Groth

Structural loads on a free-falling lifeboat

(Strukturelle belastninger på et fritt fall livbåt)

Free-fall lifeboats represent a good alternative to conventional, davit launched, lifeboats (lowered to sea by means of cables) because they require shorter time for launching and can have more momentum for escaping the host ship/platform. The different phases of their evolution have been investigated during the project thesis with focus on the water-entry and later stages. A simplified body geometry was modelled numerically and studied with a selected CFD commercial solver assuming calm-water conditions and incompressible air.

The project activity was carried out together with two other master students. The master thesis will be individually carried out but with some shared investigations.

Objective

Present master thesis aims to continue the numerical investigations started during the project thesis focusing on the possible structural consequences induced by the fluid-lifeboat interactions during water-entry and later stages.

The work should be carried out in steps as follows:

1. Summarize major findings/outcomes from the project thesis and investigate possible reasons for questions left open. The latter part will be carried out in collaboration with the other two students working on the same simplified lifeboat concept.
2. Complement the literature study of the project with state-of-the-art works on numerical/experimental/theoretical studies of structural-loads and fluid-structure interaction problems relevant for the topic of interest.
3. Use the simplified lifeboat geometry studied during the project thesis and perform a systematic numerical study on the relevant parameters connected with initial conditions, assuming calm water and incompressible air, and using the CFD solver selected in the project work.
4. Using findings from the literature study performed in step 2, select an available structural solver to be used for the structural analysis of the lifeboat with hydrodynamic loads from the CFD solver used in the project. At least one of the two following conditions should be examined: a) during the initial slamming phase and b) during and after the pinch off time of the cavity in the aft part of the body. For these studies assumes no hydroelasticity excitation and study the structural response with a quasi-static approach but try also to assess possible occurrence of hydroelasticity.
5. Investigate the structural consequences in one basic test case and the sensitivity to modified initial conditions and considering (A) air compressibility effects at least in one relevant case and (B) presence of incident waves at least in one relevant case (using for A and B hydrodynamic simulations from the studies of the two other students).

The work may show to be more extensive than anticipated. Some topics may therefore be left out after discussion with the supervisor without any negative influence on the grading.

The candidate should in his report give a personal contribution to the solution of the problem formulated in this text. All assumptions and conclusions must be supported by mathematical models and/or references to physical effects in a logical manner.

The candidate should apply all available sources to find relevant literature and information on the actual problem.

The thesis should be organised in a rational manner to give a clear presentation of the work in terms of exposition of results, assessments, and conclusions. It is important that the text is well written and that tables and figures are used to support the verbal presentation. The thesis should be complete, but still as short as possible. In particular, the text should be brief and to the point, with a clear language. Telegraphic language should be avoided.

The thesis must contain the following elements: the text defining the scope (i.e. this text), preface (outlining project-work steps and acknowledgements), abstract (providing the summary), table of contents, main body of thesis, conclusions with recommendations for further work, list of symbols and acronyms, references and (optional) appendices. All figures, tables and equations shall be numerated.

The supervisor may require that the candidate, in an early stage of the work, present a written plan for the completion of the work. The plan should include budget for the use of computer and laboratory resources that will be charged to the department. Overruns shall be reported to the supervisor.

From the thesis it should be possible to identify the work carried out by the candidate and what has been found in the available literature. It is important to give references to the original source for theories and experimental results.

Supervisor : Marilena Greco

Co-supervisor : Andrea Califano

Co-supervisor : Ole Hermundstad

Submitted :15 January 2017

Deadline :25 June 2017

Marilena Greco

Supervisor

Abstract

Free-falling lifeboats are a method of escaping hazardous events in open sea. They rest at a skid until released and launched into the water. It is important that the use of free-falling lifeboats ensure a safe evacuation. In this master thesis, a simplified free-falling lifeboat geometry has been used to investigate the physical phenomena connected with this evacuation method.

The hydrodynamic results are obtained with a computational fluid dynamics (CFD) program, Star-CCM+, and the structural results from a finite element method (FEM) program, Abaqus. There has been conducted a sensitivity and convergence study of the CFD simulations, and a convergence check for the FEM model.

The lifeboat has been solved with seven different parameters under the assumption that the air is incompressible, where the main initial conditions were a water entry angle of 60 degrees, a velocity of 20,61 m/s and with centre of gravity -0.5 m in z_{body}-direction from the body centreline. These initial conditions have been changed with $\pm$ 5 degrees for the water entry angle, $\pm$ 5 m/s for the body fixed velocity and $\pm$ 0.2 m for the centre of gravity. For the structural assessment only the initial conditions have been used, but with four load cases. One load case where only inputs to Abaqus from Star-CCM+ for the aft is established (one-way coupling) with air modelled as incompressible. Two load cases where inputs are given to both of the programs (two-way coupling) for the hull and aft, with air as incompressible. The fourth load case is the same as the first load case, but with air modelled as compressible.

Results from the initial conditions shows that the lifeboat experiences the same physical phenomena as a real lifeboat. It experiences an air cavity closure on the aft and it follows the preferred trajectory suggested by DNV-GL. For the parameter investigation, it was shown that the change in water entry velocity gave the largest difference on most of the results, with respect to the initial conditions. This includes a variation of the air cavity closure time and peak magnitude, and water exit time. The change in water entry angle gave the largest change in maximum submersion compared with the initial conditions. The difference in maximum submersion created also a larger pressure on the aft, due to the hydrostatic pressure. The change in COG_z did not create much differences on the results.

When using a one-way coupling simulation, with air modelled as incompressible, the structural results were unrealistic. Where all the different shell thicknesses exceeded yield and ultimate

strength. It was found that hydroelastic effects matter for this load case. With the two-way coupling, for the aft, the results were almost the same. Due to a coarser mesh discretization in the CFD simulations with the two-way coupling, the results from one-way and two-way coupling are not comparable. When the air was modelled as compressible the response from the aft with a shell thickness of 20 mm was found to be quasi-static. With this thickness, the aft was also able to withstand the stresses from the air cavity closure and the air bubbles oscillations.

When using the hull in the two-way coupling it was seen that the splash crown had the largest influence on the stresses on the lifeboat. Here the 20 mm, 10 mm and 5 mm shell thickness were able to withstand these stresses without going into the plastic zone, while a shell thickness of 2.5 mm exceeded the Tresca yield criterion. It was also found that the solution obtained was of a quasi-static approach.

Sammendrag

Fritt fallende livbåter er en metode for å evakuere fra farlige hendelser på havet. De ligger på en rampe inntil de blir frigjort og skytes ut i vannet. Det er viktig at bruken av fritt fallende livbåter gir en sikker evakuering. I denne masteroppgaven har en forenklet livbåt geometri blitt brukt til å undersøke de fysiske fenomenene knyttet til denne evakuerings metoden.

De hydrodynamiske kreftene er oppnådd med et dataprogram som regner ut fluidets dynamikk (CFD), Star-CCM+, og konstruksjonsresultater er oppnådd med et program som regner ut konstruksjonens respons ved hjelp av elementmetoden (FEM), Abaqus. Det har blitt gjennomført en følsomhets- og konvergensstudie av CFD-simuleringene, og en konvergenskontroll av FEM-modellen.

Livbåten har blitt gitt syv forskjellige parametere under antagelsen at luften ikke kan komprimeres, der startbetingelsene var en vanninngangsvinkel på 60 grader, en hastighet på 20.61 m/s og med tyngdepunktet -0.5 m i z_{kropp} retning fra livbåten midtlinje. Disse parameterne ble endret med $\pm$ 5 grader for vanninngangsvinkel, $\pm$ 5 m/s i hastighet og $\pm$ 0.2 m i tyngdepunkt. For konstruksjonsdelen er bare startbetingelsene blitt brukt, men med fire forskjellige belastninger. En belastning hvor bare Abaqus får verdier fra Star-CCM+ for akter (en enveiskobling), med luft modellert som ikke-kompressibel. To belastninger hvor Abaqus og Star-CCM+ får verdier fra hverandre (en toveiskobling), både for baksiden og for skroget. En siste belastning på lik linje som første (enveiskobling), men hvor luften er modellert som kompressibel.

Resultatene fra startbetingelsene viser at livbåten oppnår de samme fysiske fenomenene som en ekte livbåt. Den får en luftboble på baksiden, og den følger den foretrukne banen utviklet av DNV-GL. For parameterundersøkelsen ble det vist at endringen i vanninngangshastighet har mest å si på resultatene, med hensyn til start betingelsene. Dette inkluderer en variasjon av tiden hvor luftboblen kollapser og størrelsen på verdien, og vannutgangstiden. Endringen i vanninngangsvinkelen ga den største forandringen i maksimal neddykking sammenlignet med start forholdene. Forskjellen i maksimal neddykking skapte også et større trykk på baksiden, på grunn av hydrostatisk trykk. Endringen i tyngdepunktet skapte liten forskjell på resultatene.

Ved bruk av enveiskobling mellom Star-CCM+ og Abaqus, med luft som ikke-kompressibel, er konstruksjons resultater urealistiske. Hvor alle skalltykkelser overstiger flytespenningen og maksimal flytespenning. Med denne belastningen var det funnet at hydroelastiske effekter var av betydning.

Med toveiskoblingen, for akter, ble resultatene veldig lik. På grunn av en grovere celleinndeling i CFD simuleringene med toveiskoblingen, var ikke resultatene mellom enveis- og toveiskoblingen sammenlignbare. Når luften var modellert som kompressibel var responsen fra akter, med en skalltykkelse på 20 med mer, kvasi-statisk. Med denne tykkelsen klarte den aktre delen å motstå kreftene fra luft boblens kollaps, og dens svingninger.

Når skroget ble brukt i en toveiskobling ble det sett at det var vann spruten som hadde størst effekt på spenningene på livbåten. Her klart skalltykkelsene 20 mm, 10 mm og 5 mm å motstå denne spenningen uten å gå inn i den plastiske sonen, mens for en skalltykkelse på 2.5 mm Tresca kriteriet var overskredet. Det var funnet ut at løsningen var av kvasi-statisk form.

Preface / Acknowledgements

This thesis is a result of the individual, and collaborated, work required for fulfilment of the degree Master of Science, Marine Structures.

One part of this thesis is written with fellow co-students Vegard Netland and Andreas Svendsen. We wrote the specialization project “Hydrodynamic effects relevant for free-falling lifeboats, a preliminary study” together in the fall 2016. Since none of us had experience with CFD-analysis before the fall of 2016, there was a steep learning curve, and some crucial mistakes were made. One part of the objective of the master thesis is therefore to re-do the specialization project, which results in a common part, sections 2 - 7. This is of agreement with our main supervisor Professor Marilena Greco.

The individual part consists of the structural loads from the initial condition results from the common part, as well as a theory and description of how the work has been conducted. For the individual part, it is assumed that the reader is familiar with most of the procedures in Finite Element Method, such that most of these equations will not be described.

I am very grateful to my main supervisor, Professor Marilena Greco, for her guidance, knowledge and her willingness to always help. She has provided co-supervisors with valuable knowledge on the topic, Andrea Califano (DNV-GL), Sèbastien Fouques (SINTEF) and Ole Andreas Hermundstad (SINTEF). I would like to thank them all for their guidance and help. I will also thank Guomin Ji (SINTEF) for all the help in Abaqus.

At last I would like to thank family and friends for making my time at NTNU Trondheim as pleasant and fun as possible. As well as Vegard Netland and Andreas Svendsen for useful insights in the individual part, thank you for your contribution.

Trondheim, 25/06/2017

Simen Groth

List of content

1 Introduction 1

2 Introduction to free-falling lifeboat phases and physics 2

2.1 Launching phase 2

2.2 Free-falling phase 4

2.3 Water entry phase 5

2.3.1 Slamming 6

2.3.1.1 Simplified calculation approach 6

2.3.1.2 Slamming calculations for free-falling lifeboats 9

2.3.1.3 Hydroelasticity 10

2.3.2 Parameters defining the water entry 10

2.4 Submerged phase 12

2.4.1 Air cavity formation 13

2.4.2 Cavity classifications 13

2.4.3 Physical insight 14

2.4.4 Capillary waves evolution in the air cavity water surface 16

2.5 Water exit phase 17

2.6 Sail away phase 19

2.7 Motion patterns 19

2.7.1 Log dive 20

2.8 Occupant safety 21

3 Computational fluid dynamics 23

3.1 Governing equations in CFD 23

3.2 Previous work with the use of CFD for free-falling lifeboats analysis 25

3.2.1 Validation of CFD with experiments 25

3.2.2 Free-falling lifeboats in waves 26

3.2.3 CFD simulations for structural assessment 26

3.2.4 Sail away phase 28

3.3 Star-CCM+ 28

3.3.1 Physics 29

3.3.1.1 Transport equation 29

3.3.1.2 Turbulence models 30

3.3.1.2.4 Reynolds stress transported model 31

3.3.2 Free boundaries approximations 31

3.3.2.1 Volume of fluid method 31

3.3.3 Wall Y^+ 32

3.3.4 Courant Friedrichs Lewy Number 34

3.4 High Performance Computers 35

4 Pre-Processing 37

4.1 Geometry 37

4.2 Boundary conditions 38

4.3 Mesh configurations 40

4.4 Applied physics 42

5 Sensitivity & Convergence 45

5.1 Sensitivity Analysis 45

5.1.1 Residuals 45

5.1.2 Number of iterations 47

5.1.3 CFL number analysis 49

5.2 Convergence Study 51

6 Results with initial conditions 57

6.1 Acceleration and angular acceleration 58

6.1.1 Water entry 59

6.1.2 Air cavity formations 59

6.1.3 Submerged phase after air cavity formation 61

6.1.4 Water exit 61

6.1.5 Sail away phase 61

6.2 Velocity 62

6.3 Motion 63

6.4 Pressure aft 63

6.5 Comparison with theory 65

6.5.1 Air cavity investigation 65

6.5.2 Water exit 66

6.6 Courant validation 67

7 Parameter investigation 69

7.1 Velocity 69

7.2 Water entry angle 71

7.3 COG 73

7.4 Conclusion/ Discussion for the parameter investigation 75

8 Finite Element Method 76

8.1 FEM introduction 76

8.2 Abaqus 77

8.2.1 Modelling 77

8.2.2 Beam element 79

8.2.3 Shell element 81

8.3 System properties 81

8.3.1 Coordinate systems used 83

8.4 FEM convergence study 83

8.5 Eigenmodes of the structure 87

9 Fluid-Structure-Interaction 90

9.1 Communication between CFD and FEM 90

9.1.1 FSI interaction between Star-CCM+ and Abaqus 90

9.2 Criterions and assumptions 92

9.2.1 FEM solving method 92

9.2.2 Response and hydroelastic effects 93

9.2.3 Boundary conditions 95

9.2.4 Von-Mises and Tresca 96

9.2.5 Air modelled as compressible 98

10 Loads on the aft with incompressible air and one-way coupling 99

10.1 Validation of the forces and solver 99

10.2 Stresses 101

10.3 Displacements 102

11 Loads on the aft with incompressible air and two-way coupling 107

11.1 Validation of forces and displacements 107

11.2 Path 109

11.3 Pressure 110

11.4 Acceleration 110

11.5 Stresses 111

12 Loads on the hull with incompressible air and two-way coupling 113

12.1 Validation of displacements and solver 113

12.2 Path 115

12.3 Pressure 115

12.4 Accelerations 116

12.5 Stresses 117

12.6 Displacements 119

13 Loads on the aft with compressible air effects and one-way coupling 121

13.1 Compressible air properties 121

13.2 Validation of forces and solver 122

13.3 Stresses 125

13.4 Displacements 127

14 Error sources 129

15 Conclusions and discussion 130

16 Further work 133

Appendix 138

List of figures

Figure 2.1: Shows the lifeboat on a launch skid, as the center of gravity passes the end of the launch skid. 3

Figure 2.2: Shows a free-falling lifeboat in the free-falling phase. This is a Norsafe AS production, one of the leading lifeboat producers. (Consultance, 2017) 4

Figure 2.3: Wind conditions (DNV-GL, 2010) 5

Figure 2.4: Shows how the different parameters are defined in the analysis of impact forces and pressure on a body. 7

Figure 2.5: Shows the difference in splash crown formation for a hydrophilic and a hydrophobic case (Truscott, et al., 2013) 10

Figure 2.6: Visualization of different water entry events (Truscott, et al., 2013) 14

Figure 2.7: Trajectory dependent on released depth for ping-pong balls (Truscott, et al., 2016) 17

Figure 2.8: Motion patterns for a free-falling lifeboat 19

Figure 2.9: $x\ is\ the\ horizontal\ velocity\ of\ the\ lifeboat\ and\ vx'$ is the sum of the horizontal and the vertical velocity components in the direction of motion. (DNV-GL, 2016) 20

Figure 2.10: The local seat coordinate system (DNV-GL, 2016) 21

Figure 3.1: Location of force panels, P1 (hull bottom fore), P2 (roof top – fore), P3 (hull bottom aft) and P4 (Stern/back door) (Fouques & Hermundstad, 2016) 26

Figure 3.2: Pressure time series for P1, P3 and P4 (Fouques & Hermundstad, 2016) 27

Figure 3.3: Correlation between $Y+$ and $u+$ (Steve CD adapco, 2016) 33

Figure 4.1: Simplified geometry 37

Figure 4.2: Visualization of the coordinate systems, a) is the global coordinate system and b) is the body fixed 38

Figure 4.3: Boundary conditions illustration 39

Figure 4.4: Mesh 41

Figure 4.5: Prism layer illustration on the corner, cut-out A-1 from Figure 4.4 42

Figure 4.6: Refined mesh on aft part inside the overset 42

Figure 4.7: Main applied physics in the simulations 43

Figure 4.8: In the aft part of the body, air is still entrapped after 1.05 seconds, though the body is fully submerged, results in $Y+$values below 30. 43

Figure 5.1: Residuals for the whole simulation with Δt =1.2ms and 10 inner iterations. 46

Figure 5.2: Residuals for the complete simulation with Δt=0.6ms and 10 inner iterations 46

Figure 5.3: VOF picture approximately from where the turbulence model starts to diverge for larger time steps, even though the time steps are relatively small 47

Figure 5.4: Residuals where the iterations for each time step is showed 48

Figure 5.5: Residuals for one time step 48

Figure 5.6: CFL values for free surface interaction, where blue is for Δt=1.2ms and red is for Δt=0.6ms 49

Figure 5.7: Courant scene for a global view at the end of water entry phase 50

Figure 5.8: Local Courant scene from cut A-1 in Figure 5.7 50

Figure 5.9: Global Courant scene right before cavity closure 51

Figure 5.10: Local Courant scene right before cavity closure, cut B-1 from Figure 5.9 51

Figure 5.11: Mesh with 0,16 m as smallest cell, discretization $\Delta x3$ 52

Figure 5.12: Mesh with 0,08 m as smallest cell, discretization $\Delta x2$ 53

Figure 5.13: Mesh with 0,04 m as smallest cell, discretization $\Delta x1$ 53

Figure 5.14: Convergence plots, where yellow is the time instance of 0.22 s – 0.75 s, blue 0.985 s – 1.0125 s and purple 1.4 s – 2.4 s 55

Figure 6.1: VOF of air representation of the path from water entry to sail away 58

Figure 6.2: Acceleration and angular acceleration measured in the body fixed coordinate system 58

Figure 6.3: Beginning of the air cavity closure, 2-D, starting from solution time 0.756s with $\Delta t = 0.025s$, until 0.882s 60

Figure 6.4: Visualization of the air cavity closure in 3D where a) shows the solution time 1.002 s and b) shows solution time 1.102 s 60

Figure 6.5: Velocity plot where the red is in the x_{body} -direction and blue in z_{body} -direction 62

Figure 6.6: Position plot, where the red line is in the x-direction, blue in the z-direction and the green in y-direction 63

Figure 6.7: Pressure plots on the aft part 64

Figure 6.8: Pressure distribution on the lifeboat 7ms before the peak 64

Figure 6.9: Minimum pressures from the splash crown, where a) shows the global and b) more locally of the same time instance 65

Figure 6.10: CFL number throughout the simulation 67

Figure 6.11: CFL visualization 68

Figure 7.1: Green is 15.62 m/s, red is IC with maximum velocity 20.62 m/s and blue is 25.62 m/s. The accelerations and velocities are taken in the body fixed coordinate system. The dashed lines are in the x-direction, and the solid lines are in the z-direction in the velocity and position plots. 70

Figure 7.2: Plots of the results with different water entry angles, where blue is 55°, red is 60° and green is 65°. The accelerations and velocities are taken in the body fixed coordinate system. The dashed lines are in the x-direction, and the solid lines are in the z-direction for the velocity and position plots. 71

Figure 7.3: a) shows a picture of water entry angle 55° and b) shows a picture of water entry angle 65° at 0.9324s 73

Figure 7.4: Result plots with different centre of gravity in z-direction, where blue is -0.3m, red is -0.5m and green is -0.7m. The accelerations and velocities are taken in the body fixed coordinate system. The dashed lines are in the x-direction, and the solid lines are in the z-direction for the velocity and position plots. 74

Figure 8.1: Abaqus model of the geometry, shell (hull and aft) labelled as red, ring stiffeners as white and bottom stiffeners as green 78

Figure 8.2: Example of local axis definition for beam-type elements (Simulia - Abaqus 6.14, 2014) 80

Figure 8.3: Distribution of the mass and moments to ensure same properties in both programs, where green is the point masses and moments applied and orange is the non-structural mass 82

Figure 8.4: Coordinate systems in Abaqus, where a) is the origin and b) is located on the aft 83

Figure 8.5: Mesh discretization $\Delta x2FEM$, where a) is of hull, b) only of the aft, c) the location of two poor elements in the fore part of the hull and d) zoomed in on the poor elements (A-1 from c)) 84

Figure 8.6: Pressure plots from CFD $\Delta x2$, where red is unfiltered and blue is filtered 85

Figure 8.7: Max displacement versus number of elements on the aft with the applied pressure from Figure 8.6, blue dots are the results 86

Figure 8.8: Max displacement on the hull versus number of elements on the hull with the applied pressure from Figure 8.6, blue dots are the results 87

Figure 8.9: Visualization of the 20 mm eigenmodes listed in Table 8.6, the behaviour is equal for all thicknesses, where a) is connected to eigenmode 1, b) is connected to 2, c) is connected to 3, d) is connected to 4 and e) is connected to 5 89

Figure 9.1: Mapping interpolation option Least Squares method 91

Figure 9.2: The response in the structure as a proportional to the ratio of T_d over T_n (Faltinsen, 2005) 95

Figure 9.3: Concentrated forces (CF) from Star-CCM+ to Abaqus 96

Figure 9.4: Von Mises and Tresca criterion (Case, et al., 1999) 97

Figure 10.1: Total force from Star-CCM+ vs total force from Abaqus on the aft 100

Figure 10.2: External work versus external work minus kinetic energy for the quasi-static solver check, when air is modelled as incompressible 100

Figure 10.3: Plots of average and maximum Tresca and von-Mises stress on the aft 101

Figure 10.4: Shows the von-Mises stress on the aft with shell thickness 20 mm and a deformation scale factor of 20, where the grey area is above the ultimate strength and a) shows Δt = 1.023 s and b) shows Δt = 1.095 s 102

Figure 10.5: Nodes used for displacements a) Location of the four nodes b) zoomed in on the nodes 103

Figure 10.6: Displacement of all the nodes on the aft part at $\Delta t = 1.095\ s$, where node 8759 excites the largest deformation 103

Figure 10.7: Displacement for nodes 8726, 8741, 8757 and 8759 for all shell thicknesses where the values are taken in the $znodes$-direction 104

Figure 10.8: Shows the displacements of the shell thickness 20 mm with a deformation scale factor of 20, where the time instance of a) is 1.023 s and b) is 1,044 s 105

Figure 10.9: Maximum response by equation [48] versus Abaqus results, where the Abaqus results are superimposed such that the maximum response from both methods are in phase. This is done for a shell thickness of 20 mm. 106

Figure 11.1: Force, taken as magnitude, on the aft with two-way coupling 108

Figure 11.2: Maximum displacement magnitude of the aft, where Star-CCM+ has used n_{global} coordinate system and Abaqus n_{origin} coordinate system 108

Figure 11.3: Position from Star-CCM+ with two-way coupling 109

Figure 11.4: Average pressure from Star-CCM+ with two-way coupling 110

Figure 11.5: Acceleration from Star-CCM+ with two-way coupling 111

Figure 11.6: Plots of average and maximum Tresca and von-Mises stress on the aft with two-way coupling 112

Figure 12.1: Star-CCM+ forces mapped to Abaqus for all shell thicknesses, plot values obtained only from Abaqus 113

Figure 12.2: Maximum displacements for all shell thicknesses, where Star-CCM+ has used coordinate system n_{global} and Abaqus n_{origin}. The Star-CCM+ displacements for shell thickness of 5 mm is not included 114

Figure 12.3: External work versus external work minus kinetic energy for the quasi-static solver check for hull, when air is modelled as incompressible 114

Figure 12.4: Position from Star-CCM+ of the lifeboat with two-way coupling when Abaqus solves for the hull 115

Figure 12.5: Average pressure from Star-CCM+ on the hull with the solution from the two-way coupling, when Abaqus solves for the hull. Shell thickness 5 mm is not included 116

Figure 12.6: Accelerations from Star-CCM+ with two-way coupling, when Abaqus solves for the hull. Shell thickness 5 mm is not included 117

Figure 12.7: Average and maximum von-Mises and Tresca stress on the hull, where yellow is the yield stress and purple is the ultimate stress 118

Figure 12.8: Location of maximum Tresca stress at Δt = 0.36 s 118

Figure 12.9: Cut A-1 from Figure 12.8, where the grey area is the area which exceeds ultimate strength 119

Figure 12.10: The red circle shows the location of the nodes where maximum displacements for the hull are 120

Figure 13.1: None dimensional pressure peaks plotted log linear against none dimensional period for polytrophic condition (Svendsen, 2017) 122

Figure 13.2: Total force on the aft part with compressible air, Star-CCM+ versus Abaqus 123

Figure 13.3: External work versus external work minus kinetic energy for the quasi-static solver check, when air is modelled as compressible 124

Figure 13.4: Von-Mises and Tresca stress on the aft when the air is modelled as compressible 125

Figure 13.5: Stresses on the aft with a deformation scale of 20, where the grey area is above the ultimate strength, a) shows von-Mises stress at Δt = 1.362 s, b) shows von-Mises stress at Δt = 1.635 s, c) shows Tresca stress at Δt = 1.362 s, and d) shows Tresca stress at Δt = 1.635 s 126

Figure 13.6: Displacements of node 8726, 8741, 8757 and 8759 for shell thickness 20 mm, 10 mm and 5 mm in z_{nodes} - direction 127

Figure 13.7: Shows the difference in the air bubble on the aft at solution time 1.3608 s where a) is with the air modelled as compressible and b) is the air is modelled as incompressible 128

List of tables

Table 4.1: Simplified geometry properties taken from the body fixed coordinate system 38

Table 4.2: Dimensions for each part in the simulation, where Overlap Overset, Overset and Box Behind is measured in the body fixed coordinate system, while the rest of the parts in the global coordinate system 39

Table 5.1: Mesh description, where the cell sizes from the prism layer is excluded as smallest cell 52

Table 5.2: Prism layer specification for each mesh discretization 52

Table 5.3: Order of accuracy for different integrals and points for selected time intervals and point of time. 55

Table 5.4: Mesh discretization with its specific solving time, number of processors used and computational cost 56

Table 6.1: Initial conditions 57

Table 7.1: Parameter investigation values 69

Table 7.2: Distinctive values for comparison the change in water entry velocity 70

Table 7.3: Distinctive values for comparison for a change in water entry angle 72

Table 7.4: Distinctive values for comparison of a change in centre of gravity in z-direction 74

Table 8.1: Technical specifications for material selection 78

Table 8.2: Beam section properties 80

Table 8.3: Star-CCM+ and Abaqus model properties 82

Table 8.4: Elements in each type of mesh 85

Table 8.5: Displacement from mesh types 86

Table 8.6: Eigenfrequencies and eigenperiods for the aft plate with corresponding modes 88

Table 10.1: Average oscillation period and node displacements in z_{nodes} direction for each plate thickness 104

Table 12.1: Displacements with two-way coupling for the hull 119

Table 13.1: Oscillation period and displacements measured in z_{nodes}, when the air is modelled as compressible 127

Table 13.2: $TdTn$ ratios for shell thicknesses with T_d period taken as 0.252 s when air is modelled as compressible 128

Nomenclature

$\boldsymbol{n}_\alpha(\mathrm{S})$	Orthogonal direction vector
β	Dead rise angle
$\beta(2)$	Torsional constant
Γ	Diffusion vector
γ	Surface tension
$\gamma(2)$	Forcing coefficient
Δt	Time step
Δx	Length of one cell
Δx_{Stiff}	Length between stiffeners
Δx_i	Mesh discretization, i = 1, 2, 3
δt_1	Expansion time
δt_2	Collapsing time
δ'_{ij}	Kronecker delta
$\delta \boldsymbol{D}$	Virtual strain rate
ϵ	Dissipation rate
$\epsilon(2)$	Strain
η	Surface elevation
η_b	Water spray point
θ	Angle
θ_0	Contact angle
κ	Von Karman's constant
μ	Dynamic viscosity
ν	Kinematic viscosity
ν (2)	Poisson ratio
ξ	Damping ratio
ρ	Fluid density
Fr	Froude number
F_i	Force, i = 1, 2, 3, 4, 5, 6
F_n	Normal reaction force
f	Frequency in cycles/seconds
$f_{stretch}$	Stretch factor
f	Body force at any point within the volume of material under consideration
f (s)	Cross-sectional scaling factor
g	Gravity
H_c	Cavity height
H_w	Height of the mean wind velocity
|H (f)|	Frequency domain transfer function
h_p	Pop-up height
I_{ii}	Moments of inertia, i = x, y, z
I_q	Integrated quantity
J	Torsional constant
K	Stiffness matrix
k	Wave vector
k	Kinetic energy
L	Length
M	Mass
m	Meters
N	Newton
n_{global}	Global coordinate system, n = x, y, z
n_{body}	Body fixed coordinate system, n = x, y, z
n_{origin}	Origin coordinate system in FEM, n =x, y, z
n_{nodes}	Coordinate system defined by nodes, n = x, y, z

ρ_s	Solid density
σ	Principle stress
σ_{ij}	Stress tensor
σ_y	Yield stress
σ_u	Ultimate stress
τ_W	Shear stress
u_τ	Frictional velocity
ϕ	Velocity potential
ϕ^N	Eigenvector
ϕ^*	Value of the forces solution
S_θ	Source term
q_ϕ	Source term
$\psi(S^\alpha)$	Warping function
Ω	Submergence
ω	Frequency in rad/s
ω_n	Natural frequency
ω_{n0}	Undamped natural frequency
∇	Nabla operator
∂	Partial derivative
A	Area
A_{ii}	Added mass, i = 1, 2, 3, 4, 5, 6
A	Surface area of control volume
a_i	Acceleration, i = x, y, z
a	Surface vector
Bo	Bond number
b	Damping
b_{cr}	Critical damping
C_a	Cappilary number
C_D	Drag coefficient
c	Wetted length
D	Diameter
E	E-module
F_D	Drag force
p	Pressure
R	Radius
Re	Reynolds number
R_{ii}	Radius of gyration, i = x, y, z
S	Stress
S (2)	Surface bounding a volume
S_z^d	Residence term
s	Seconds
T_c	Cavity closure time
T_d	Duration of load
T_n	Natural period
t	Time
t (S)	Vector orthogonal to n_1 and n_2
t	force per unit of current area
t_0	Air cavity formation starting time
U	Velocity vector
U_w	Wind velocity
u, v, w	Velocity in x, y, z
u^+	Non-dimensional velocity
V	Volume
$v_{x'}$	Velocity in x_{body}
We	Webber number
w (s)	Warping amplitude
X_h	Prism layer height
x (S)	Position of centreline
x_{min}	Minimum cell size
Y^+	Non-dimensional wall distance
y	Center of cell height
y_p	Particular solution of response
z_0	Creation position of air cavity
z_{0r}	Roughness length

CAR	Combined Acceleration Ratio
CFD	Computational Fluid Dynamics
CFL	Courant Friedrichs Lewy
DOF	Degrees of freedom
FEA	Finite Element Analysis
FEM	Finite Element Method
FSI	Fluid-Structure-Interaction
HPC	High Performance Computer
OA	Order of Accuracy

1 Introduction

Free-falling lifeboats are one of the last options for escaping ships or oil platforms when a hazardous event happens. They fall from a typical height of 20-30 meters and enters the water with a preferable angle of 50-60 degrees. The motion from start to end is called phases, where in the later years a lot of studies have been conducted on the behaviour of the lifeboats in these phases, where the water-entry (slamming) and the submergence phases are most pronounced.

Since the weather and wave conditions will most likely be harsh when using a free-falling lifeboat, realistic experimental data is difficult to produce with the same environmental conditions. There has on the other hand been conducted experiments in calm water. As a consequence of this, new methods have been used to obtain results for a free-falling lifeboat. Here, computational fluid dynamics (CFD) has been proved to be a valuable tool for obtaining many of the same results as experiments.

The objective of the thesis is to use a simplified geometry of a lifeboat to evaluate different parameters connected with a lifeboat dive. The results are obtained with a CFD program and these results have been evaluated. In the later sections a structural analysis has been conducted, where a combination of CFD and finite element method (FEM) has been used, which means that the loads will be exported from the CFD program and imported in the FEM program. The establishment of this interaction will be discussed in the later sections.

The thesis contains therefore of two parts. The first part is connected with the physics behind all the free-falling lifeboat phases and the CFD physics, with a sensitivity and convergence study with initial conditions of the lifeboat, as well as a parameter investigation. The second part of the thesis contains the FEM modelling, a convergence study of the FEM model, the interaction between CFD and FEM, and results obtained from this interaction.

2 Introduction to free-falling lifeboat phases and physics

In the case of free-falling lifeboat diving, the process is divided into different phases. The body operates in different fluids, enters the water in high velocity, gets fully submerged, ascents to the surface and should then it be able to operate as a sailing vessel. This complex matter is thus divided into a launching phase, free-falling phase, water entry phase, submerged phase, water exit phase and the sail away phase.

The theory in the submerged phase, water exit phase and partly the water entry phase, will be based on studies of water entering and exiting projectiles, combined with theory from previous papers regarding free-falling lifeboats.

2.1 Launching phase

The lifeboat will normally rest at a skid mounted on the mother vessel. Several releasing mechanisms for launching are available, most common are the releasing hook. The lifeboat is released from the hook by a manually driven hydraulic pump that is possible to operate from the inside. After releasing, the lifeboat slides along the skid driven by the gravitational and frictional forces. As the boat passes the end of the skid, an increasingly part of the lifeboat will be free falling, while the behind part will have contact with the end of the skid. This will lead to a rotation which depend on the position of the skid in the global coordinate system.

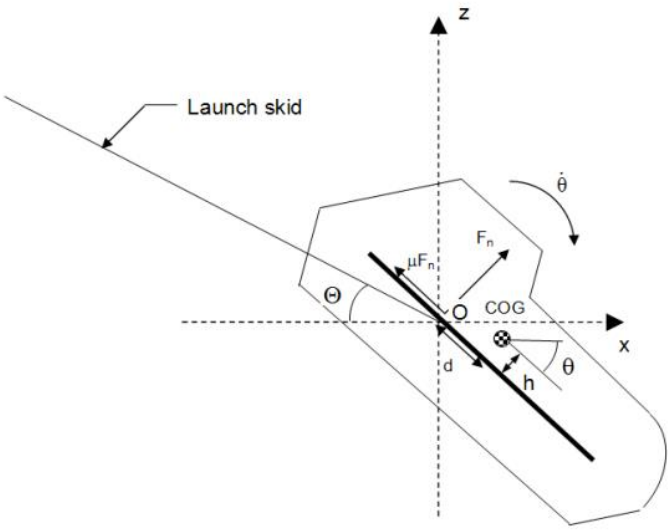

Figure 2.1: Shows the lifeboat on a launch skid, as the center of gravity passes the end of the launch skid.

Assuming a global coordinate system shown in Figure 2.1 where z represents the vertical axis, and x and y the two normal horizontal axes. The gravitational force will act downwards in z-direction. Ideally the skid plane lies in the x-z plane, the lifeboat will then move straight forward down the skid, without any translation in the y- direction. Then if the centre of gravity of the lifeboat lies along the y-axis, there will only be rotation about one axis, the y-axis. This rotation is pitch.

Since the lifeboat is used in emergency cases, the operational conditions will likely be harsh, and an ideal launch situation will be unlikely. When the skid plane moves out of the x-z plane, the skid plane will be skewed seen in the y-z plane. The gravity force pulls on the centre of gravity, leading to rotation in roll and yaw as well as pitch. The skid plane can also be tilted forward and backwards as a consequence of rotational motion of the mother vessel parallel to the x-axis of the skid plane. The result of this can respectively be an increase and decrease in the initial free-falling velocity. The rotation is dependent on the velocity at the end of the skid. If the lifeboat slides slowly over the skid end, the gravity has a large amount of time to pull down the part that has passed the skid end, causing a large rotation. In the case of high sliding velocity, the rotation will be small.

The launching plane is dependent on the motion of the mother vessel, hence the initial conditions in the launching phase is crucial for the further phases.

2.2 Free-falling phase

The free-falling phase starts when the lifeboat no longer has contact with the skid, that is when the normal reaction force from the skid is zero, $F_n = 0$, seen in Figure 2.1. The free-falling phase is affected by the rotation (angular velocity), initial velocity out from the skid, skid plane angle (launching angle), air resistance and wind loads. The free-falling time is dependent on the diving height, that is the freeboard position of launching.

Figure 2.2: Shows a free-falling lifeboat in the free-falling phase. This is a Norsafe AS production, one of the leading lifeboat producers. (Consultance, 2017)

In wave conditions where the launching point on the vessel has a relatively steady global position, the diving height will depend on the phase of the impact wave. It will increase if the lifeboat is launched such that it enters in a through and decrease when entering at a crest. Longer free-falling time leads to a larger effect of the air resistance, wind loads and larger impact velocities. However, the wind loads are not constant trough the free-falling distance. The wind velocity profile is dependent on the atmospheric stability conditions. It is also dependent on the hour of the day and changes between day and night, dawn and dusk. An example of a wind velocity profile from DNV for stable (low temperature lapse rate), neutral (medium temperature lapse rate) and unstable (high temperature lapse rate) atmospheric conditions are shown in Figure 2.3. (DNV-GL, 2010) It should be noted that most lifeboats are installed between 10-30 meter above sea level, hence, the difference regarding the wind velocity for the presented atmospheric condition is small.

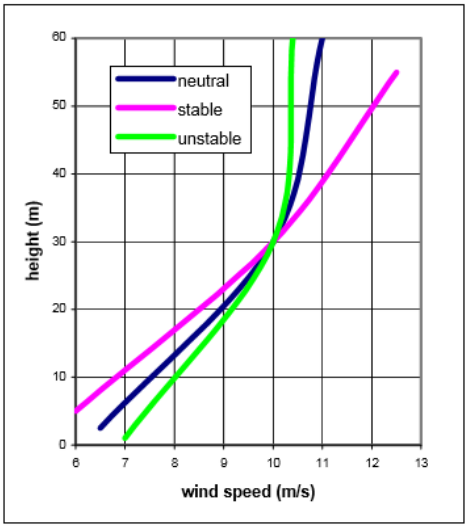

Figure 2.3: Wind conditions (DNV-GL, 2010)

A logarithmic wind velocity profile for neutral atmospheric conditions from DNV-GL is expressed as

$$U_w(z) = U_w(H_w)\left(1 + \frac{ln\left(\frac{z}{H_w}\right)}{ln\left(\frac{H_w}{z_0}\right)}\right) \quad [1]$$

Where H_w is the height of the mean wind velocity measuring, z is the height at any given point and z_0 is the terrain roughness parameter also known as the roughness length. In open sea with waves, this value is in the range of 0,0001 – 0,01 m.

The effect of the rotation, air resistance and the wind loads are dependent on the diving time. Rotation is measured in rotation angle over time, hence the water entry angle is dependent on launching angle and the rotation given at the end of the skid and free-falling time.

2.3 Water entry phase

The water entry phase starts from the initial impact between body and the free surface, and ends when the aft part of the body is below the undisturbed free surface. The launching and free-falling phases sets the initial parameters for the water entry. These parameters are the velocity, water entry angle and angular velocity in roll pitch and yaw. The typical diving height for a free-falling lifeboat launched at a skid, is between 20 m and 30 m. This will provide an impact velocity of approximately

20 m/s. The skid usually has a value of 35°, and a desirable water entry angle is 50°-60°, hence the angular velocity is providing the water entry angle. As the body enters the water it is subjected to resistance forces in terms of drag, viscosity effects and slamming. The influence of slamming forces is most critical for the water entry phase, due to the transfer of momentum from the lifeboat to the impact fluid.

2.3.1 Slamming

In the water entry phase, the free-falling lifeboat will experience impulse loads with high pressure peaks, propagating from the bow to the stern. This phenomenon is known as slamming. It is a strongly non-linear problem. It is very sensitive of the relative impact velocity, that is the liquid-body velocity, and the dead rise angle, β, which is the angle between the water and the body. The sudden transition from air to water leads to large forces on the body, and can lead to global elastic transient resonance oscillation. The slamming load are the most critical load in the matter of free-falling lifeboats, and govern the design of the local hull structure. In this phase, the pitch rotation will reverse from the free-falling rotation. The rotation is now counter clockwise, when using Figure 2.4 as reference, and causes increased slamming pressure on the aft part of the hull. For oval geometry cases, such as the lifeboat form, it is important that the water entry angle does not become too low. If it does, the slamming forces will increase rapidly due to the large change in added mass.

Some of the physical phenomena connected with slamming is compressibility of water, air cushions/bubbles (for small angle between the body and the water), hydroelasticity, cavitation and ventilation.

2.3.1.1 Simplified calculation approach

There has been performed extensive researching on the field of slamming. Von Karman (1929) and Wagner (1932) had a large impact on the field.

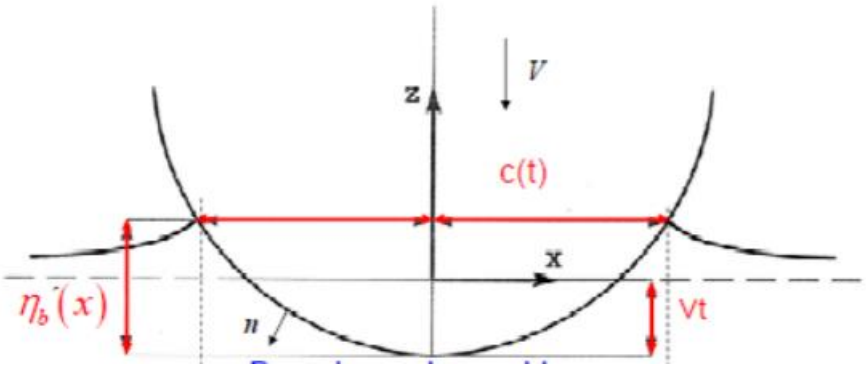

Figure 2.4: Shows how the different parameters are defined in the analysis of impact forces and pressure on a body.

The wetted area is taken to be between $-c(t) \leq x \leq c(t)$, shown in Figure 2.4. Von Karman (1929) developed a method with a simplified approach. The wetted length is taken at the free surface, excluding the up-rise water effect. Wagner (1932) includes this effect and the wetted area is taken at a height $\eta_b(x)$ which is defined as the distance from where the body has its maximum submerged point up to the point of water spray.

The density of water is almost independent of the temperature and pressure (Engineering ToolBox, u.d.), which make the incompressible assumption appropriate. For a frictionless fluid, there will be no shear forces and torque. A frictionless flow without initial fluid rotation, will never start to rotate, and the velocity can be derived by the velocity potential spatial derivatives. Equation [3] - [8], shown below, are only valid for frictionless, stationary and incompressible fluid, meaning that potential theory is applicable.

$$U = \nabla\phi \qquad [2]$$

Then for a simple two-dimensional projectile penetrating the free surface, the force in heave can be written as

$$F_3 = \frac{d}{dt}(VA_{33}) + \rho g \Omega(t) \qquad [3]$$

F_3 is the force in heave, A_{33} is the added mass in heave. The term $\rho g \Omega(t)$ is the time dependent buoyancy force, and is initially zero. The velocity and added mass in heave are time dependent variables, hence equation [3], by utilizing the product rule, can be written as

$$F_3 = A_{33}\frac{dV}{dt} + V\frac{dA_{33}}{dt} + \rho g \Omega(t) \qquad [4]$$

In this case, the pressure can be defined from the Bernoulli equation

$$p = -\rho g z - \rho\frac{\partial \phi(x,z)}{\partial t} - \frac{1}{2}\rho(\nabla\phi)^2 \qquad [5]$$

For the slamming case, by assuming that $z = 0$ at the mean water surface, and neglecting the spatial derivatives of the velocity potential, as they are much smaller than the time derivatives of the velocities potential, equation [5] can be simplified to

$$p = \rho\frac{\partial \phi(x,z)}{\partial t} \qquad [6]$$

The velocity potential on the body can be written as

$$\phi = -V\sqrt{c^2 - x^2}\,, \quad |x| < c(t) \qquad [7]$$

Then by time differentiate the velocity potential, the pressure becomes

$$p = \rho\frac{dV}{dt}\sqrt{c^2 - x^2} + \rho V\frac{c}{\sqrt{c^2 - x^2}}\frac{dc}{dt} \qquad [8]$$

The first term from equation [8], $\rho\frac{dV}{dt}\sqrt{c^2 - x^2}$, represents the added mass pressure and the second term, $\rho V\frac{c}{\sqrt{c^2 - x^2}}\frac{dc}{dt}$, represents the slamming pressure. (Faltinsen, 1990)

For a “real flow”, viscous forces will always be present, resulting in shear stresses and boundary layers, but for large $Re = \frac{uL}{\nu}$, irrotational fluid flow outside the boundary layer is a valid assumption. For the slamming case, it is assumed that the spatial derivatives are negligible compared to the time derivatives. Since the viscous term is multiplied with the spatial derivatives in the Navier–Stokes equation, the inviscid fluid assumption is reasonable for the case of slamming.

2.3.1.2 Slamming calculations for free-falling lifeboats

Calculation of the slamming pressure for free-falling lifeboats is a complex matter. There will be an oblique impact, the body is three-dimensional and waves should be considered. Sauder proposed a method for calculating the slamming phenomena for free-falling lifeboats. The method is developed to predict the trajectory in the six degrees of freedom in waves. In able to do so, three dextral orthogonal coordinate systems are used, and some approximation and assumptions had to be set.

Approximations:

- Three-dimensional formulation of fluid momentum conservation
- Long wave
- A boundary element method for evaluating the added mass matrix

Assumptions:

- The viscosity and the compressibility of the water are neglected
- Potential theory is applied
- The fluid acceleration is assumed to be much larger than the gravity acceleration, hence the high-frequency free surface boundary condition $\phi = 0$ can be used.
- Von Karman approach, local water up-rise is neglected. The pressure in the spray area will be very close to atmospheric pressure. It is the hydrodynamic pressure and forces that are of interest.
- Ventilation, cavitation and hydroelasticity are neglected

(Sauder & Fouques, 2009)

2.3.1.3 Hydroelasticity

In slamming, hydroelasticity is relevant for dead rise angles $\beta < 5°$ and when the loading time associated with water entry is small or comparable to the natural wet period of the structure. Hydroelasticity means that the hydrodynamic loads affect the structural elastic vibrations and in return the elastic vibrations affect the fluid flow and related pressure field. When hydroelasticity matters in the slamming problem, the hydrodynamic and structural problems must be solved simultaneously. In extreme cases of flat impacts with hydroelasticity the maximum pressures cannot be used to estimate the structural response. Hydroelasticity is a phenomenon connected with slamming where the dead rise angle $\beta < 5°$. (Greco, 2012)

2.3.2 Parameters defining the water entry

There are several parameters which influence the physics during a water entry problem, resulting in air entraining, super cavitation or maybe no cavity formation at all. Water entry with air cavity formation and air entraining are emphasis on, in this thesis.

Air cavity is a result of viscous forces outweighing the surface tension, and the contact line is then pinned to the body surface at the air-water project line. This resulting in air to be entrained behind the body as the air cavity develops. For water impacts, where the fluid velocity is high, a small horizontal jet gets ejected at great radial velocity outwards from the intersection point. For Spheres, Thorodsen et. al (2004) found that this was the case for Re > 9000. (Truscott, et al., 2013)

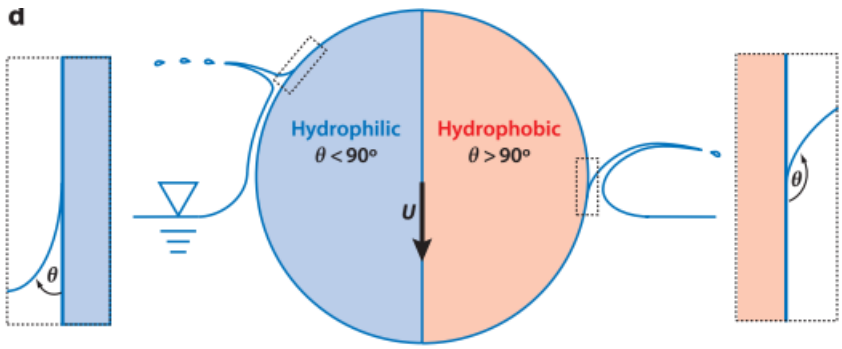

Figure 2.5: Shows the difference in splash crown formation for a hydrophilic and a hydrophobic case (Truscott, et al., 2013)

Important parameters for the entering body are geometry, wettability, density and location of center of mass, and due to variation in geometry, impact conditions and material properties, the water entry phenomenon is very complex and difficult to predict. Wettability is defined with the static contact angle θ_0 shown in Figure 2.5. If this contact angle, θ_0, is below 90 degrees, the water entry is called hydrophilic, while a θ_0 > 90 is called hydrophobic. For an interaction between a body and a given fluid with constant surface tension, less impact velocity is needed for the body at a higher θ_0 to ensure cavity creation.

Impact parameters influencing cavity creation are the impact angle, impact velocity, transverse and longitudinal spin. Truscott, et al. (2013) did experience with billiards ball, where the contact angle varies from one side to another, due to an initial spin counter clockwise. The left-hand side of the sphere experienced a larger dynamic wetting angle, due to an advancing contact angle resulting in a larger outward splash. For the right-hand side, the spin resulted in positive vertical velocity, contributing to a wedge of fluid is drawn across the cavity and inhibits splash growth. (Truscott, et al., 2013)

Important parameters for the opposite fluid is viscosity, density and surface tension. Surface tension is due to the cohesive force between the liquid molecules, with dimension force per unit length. For sea water it has a natural value of $72.8 * 10^{-3}\ N/m$. Truscott did experiments with spheres, only changing the body density ρ_s, showing the dependency of density relation, $\frac{\rho_s}{\rho}$, and cavity closure height divided on total cavity height, $\frac{H_c}{H}$. The experiment showed that $\frac{H_c}{H}$ increased with increasing $\frac{\rho_s}{\rho}$. More about cavity shapes and creation will be included in the submerged phase, section 2.4.

The value of the surface tension may be of importance for how the air cavity forms. Further influencing all the aspects of the behavior of a body, such as acceleration, velocity and trajectory when the body moves from the water entry phase to the submerged phase. For relatively large bodies and velocities, surface tension can be neglected, though it might be of importance near cavity closure. The formation of an air cavity can be predicted by non-dimensional numbers. They are all inverse proportional with the surface tension force γ. A high Capillary number may indicate that an air cavity will form, defined as

[9]

$$C_a = \frac{\mu U_0}{\gamma}$$

Where μU_0 is the viscous force. The Bond number is the ratio between gravitational forces, $\rho g D^2$, and surface tension forces. The air cavity shape is dependent on the ratio between surface tension and inertia forces for a low Bond number, defined as

$$Bo = \frac{\rho g D^2}{\gamma} \quad [10]$$

For low Bond numbers the cavity shape will be dependent on the ratio between inertia forces and surface tension, this is known as the Webber number. The cavity breakup and characterization of the splash crown stability can be predicted by this number, given as

$$We = \frac{\rho U_0^2 D}{\gamma} \quad [11]$$

Where $\rho U_0^2 D$ represents the inertia force. The Froude number characterizes the macroscopic behaviour of the air cavity

$$Fr = \frac{U_0}{\sqrt{gD}} \quad [12]$$

The lifeboat structure is relative large and the water entry velocity is relative high. Additionally, a low surface tension for water, results in very high non-dimensional numbers. Therefore, the surface tension will have little influence in the submerged phase.

2.4 Submerged phase

The submerged phase starts when the aft part passes the free surface, and for this phase, the focus will mainly target the understanding of the cavity evolution of the air cavity behind the free-falling body. The body will experience large hydrostatical pressure on the hull as well as hydrodynamic forces. The translational and rotational velocity and the water entry angle at initial water entry, affects the trajectory through the water. As mentioned earlier in the water entry phase, there are

several parameters influencing the water entry, increasing the complexity of the submerged phase. External forces will also have great effect on the trajectory. These external forces are primarily waves, but also strong current can have an effect. The waves have local phase dependent fluid particle velocity and acceleration properties, as well as wave surface elevation and slope.

2.4.1 Air cavity formation

As the very aft passes the free surface, the corner at the newly created free surface has an initially infinite curvature. The gravitational force tries to flatten out this new surface, dragging the two corners diagonally inwards towards the body-center. The contact point of where the two surfaces collapses will be the point of air cavity closure. At this point a singularity will emerge. This results in a formation of water jets. The water jets move in oppositely directions from the collapse location, one towards the body inside the entrapped air bubble, and the other in the reversed water entry direction. As the two water surfaces collapses, the body will experience an abrupt change in acceleration. The reason for this is that the newly entrapped bubble behind the lifeboat is compressed by the water surrounding it, resulting in that the body will get a positive acceleration contribution in the direction of motion. After the first compression, the entrapped bubble will oscillate due the difference in pressure inside the bubble and the surroundings, while it decreases in size until it gets dissolved.

The formation of an air cavity behind the lifeboat contributes to a stronger retardation. Hence when designing a lifeboat hull, there will be a high focus on minimizing the air cavity by mainly altering the lifeboat-stern geometry. The formation of the air cavity is most pronounced at the aft part of the body. However, there will be appendages and a wheelhouse on a lifeboat, where air cavity also will be present, but in a smaller scale. (DNV-GL, 2016)

2.4.2 Cavity classifications

The creation of air cavity begins in the first few moments after impact, as the fluid is displaced downward and upward, forming a splash curtain.

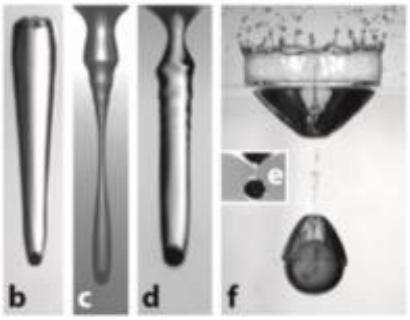

Figure 2.6: Visualization of different water entry events (Truscott, et al., 2013)

Air cavity can be divided into four types of cavity formations after water impact. Surface seal, deep seal, shallow seal and quasi-static seal, Figure 2.6 b, c, d and f, respectively. Surface seal is defined when cavity closure occurs at the free surface, with a long cavity attached beyond the body. Surface seal is often more relevant for higher Froude's Number, while a deep seal, where the pinch off occur closer to the body often is connected with relatively low Froude Number. For shallow seal, the pinch of occurs just below the water surface, like a deep seal, but with a shape more like a surface seal.

The main difference between a shallow and a deep seal is that the pinch of close to the surface in a shallow seal is due to capillary instabilities rather than hydrostatic pressure. The opposite is the case for a deep seal. Quasi-static seal is often in connection with pinch of at the body or close to it. This is common for cases where the body is almost restrained to enter the water due to the large surface tension. Aristoff and Bush (2009) presented low Bond number cases where $10^{-2} < Bo < 10^{3}$ versus Froude numbers of $\sqrt{10^{-0,5}} > Fr < \sqrt{10^{2,5}}$ and stated that only surface and deep seal occurs for $Bo > 10^{3}$. Lee et al. (1997) suggest that deep seal occurs roughly halfway between the surface and a projectile for $\sqrt{20} < Fr < \sqrt{70}$, where transition to surface seal occurred for $Fr > \sqrt{150}$.

In the case of free-falling lifeboats, the surface tension is considerably low. This leads to high Capillary, Bond and Webber number (Equations [9] - [11]), which predicts air cavity formation in form of deep seal corresponding with Froude number range for lifeboats.

2.4.3 Physical insight

The study regarding the dynamics of water impact and air cavities was intensified during the world war because of the needed design of military projectile entering water in high speed. Therefore,

most of these early experiments were conducted with a high Froude Number, resulting in relative unimportant gravity effects. In recent years, scientific interest and practical importance have led to an increase of studies with relatively low Froude number, where gravity effects are comparable to inertia forces.

To better understand the physics in the submerged phase, it is important with a basic knowledge of the cavity development and evolution, regarding both assumptions and simplifications made for the different derivations. Experiments is often conducted with high Reynolds number to ensure more accurate cavity parameter calculations when potential theory is applied. This is due to the small influence of the viscous forces. Not only experiments have been conducted regarding water entry dynamics, but also theoretical and numerical studies have been performed.

Birkhoff and Zaranthello (1957) and Lee, Longoria and Wilson (1997) used a two-dimensional analytic model to study the air cavity dynamics. In a two-dimensional potential flow, air cavity cannot be created, and to account for the three-dimensional flow effects, they had to introduce an arbitrary constant to make the kinetic energy finite. This arbitrary constant was further determined by fitting the theoretical prediction with experimental data and/or nonlinear numerical simulations. A thorough explanation of a specific derivation regarding the air cavity dynamics will be included in the compressible part for this thesis. (Yan, et al., 2009)

A simple derivation of how the cavity closure is dependent of the Froude number, can be obtained by dividing the water entry of a body and the following air cavity into two main phases. Assuming a relative low Fr>10 and a constant vertical velocity, the vertical position of the bow, z_b, after impact can be defined as $z_b = \mathrm{Vt}$, if $t = 0$ at initial impact. At some height, z_0, the creation of the cavity begins, with an initial radius $r(z_0, t_0) \approx R$, where R is the body radius assuming an axisymmetric body. As the body continuous to descend below z_0 ($t > t_0(z_0)$), the cavity expands, $\frac{\partial \mathrm{r}}{\partial \mathrm{t}} > 0$, for some time. When the cavity has reached the maximum radius, the expansion time $\delta t_1(z_0)$ is over, and the radius will decrease, eventually resulting in collapsing of the air cavity. Generally speaking, there is a height H_c, where the cavity first closes at $t = T$, and $r(H_c, T) = 0$. Initial air cavity closure can occur above the free surface, referred to as surface closure, or below the free surface, often referred to as deep closure or pinch of. Cavity closure is dependent on Froude number, where deep closure usually occurs for relatively low Froude numbers, while surface closure is more common for larger Froude numbers, discussed in section 2.4.2. Regarding the contraction phase, a basic estimate

of closure time at any height z_o can be obtained by assuming steady state, with a constant radial velocity derived from Bernoulli equation,

$$-\frac{\partial r}{\partial t} = u(z_o) = (2gz_0)\text{^}0{,}5 \text{ for } t > t_o + \delta t_1 \quad [13]$$

The time of collapse is $t_c(z_0) = t_0 + \delta t_1 + \delta t_2$, where δt_2 is equal to the collapsing phase time, and can be estimated as $\delta t_2(z_o) \cong R/u(z_o)$, by assuming that the maximum cavity radius is equal to the body radius. For many body shapes, like long vertical cylinders, the expansion phase is short compared to the collapsing phase, and can be neglected. Resulting in closure time defined as: $T = min_{z0}\,[t_0(z_0) + \delta t_2(z_0)]$ and substituting δt_2 in terms of z_o, a relation between Froude number and closure time can be found

$$\frac{TV}{D} \approx \left(\frac{3}{2^{5/3}}\right) Fr^{2/3} \quad [14]$$

At pinch of position $z = H_c$, assuming that the total cavity height $H = TV$ at pinch of, is equal to $3H_c$. According to Duclas, et al. (2007), this relation, even though with many simplifications, will show good agreement with reality in the case of relatively long vertical cylinders. More detailed derivation of the equation above can be found in Mann (2005) and Mann, et al. (2007). (Yan, et al., 2009)

2.4.4 Capillary waves evolution in the air cavity water surface

As the two surfaces collapses together at the air cavity closure, it will result in a shock, leading to air, water jet and capillary waves moving towards the body along the free surface of the air cavity. The shock creates a wave packet containing wave of different frequencies, the waves spread with the velocity $c = \omega/k$, given by the dispersion relation $\omega^2 = \left(\frac{\gamma}{\rho}\right) k^3$, where plane capillary waves are assumed. γ is the surface tension and k is the wave vector. (Gekle, et al., 2008)

2.5 Water exit phase

An important parameter for the water exit for a body breaching the water surface, is the pop-up height, h_p. It is defined as the height from the body center, to the undisturbed free surface. Pop-up height is of interest for all applications where objects breach the surface. For example, an emperor penguin breaches the surface to escape from predators. They release bubbles from their feather during ascent to reduce drag forces, resulting in an increased water exit velocity. In the case of a free-falling lifeboat, water exit speed is beneficial for a longer sail away distance.

The pop-up height depends on the free surface exit speed, which is dependent on the under-water trajectory and dynamics during surface breach. Vortex shedding is dependent on the release depth, and will in addition influence the trajectory and speed of the body. During ascent, vortices will shed differently, depending on the Reynolds number. This leads to three underwater trajectory regimes, often referred to as vertical, oblique, and oscillatory. This is demonstrated in Figure 2.7.

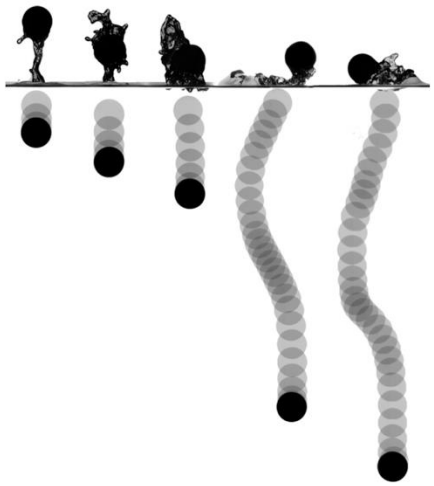

Figure 2.7: Trajectory dependent on released depth for ping-pong balls (Truscott, et al., 2016)

Depending on the Webber number (equation [11]) and the Froude number (equation [12]), during water exit in addition to the structure of the vortex shed near the water surface, the resulting splash plume and cavity will take on various forms. This indicates varying amounts of energy transferred to the fluid during water exit. A rough estimate of h_p can be derived from the mechanical energy considering the body at breach, assuming constant mass. The added mass will actually vary as the body breaches the surface, making the problem more complex

[15]

$$\frac{V_1^2}{2} + gh_1 = \frac{V_2^2}{2} + gh_2$$

Where $h_1 = h_p$, V_1 is the vertical velocity equal to zero at maximum h_p. V_2 is the vertical velocity at surface breach and h_2 is the height of the body center at water surface, equal to zero. When assuming zero net hydrodynamic forces acting on the body during breach, neglecting the work done by buoyancy and dynamic pressure forces and ignoring the energy lost when the body breaches the surface, resulting in splash and wave production, equation [15] can be simplified to

[16]

$$gh_p = \frac{V_2^2}{2}$$

this yields

[17]

$$\frac{h_p}{D} = \frac{V_2^2}{2Dg} = \frac{1}{2} * Fn_b^2$$

Seen from formula [17], the pop-up height depends on the vertical free surface exit speed as mentioned above. An increased depth of release does not have to result in higher pop-up due to the fact that the water exit velocity do not correlate with an increasing function of the release depth. For a more reliable derivation of the exit speed, where the force balance is modeled for a sphere by setting the net vertical acceleration equal to zero, see Truscott, et.al. (2016), equation 4.

Depending on the pop-up height, slamming can also occur after the water exit phase, referred to as second slamming. In the cases of second slamming, the lifeboat can have a water entry angle close to zero degrees. This angle provides the maximum slamming forces at for a given velocity. Since the slamming force is proportional with square of the velocity, and the velocity at second water entry is significantly lower, slamming forces for the first water entry is of main interest. (Truscott, et al., 2016)

2.6 Sail away phase

The main objective in the sail away phase is to get away from hazardous events. The ability to sail away from the evacuation scene is crucial and all the other phases will affect this phase. Here, the functionality of the lifeboat is described as a sailing vessel, that is resistance, maneuverability and stability. As the conditions are most likely to be challenging, the sail away performance must be of high standard, where the forward distance performance depends on the lifeboat initial motion right after resurfacing, which will be affected by waves. (Jin, et al., 2014)

2.7 Motion patterns

DNV-GL has identified four different main motion patterns for free falling lifeboat launches in calm water.

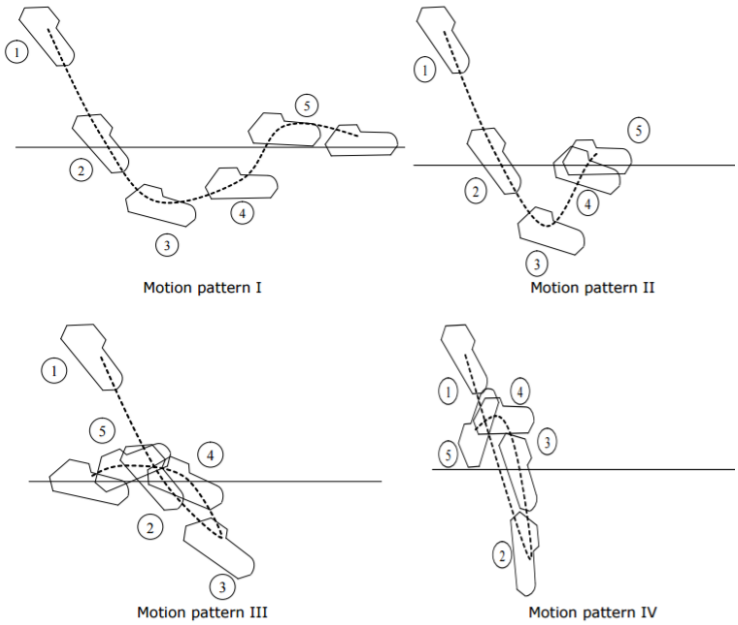

Figure 2.8: Motion patterns for a free-falling lifeboat

Where motion pattern 1, in Figure 2.8, is when the lifeboat pitches significantly at maximum submergence and ascent so that it surfaces with a positive forward velocity. Motion pattern 2, in Figure 2.8, is the same, but the forward velocity is reduced to zero and it surfaces with a negative (backward) velocity. Motion pattern 3 and 4, in Figure 2.8, is when the lifeboat moves backwards

after reaching maximum depth in water, these two motions are often referred to as *log dive*, and should be avoided. (DNV-GL, 2016)

2.7.1 Log dive

Log dive is an unwanted water exit path where the body exits with aft part first. This can occur if the water entry angle is too large. Launching problems, wind loads and entry in a through can lead to an increased water entry angle. Also, the air cavity formation should stay intact in order to have the strong drag force, pulling on the lifeboat back into the entry trajectory, reversing the path. One criteria for log dive to occur is if the maximum negative longitudinal velocity in the ascent phase accommodate the following criteria

$$v_{x'} < -\sqrt{2g * VCG} \quad [18]$$

$v_{x'}$ is the velocity in the body fixed x-direction, VCG is the vertical position of the center of gravity.

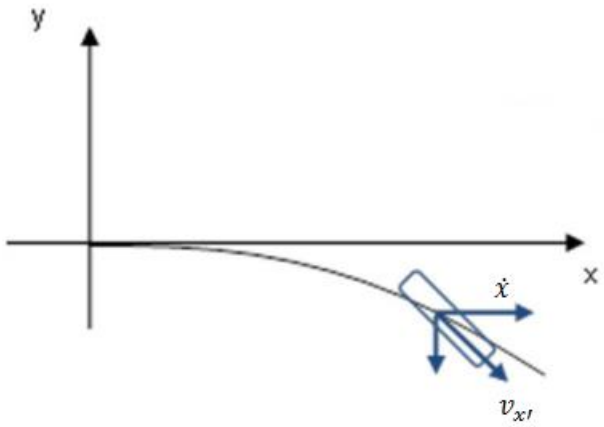

Figure 2.9: $\dot{x}$ *is the horizontal velocity of the lifeboat and* $v_{x'}$ is the sum of the horizontal and the vertical velocity components in the direction of motion. (DNV-GL, 2016)

2.8 Occupant safety

Accelerations induced on the lifeboat is important regarding the safety and comfort for the occupants. To ensure that the passengers does not get harmed by the induced acceleration, the lifeboat designer has to focus on complex combination of various relations like for example body sizes and seating.

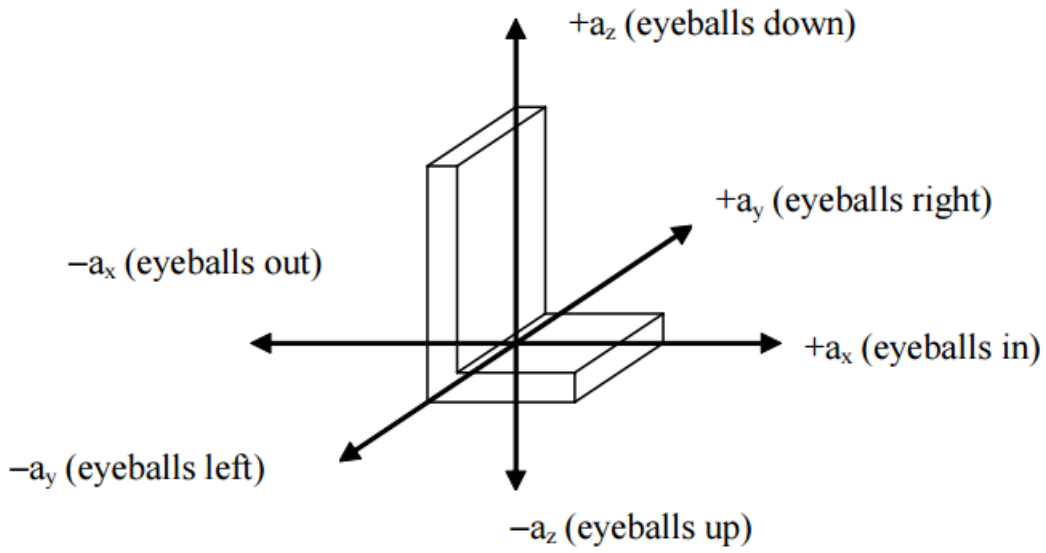

Figure 2.10: The local seat coordinate system (DNV-GL, 2016)

The basis for quantifying the acceleration induced loads on the human body in a free-fall lifeboat dive consist of acceleration components in the relevant directions. See Figure 2.10 for description of acceleration components a_x, a_y and a_z. An accepted criterion for occupant acceleration, is the Combined Acceleration Ratio (CAR), which is defined as

[19]

$$CAR = \max \sqrt{\left(\frac{a_x}{18g}\right)^2 + \left(\frac{a_y}{7g}\right)^2 + \left(\frac{a_z}{7g}\right)^2}$$

18g, 7g and 7g is the normalization constants for the accelerations a_x, a_y and a_z, respectively.

- CAR_1 for out of seat acceleration – positive a_x values in the times series only.
- CAR_2 for into seat accelerations – negative a_x values in the times series only.

For into the seat acceleration it is recommended that the normalization constant a_x is reduced with 50% from 18g to 9g. A CAR value of less than one is defined as safe.

When interpreting the CAR index the acceleration data from the time series is to be filtered with a minimum 20Hz low-pass filter. A Butterworth fourth-order filter is to be used for filtering of the acceleration data, where the frequency domain transfer function, |H(f)|, is described as

[20]

$$|H(f)|^2 = \frac{1}{1 + \left(\frac{f}{20}\right)^4}$$

where f is an arbitrary frequency (1/s). (DNV-GL, 2016)

3 Computational fluid dynamics

Computational fluid dynamics (CFD) is a branch of fluid mechanics that uses numerical analysis and algorithms to solve and analyze problems that involve fluid flows. CFD uses computers to perform the calculations required to simulate the interaction between the body and the fluid defined by the boundary conditions.

In a CFD process there are 5 to 6 main interconnected steps; 1) Geometry definition, 2) Surface grid generation, 3) Volume grid generation, 4) Flow calculation, 5) Data reduction, and 6) Experimental validation, if it can be provided. Then the software creates a second mesh, but now representing the volume occupied by the fluid, this is done to determine the behavior of the particles. After the meshes are finish, the software will set up a clear image on how the fluid will come in contact with the initial surface or object, while also emphasizing the exact problems encountered by it in the process. The software works to solve the Navier-Stokes problem, and afterwards the post-processing begins. It is assumed that the governing equations are valid. By applying the mass conservation equation and the momentum equation, four equation emerges and the pressure and the velocities in the three dimensions can be calculated. The results from CFD simulations are generally validated with previous experiments. (J. Andreson, 2009)

3.1 Governing equations in CFD

CFD calculations is based on solving the Navier-Stokes problem for four equations and four unknowns. The first of two equations that govern the fluid mechanics, is the conservation of mass. It describes the balance of mass through a control volume. The equation for this is called the continuity equation and can be expressed as:

$$\frac{\partial \rho}{\partial t} + \frac{\partial}{\partial x_j}(\rho u_j) = 0 \qquad [21]$$

Where u_j is the velocity vector in all three directions, and the operator $\frac{\partial}{\partial x_j}$ is the respectively derivatives. It implies that the mass cannot be created or destroyed in a flow field. Hence, if there is a

change in density there must be a change in the volume. It must be compressed or stretched in at least one direction, in order to conserve the mass in the control volume.

The other three equations can be expressed from

$$\frac{\rho Du_i}{Dt} = \frac{\partial \sigma_{ij}}{\partial x_{ij}} + \rho f_i \quad [22]$$

This is the basic conservation law for momentum in fluid mechanics and is valid for every relation between deformation rates and viscous stress. The stress tensor vector can be written as

$$\sigma_{ij} = -p\delta_{ij} + \sigma' \quad [23]$$

where the viscous stress tensor for Newtonian fluid, defined as "The resistance which arises from the lack of lubricity in the parts of fluid, other things being equal, is proportional to the velocity by which the part of the fluid are being separated from each other" (White, 2006) have the relation:

$$\sigma' = (\frac{\partial u_i}{\partial x_j} + \frac{\partial u_j}{\partial x_i} - \frac{2}{3} * \delta'_{ij} * \frac{\partial u_k}{\partial x_k}) \quad [24]$$

δ'_{ij} is the two variables function, called the Kronecker delta. Its value is an integer, and equal to one if the velocity component changes in its defined direction, and zero if not, shown in equation [25].

$$\delta_{ij} = \begin{cases} 0 & if\ i \neq j \\ 1 & if\ i = j \end{cases} \quad [25]$$

By inserting equation [24] into equation [23] and then into equation [22], the famous Navier-Stokes equation appears:

$$\rho \frac{Du_i}{Dt} = -\frac{\partial p}{\partial x_i} + \frac{\partial}{\partial x_j}\left[\mu\left(\frac{\partial u_i}{\partial x_i} + \frac{\partial u_j}{\partial x_j} - \frac{2}{3}\delta_{ij}\frac{\partial u_k}{\partial x_k}\right)\right] + \rho f_i \quad [26]$$

In the case of constant fluid density, which is assumed in most CFD calculation for free fall lifeboats equation [26] can be reduced to:

$$\rho \frac{Du_i}{Dt} = -\frac{\partial p}{\partial x_i} + \mu \nabla^2 u_i + \rho f_i \quad [27]$$

(Ytrehus, u.d.) (White, 2006) (J. Andreson, 2009)

3.2 Previous work with the use of CFD for free-falling lifeboats analysis

Since free falling lifeboats mainly operates at sea, experimental results for typical north-sea waves is hard to come by. Here CFD is a valuable resource for calculating forces, accelerations, path and other parameters and features.

3.2.1 Validation of CFD with experiments

Tregde (2015) ran CFD simulations of a free-falling lifeboat which started 0.5m above water level, and with initial conditions received from previous CFD simulations. The trajectory of the lifeboat is assumed to be governed by the Reynolds averaged Navier-Stokes equations in which turbulence effects are included. In the simulations some simplifications were made, such as;

- Water is assumed to be incompressible
- The lifeboat geometry is somewhat simplified to ease the meshing
- The lifeboat is assumed to be a rigid body, hydroelastic effects are not taken in account
- Air is assumed to be either incompressible or compressible with ideal gas relation
- Implicit 1st order time scheme has been used.

The simulations were compared with experimental results, where the compressible CFD simulations compared with the full scale experimental data showed good correlation for pressure on the top of canopy, figure 7 and 8 in the paper.

Tregde concludes that incompressible flow simulations would give reliable results for motions, accelerations and most pressures, except in the aft sections of the vessel, where the compressed air bubble makes a big difference. (Tregde, 2015)

3.2.2 Free-falling lifeboats in waves

Berchiche, et al. (2015) ran 12 cases of a free falling-lifeboat in waves with CFD simulations, were the waves had different headings and hit point locations, seen in table 2 in the paper. It should be noted that the simulations were done with laminar flow, with Reynolds-Averaged Navier-Stokes (RANS) and an implicit unsteady model with second order time scheme. Also there it was concluded that the CFD simulations were able to predict the motions, accelerations and pressures of the lifeboat during water entry into waves of various directions. Similar as Tregde (2015), Berchiche, et al. (2015), also states that for the local pressures at places where air-cavities are formed and then collapse, such as the aft wall of the lifeboat, it is necessary to model the air as compressible. (Berchiche, et al., 2015)

3.2.3 CFD simulations for structural assessment

In Fouques & Hermundstad (2016) they propose a method that complies with DNV-OS-E406 standard. The simulations have been done by a software developed at MARINTEK, the VARUNA launch simulation. Four different force panels were used, as seen in Figure 3.1.

Figure 3: Sketch indicating the location of the various force panels used to estimate pressure time series.

Figure 3.1: Location of force panels, P1 (hull bottom fore), P2 (roof top – fore), P3 (hull bottom aft) and P4 (Stern/back door) (Fouques & Hermundstad, 2016)

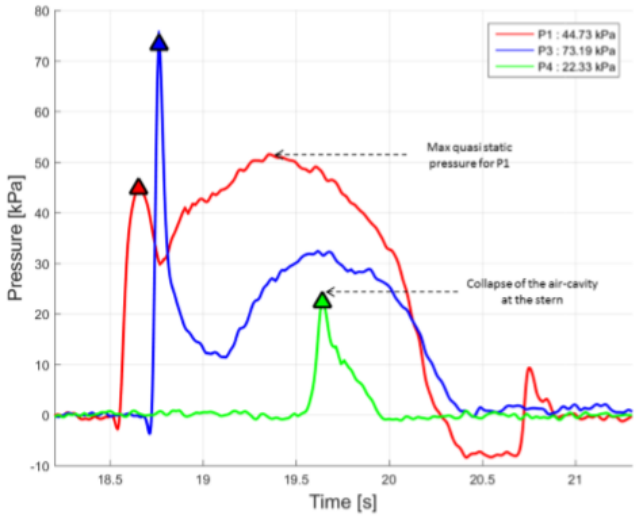

Figure 4: Example of pressure time series (full-scale) with extracted maximum slamming pressures during water impact (triangles). The definition (time instant) of the maximum quasi-static pressure is also indicated in the figure for P1.

Figure 3.2: Pressure time series for P1, P3 and P4 (Fouques & Hermundstad, 2016)

A variety of load indicators were extracted from the measured pressure time series. Figure 3.2 shows an example of pressure time series (full scale) with extracted maximum slamming pressures during water impact (triangles). For force panels P1, P3 and P4 a low pass filter at 22Hz was applied, and it should be noted that for P4 it is the maximum slamming pressure on the stern during the collapse of the air-cavity. For P2 it was applied a low pass filter at 5Hz, and it was the maximum quasi-static pressure in the submerged phase. (Fouques & Hermundstad, 2016)

With respect to the Offshore Standard (DNV-OS-E406) (Califano & Brinchmann, 2013) also considers the use of CFD and FEA. Here the CFD program used is Star-CCM+ version 6.06.011 from CD-Adapco. For the structural analysis it was used a quasi-static approach with an added amplification factor during the post-processing. This was done to take into account that applied loads are considered as quasi-static, neglecting their dynamic nature. A dynamic load can have a significant effect on the structure depending on the structures ability to quickly respond to the applied load. Their work is not covering a fully developed fluid-structure interaction (FSI) analysis, where structural deformations (for instance local skin deflections) will affect hydrodynamic loads on the hull and vice versa. (Califano & Brinchmann, 2013) and (Fouques & Hermundstad, 2016) both concludes with that their approaches complies with the Target Safety requirements as set forth by the Standard (DNV-OS-E406). (Califano & Brinchmann, 2013)

3.2.4 Sail away phase

The work is done by Jin, et al., (2014). The forward distance performance of a free-falling lifeboat after water exit is addressed. A numerical study with irregular sea state under constant wind and current velocities has been used. Three weather directions, two autopilot settings and different initial motion conditions of the lifeboat are considered in the simulations. The waves are modeled using the JONSWAP spectrum, where the waves have no directional spreading and the wave forces included are of first-order. The current and the wind has a constant velocity. The current forces are implemented by superposing the current velocities onto the local forward and transverse velocities onto the local forward and transverse velocities through the sea. The sea state is represented in table 2 in the paper. Within this weather data the directions considered was: head sea, bow quartering sea and beam sea. The two autopilot system headings were set against the weather and the other along the launch direction. They are represented in table 3 in the paper.

The results obtained from the simulations, shows that the forward distance performance depends on the lifeboat initial motion right after resurfacing of the forward distance simulation. Positive initial surge velocity and small initial yaw angle gives better forward distance performance compared to those with negative surge velocity and large yaw angle. When the desired heading is set to along launch direction, the forward distance is observed best in beam sea condition, and the transverse motion is observed smallest in head sea condition. For the bow quartering and beam sea the transverse motion is quite similar. With positive surge velocity and negative initial yaw angle, the lifeboat is able to turn straight against weather without drifting sidewise. Some important aspects have been identified in the paper, such as that the lifeboat can be pushed backwards before gaining forward distance in some cases, and that the drift motion can be difficult to avoid in bow quartering and beam seas. (Jin, et al., 2014)

3.3 Star-CCM+

Berichiche, et al. (2015), Califano & Brinchmann (2013) and Tregde (2015) used the software Star-CCM+ when simulating with CFD and free-falling lifeboats, therefore Star-CCM+ is a reasonably

choice of software. The software is developed by CD-Adapco and features step-by-step tutorials to minimize the steep learning curve of the software.

3.3.1 Physics

To get the most realistic results from the CFD simulations, the physics are carefully selected. This involves volume discretization, turbulence models, interface capturing, wall Y^+equations, Courant number validation and boundary conditions. Star-CCM+ is a leading software in the matter of CFD analysis, it is a commercial code, and later theories are related to this software.

3.3.1.1 Transport equation

Star-CCM+ uses the governing equation in fluid mechanics and transforms it in to a set of algebraic equations. For this transformation, the equations have to be discretized in space and time. Then the resulting linear equations are solved by an algebraic multigrid solver. A closed set of equations are obtained after introducing an appropriate constitutive relation into the conservation equation. The integral form of the transport equation, equation [28], is obtained by integrating the generic transportation problem over the control volume and applying Gauss divergence theorem:

$$\frac{d}{dt}\int_V \rho\phi dV + \int_A \rho \boldsymbol{v}\phi \cdot d\boldsymbol{a} = \int_A \Gamma\nabla\phi d\boldsymbol{a} + \int_V S_\phi dV \qquad [28]$$

Where the first term is the transient term, the second term is the convective flux, the third term is the diffusive flux and the fourth term is the source term. V is the control volume ϕ is the transport of a scalar property, $\boldsymbol{A}$ is the surface area of the control volume and $d\boldsymbol{a}$ represents the surface vector, Γ is the diffusion vector and S_ϕ is the source term.

3.3.1.1.1 Segregated flow solver

To solve the integral conservation equation of mass and momentum in a sequential manner, the segregated flow solver can be used. Then by iteration process the non-linear governing equation are solved for the solution variables, that is the velocities and the pressure. A pressure correction equation is solved to fulfil the mass conservation constraints on the velocity field used in the employed pressure-velocity coupling algorithm. The momentum equation and the continuity

equation is used for the construction of the pressure correction equation. Then the predicted velocity field fulfils the continuity equation, this is achieved when correcting the pressure. The pressure correction equation also obtains the pressure as a variable.

3.3.1.2 Turbulence models

In Star-CCM+, there are currently four major classes of Reynolds-Average Navier-Stokes (RANS) turbulence models, which are time averaged equation of motion for fluid flow. To obtain RANS equation, the Navier-Stokes equations for the instantaneous velocity and pressure field are decomposed into a mean value and a fluctuating component. “The averaging process may be thought of as time averaging for steady state situations and ensemble averaging for repeatable transient situations.” (Steve CD adapco, 2016)

3.3.1.2.1 Spalart –Allmares

It is applicable for cases where the boundary layers are largely attached and separation is mild if it occurs. It is often used in connection with aerospace external flow applications, like flow over a wing. This turbulence model is not suited for flows dominated by free share stress layer in connection with complex recirculation. Therefore, this turbulence model is not of interest, due to separation on the aft part of the lifeboat. (Steve CD adapco, 2016)

3.3.1.2.2 K-Epsilon model

The K-Epsilon turbulence model is a two-equation model that determines the turbulent viscosity. This is done by solving the transport equations for the turbulence kinetic energy $\boldsymbol{k}$ and its dissipation rate ϵ. According to Star-CCM+, this turbulence model provides a good comparison between robustness, computational cost and accuracy. Unlike the Spalart–Allmares model, K-Epsilon are suited for complex recirculation, with and without heat transfer. (Steve CD adapco, 2016)

3.3.1.2.3 K-Omega model

The K-Omega model and K-epsilon both solve two transport equations. The main difference is the choice of the second transported turbulence variable. The K-Omega model has improved performance for boundary layer under adverse pressure gradients, compared to the K-Epsilon model. This is perhaps the most significant advantage for the K-Omega model. In the K-Omega model original form, the largest disadvantage is that the boundary layer computations are very sensitive of

the specific dissipation rate (ω) in the free stream. This leads to extreme sensitivity in the inlet boundary conditions for internal flows. This problem is not present for the K-Epsilon model. (Steve CD adapco, 2016)

3.3.1.2.4 Reynolds stress transported model

According to Star-CCM+, it is the most complex and computationally expensive models offered. It is best suited for situations where the turbulence is strongly anisotropic. This is highly relevant for the swirling flow in a cyclone separator (Cyclonic separation is a method of removing particulates from an air, gas or liquid stream). (Steve CD adapco, 2016)

3.3.2 Free boundaries approximations

For fluid dynamics, both Langrangian and Eularian coordinates are commonly considered. The Langrangian coordinate system is following the fluid particle at each point, and then the fluid properties are determined as the fluid particle is moving. The Eulerian coordinate system is just observing the fluid properties as a function of time and space. Lagrangian coordinates are most common to use as basis for numerical solution algorithms in connection with structural dynamics. Eularian coordinates are often used since the free boundaries undergo such large deformations that Lagrangian methods cannot be applied. Free boundaries are often referred to as surfaces where discontinuities exist in one or more variable. Shock waves and interfaces between fluid and deformable structures are example of free boundaries. The problems related to numerical treatment of free boundaries can be divided into three; their discrete representation, evolution in time and the way boundary conditions are imposed on the free boundaries. (Hirt & Nichols, 1979)

3.3.2.1 Volume of fluid method

There are varies ways to approximate free boundary in finite numerical simulations, but the most common method is based on the concept of a fractional Volume of Fluid (VOF). This method defines a function F. Its value is of unity if the point of interest is fully occupied with fluid, and otherwise zero. For a distinctive cell, represented by several points, the average value of F will then represent the volume fraction of the cell occupied by the fluid. A cell that only contains fluid will have the value

of unity, while a zero value represent no fluid. Hence, if F has a value greater than zero and smaller than one, it implies that the cell must contain a free surface. The VOF method solves the transport equation for the volume fraction F of the occupied liquid in each cell in the grid (see equation [29]). Only one value for the fractional volume is required for each cell, where the fractional volume at the current time step in each cell is located using the velocity field and fractional volume at the previous timestep. This method is time efficient and beneficial due to the fact that it only requires one storage word for each cell. In addition to identify the cells with boundaries, it is important to know where the fluid is located at the boundary. This is predicted only by the scalar fractional volume value and the filling state of the cells sharing a common side, which is considered as the methods main draw back.

$$\frac{\partial F}{\partial t} + u * \frac{\partial F}{\partial x} + v * \frac{\partial F}{\partial y} = 0 \qquad [29]$$

Equation [29] is an example of the derivations of the transport equation for two-dimensional cases, where F moves with the fluid. This can readily be extended to three dimensional calculations.

When both the value of F and the direction of the boundaries are known, a line separating the cell can be constructed to represent the interface, which further can be used when setting the boundary conditions. For cases related to surfaces where the fluids do not remain fixed, but have relative motion in addition, the equation above must be modified. Handling of boundaries between single face and two face fluid regions and shockwaves are examples for when the equation must be modified. (Hirt & Nichols, 1979) (Faltinsen & Timokha, 2009)

3.3.3 Wall Y+

The non-dimensional wall distance, Y^+, for a wall bounded flow is given as

$$Y^+ = \frac{y u_\tau}{\nu} \qquad [30]$$

u_τ is the frictional velocity at the body, y is half the cell height closest to the body and ν is the local kinematic viscosity (m^2/s) of the fluid. It is commonly used for boundary layer theory and the non-dimensional velocity u^+ is given as

$$u^+ = \frac{u}{u_\tau} \quad [31]$$

Where $u_\tau = \sqrt{\frac{\tau_W}{\rho}}$ and τ_W is the shear stress.

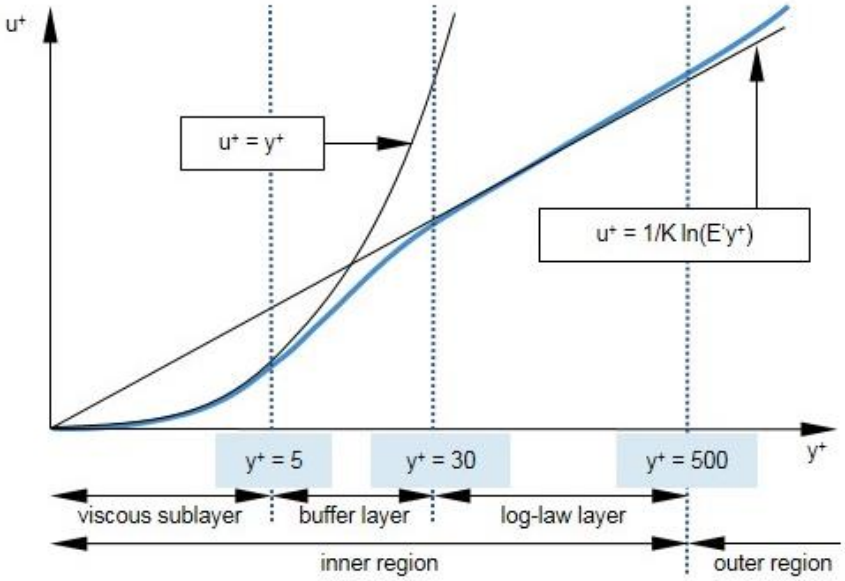

Figure 3.3: Correlation between Y^+ and u^+ (Steve CD adapco, 2016)

The logarithmic layer from Figure 3.3 can be described as:

$$u^+ = \frac{1}{\kappa}\ln(E'y^+) \quad [32]$$

Where κ is the von Karman's constant, approximately equal to 0,42. $E' = \frac{E}{f}$ where E is a coefficient equal to 5,1 and f is the roughness form function. Figure 3.3 shows that u^+ follows the relation of Equation [32] after as Y^+ passes the value of approximately 30. (J. Andreson, 2009) (Steve CD adapco, 2016)

Regarding the wall treatment, three different settings can be chosen in Star-CCM+, this depends on the value of Y^+. If the value is in the viscous sublayer, that is $Y^+ < 5$, the" low Y^+" setting should be used. Often utilized when:

- The accurate prediction of the boundary layer velocity and/or temperature profile is important.
- Simulation time and therefore cell count is not a critical issue.

If the value is in the "log-law layer", that is $Y^+ > 30$, the "high Y^+ should be used. Beneficial to utilize when:

- The wall roughness effect must be included.
- Simulation time and cell count is of critical issue.

A third setting is the "all Y^+". It is a hybrid treatment that uses both the low and high Y^+ treatment. For the buffer layer $1 < Y^+ < 30$ it uses a blending function and gives reasonable solutions for low values in the buffer layer. It is beneficial to choose this setting when Y^+ is varying due to varying geometry and velocity scale associated with the model. (Steve CD adapco, 2016)

3.3.4 Courant Friedrichs Lewy Number

The formula for the dimensionless CFL (Courant Friedrichs Lewy) number is given as:

$$CFL = \frac{u\Delta t}{\Delta x} \quad [33]$$

It gives an indication of the ratio between the simulated fluid distance for a given time step, Δt, and the length of one cell, Δx. For every time step, Δt, the Navier-Stokes equations are solved by the iteration process. If the CFL number has a value smaller than one, it implies that there will be at least one solution for each cell. For a moving mesh, such as overset meshes, u is defined as the velocity relative to the mesh in Star-CCM+. Small CFL are advantageous for the quality of the solution, but as a compromise for the computational calculation time, some increase must be tolerated. (Steve CD adapco, 2016)

The CFL number is of interest where the body intersect with the surrounding fluid. Due to the change in density across the cell in a free surface, a low time step is important to ensure robustness for the interface capturing of the free surface. This can be showed by a simplified momentum equation for incompressible, isothermal and immiscible fluids, where the flow does not have pressure and velocity gradients. The momentum equation then reduces to

$$\frac{\partial u_i \rho}{\partial t} = -\nabla \rho u_i u_i \quad [34]$$

Seen from equation [34], a change in density across the cell will lead to change in the acceleration. Large difference in the density within a cell combined with a time step too “coarse” can therefore lead to unrealistic large accelerations. The fluid will in addition accelerate when it passes sharp corners. Hence, numerical instabilities are most pronounced when sudden changes in geometry (like sharp corners) intersect with the free surface. (Kim & Park, 2016)

3.4 High Performance Computers

With the use of CFD calculations the need of processing power increases with the amount of cells in the simulation. Here high performance computers (HPC) will be valuable. With the use of these computers, more accurate simulations are possible, and the time before the results are available for the user decreases.

Vilje is NTNU's HPC and has 1404 nodes with two hyperthreaded eight-core processors per node of the type Intel Xeon E5-2670 ('Sandy Bridge'), which results in a total of 22 464 cores. There are 32GB RAM attached to each node. (NTNU HPC Group, 2016) As the simulation goes downwards in mesh size and time step, more CPU power is required. Vilje is que based where the job is submitted with a wall time and a number of processors that shall be used, an advice from Andrea Califano was that the simulations should at least have one processor per 30 000 cells. Which was extended to roughly 40 000 cells per processor to reduce que time at Vilje.

By using Vilje, one encountered limitation was the mesh operation, since this operation had to be done beforehand. For this operation, an Asus Zenbook U500V with Intel® Core™ i7-3612QM

processor and 10 GB RAM was used. Star-CCM+ recommended approximately 1 GB RAM per 500 000 cells for this study's mesh configurations, which results in a maximum of 20 000 000 cells in the simulations. (Steve CD adapco, 2016)

4 Pre-Processing

In order to establish the accurate solutions for the simulations, a geometry, mesh configurations, boundary conditions and physics has to be interpreted into Star CCM+.

4.1 Geometry

For the simulations of a free-falling lifeboat, a simplified geometry was chosen. The reason for the simplification is to not complicate the process with appendages such as a wheelhouse. Still, the essence of the behavior of the body will be similar to an actual lifeboat. This gives valuable training in simulating free fall lifeboat diving. The geometry chosen is therefore an ellipsoid, Figure 4.1, with specifications in Table 4.1.

Figure 4.1: Simplified geometry

PARAMETERS	VALUES	DIMENSIONS
LENGTH	10	m
DIAMETER	3	m
MASS	23561.9	kg
VOLUME	47.1	m^3
I_X	21205.8	$kg*m^2$
I_Y	481841.8	$kg*m^2$
I_Z	481841.8	$kg*m^2$
I_{XX}	21205.8	$kg*m^2$
I_{YY}	150501.9	$kg*m^2$
I_{ZZ}	150501.9	$kg*m^2$
R_{XX}	0.949	m

R_{YY}	2.527	m
R_{ZZ}	2.527	m
COG_X	3.75	m
COG_Z	-0.5	m

Table 4.1: Simplified geometry properties taken from the body fixed coordinate system

a) b)

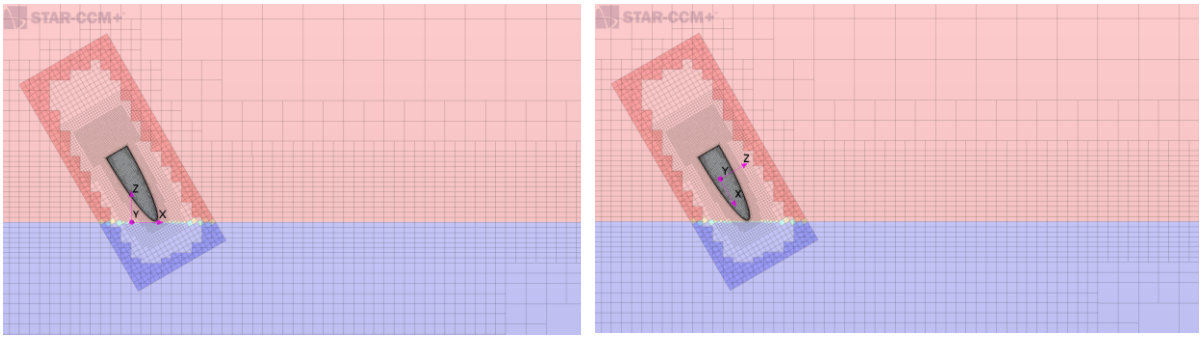

Figure 4.2: Visualization of the coordinate systems, a) is the global coordinate system and b) is the body fixed

Figure 4.2 a) shows the global coordinate system where the origin is located at [0, 0, 0] at all times in the simulations. The body-fixed coordinate system shown Figure 4.2 b), will be located in the body centre of gravity, and will follow the motion of the body. The different coordinate systems will be referred to as n_{global} for the global coordinate system and n_{body} for the body fixed, where n = x, y or z.

4.2 Boundary conditions

In order to get results that matches a realistic solution, the boundary conditions applied to the different regions in the CFD simulation must be defined. These conditions define the inputs of the simulation model. Whether the fluid flows around or through the body in question, or if the fluid enters or leaves the domain. Hence the boundary conditions connect the simulation model with its surroundings.

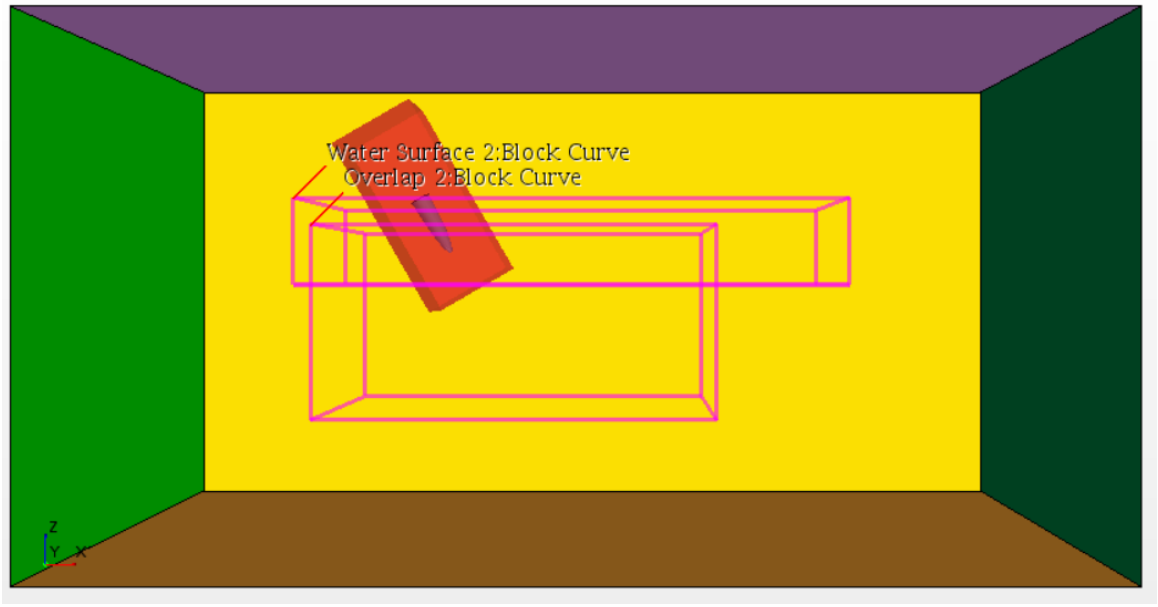

Figure 4.3: Boundary conditions illustration

Figure 4.3 shows the domain chosen for this study. Bright green is labelled as “inlet”, green as “outlet”, purple as “top”, brown as “bottom”, yellow as “port”, red as “overset”, and the transparent as “starboard”. In Figure 4.3, two additional areas are highlighted. The upper one is the “water surface” and the lower one the “overlap”. Their different dimensions are found in Table 4.2.

PART NAME	**CORNER 1 DIMENSION** (x, y, z) $[m, m, m]$	**CORNER 2 DIMENSION** (x, y, z) $[m, m, m]$	**CELL SIZE IN 0,08m MESH** $[m]$
BOUNDARIES	-50, -40, -45	100, 40, 32	5.12
OVERLAP	-15, -20, -25	45, 20, 4	0.64
WATER SURFACE	-18, -18, 8	65, 18, -5	0.64, 0.64, 0.32
OVERLAP OVERSET	-18, -11, -11	10, 8, 8	0.64
OVERSET	-17.5, -7, -7	13.25, 7, 7	0.32
BOX BEHIND	-8.5, -3.5, -3.5	-3.75, 3.5, 3.5	0.08

Table 4.2: Dimensions for each part in the simulation, where Overlap Overset, Overset and Box Behind is measured in the body fixed coordinate system, while the rest of the parts in the global coordinate system

Port, starboard, top, bottom, inlet, outlet, water surface and overlap will be referred to as the domain, while overset and the lifeboat will be referred to as it is. This is due to the set up in Star-CCM+ where they are assigned as two separate regions.

In Star-CCM+, the domain was assigned as one region with different boundaries, were as the inlet, top and bottom is assigned as velocity inlet. The velocity inlet represents the inlet of a duct for a

known flow velocity and is therefore set to zero in this case, as there is no initial current or velocity flows. The outlet of the domain is assigned as pressure outlet. The boundary face velocity is extrapolated from the interior using reconstruction gradients. The boundary condition for the lifeboat is set to wall. There will be no slip at this boundary, meaning that the fluid attached to the boundary will follow the body, resulting in a boundary layer with thickness δ and velocity gradients.

The lifeboat is impermeable, hence there will be no fluid passing through this boundary. Port and starboard side of the domain are assigned as symmetry plane. The symmetry plane can be seen as walls, due to the impermeability. However, slip condition is applied, which results in zero shear stress. The assigned parts should be placed such that the velocities at the boundaries is equal to the inlet velocity, resulting in zero velocity gradients close to the assigned parts. Large velocity gradients close to or in the boundaries will influence the simulations, therefore a large domain for this case was necessary. The overset is the interaction between the two regions, domain and lifeboat, and is where the volume to solve on is generated. For the interaction between the domain and overset to work properly, the mesh size in the overset cannot be smaller than half of the mesh size in the overlap region. (Steve CD adapco, 2016)

4.3 Mesh configurations

In order to get accurate results, a good mesh configuration is needed. In this thesis, a region based meshing was used combined with the Star-CCM+ overset mesh, where the overset mesh follows the body. The overset mesh describes how the regions in the simulation are related to each other, it creates an interface between the background (domain) and the body in question (the lifeboat). The mesh is generated with surface re-mesher, trimmer and prism layer options are enabled. Surface re-mesher uses the existing surface and optimizes it for the volume mesh models. The trimmer model is used to provide a robust and efficient method of producing a high-quality grid for both simple and complex mesh generation problems. Here hexahedra cells were used with smaller cells closer to the body such that all data were captured. The prism layer model is used with the two other models to generate orthogonal prismatic cells next to wall surfaces or boundaries. This layer of cells is necessary to improve the accuracy of the flow solution, due to better capturing of velocity gradient and viscous effects. It should be pointed out that the mesh operation is time-consuming, since the solving area should be large enough, such that near-wall disturbances do not occur. In this case it will be the lifeboat inside the overset region. The complete mesh is shown in Figure 4.4.

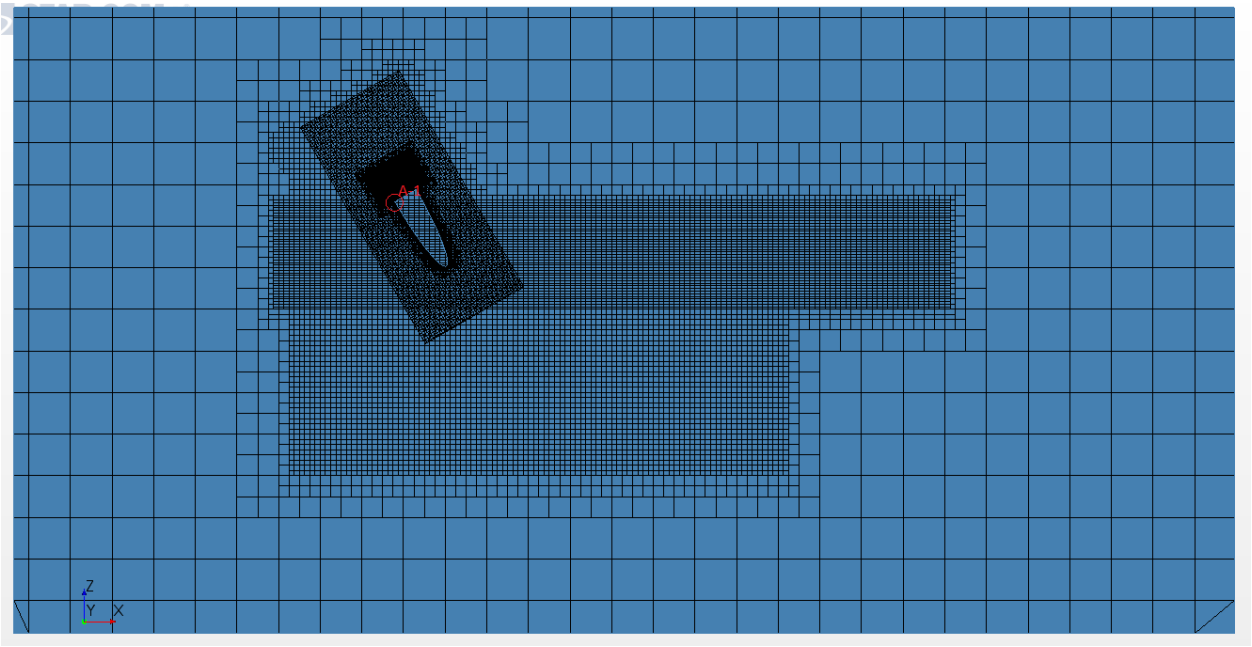

Figure 4.4: Mesh

As mentioned in section 3.3.3**,** the closest cell to the body should be so small that the wall Y^+ value is within the region of the selected model. This was done using the prism layer model, as mentioned, where the total height, number of prismatic layers and height for the cell closest to the body were inserted into Star-CCM+. The total height of the prism layers is influenced by the number of prism layers, and this number was recommended by Star-CCM+ user guide to ensure a stretch factor over the cells to be between 1.3 and 1.5. Though the simulations were conducted with varying mesh size, the cell height closest to the body were kept constant in the prism layer, hence small changes for the Y^+ values.

[35]

$$X_h = x_{min} * \sum_{n=0}^{N} f_{stretch}^{n}$$

Equation [35] shows how the prism layer height, X_h, is obtained from the minimum cell size, x_{min}, and stretch factor, f_{strech}. To ensure a smooth transition between the prism layer and the surrounding mesh the total height of the prism layer and the last cell in the prism layer is close to the size of the first cell outside the prism layer, as seen in Figure 4.5.

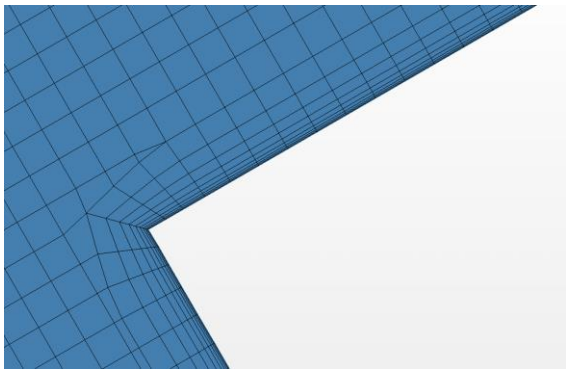

Figure 4.5: Prism layer illustration on the corner, cut-out A-1 from Figure 4.4

To capture the behaviour of the air cavity formed on the aft, a refined mesh was applied here, as seen in Figure 4.6**.**

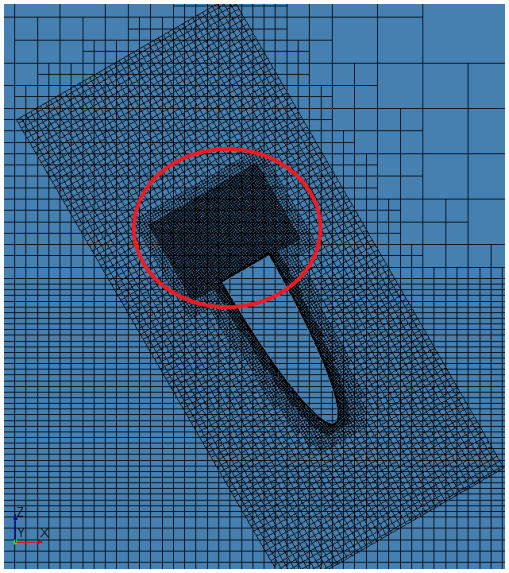

Figure 4.6: Refined mesh on aft part inside the overset

4.4 Applied physics

As described in section 3.3 Star-CCM+ offers a large variety of physics modules. In order to narrow the modules down for the case of a free-falling lifeboat, the work done by (Berchiche, et al., 2015), (Califano & Brinchmann, 2013) and (Tregde, 2015) has been used as guidelines. For this thesis the main physic modules are found in Figure 4.7.

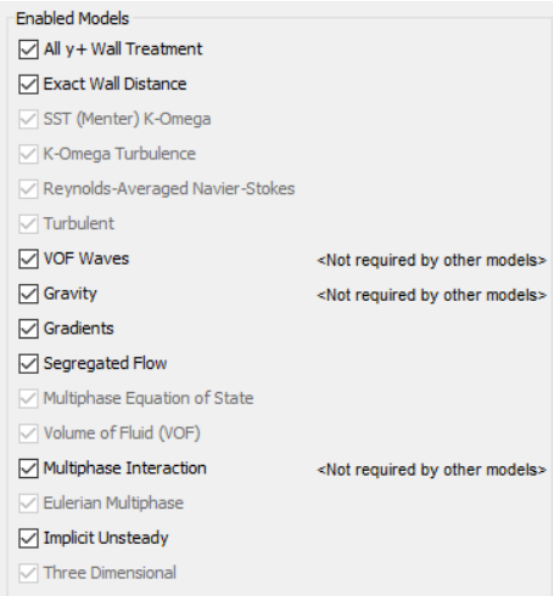

Figure 4.7: Main applied physics in the simulations

For the simulations discussed in section 3.2 Berchice et al. (2015) used a laminar flow, Califano & Brinchmann (2013) used a K-Omega module and Tregde (2015) a K-Epsillon module. Simulations with different turbulence models were conducted, where the difference in path and acceleration were unnoticeable. K-epsilon had longer solving time then K-omega for the same time step, but tolerated a higher time step before the simulation diverged. The reason for the all Y^+ treatment, was due to the density difference in water and air causing huge variation for the Y^+ at the same time instance, resulting in some values lower than 30, as seen in Figure 4.8. Y^+ values outside the log layer relation is less realizable for high Y^+, as mentioned in section 3.3.3. Therefore, a hybrid version of low and high wall Y^+ where chosen.

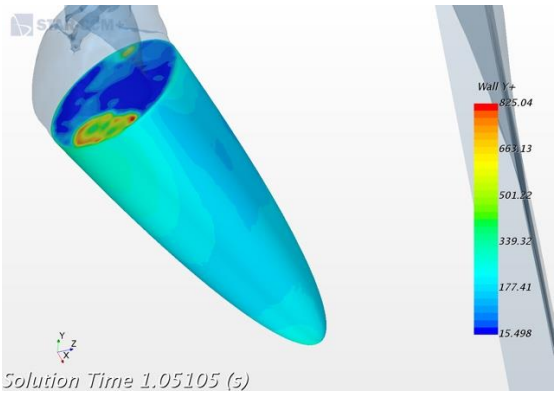

Figure 4.8: In the aft part of the body, air is still entrapped after 1.05 seconds, though the body is fully submerged, results in Y^+ values below 30.

Both (Califano & Brinchmann, 2013) and (Berchiche, et al., 2015) used an implicit unsteady time scheme with second order temporal discretization. An unsteady time scheme with second order temporal discretization have been applied for all the simulations conducted with incompressible air. The interface technique has been VOF for all the simulations, where the basic concept regarding this method is mentioned in section 3.3.2.

The solver chosen is the segregated flow solver, mentioned in section 3.3.1.1. It should be noted that the segregated flow solver can handle mildly compressible flows and low Rayleigh number natural convection, but it is not suitable for shock capturing, high Mach number and Rayleigh number amplifications. (Steve CD adapco, 2016)

5 Sensitivity & Convergence

In order to get accurate results, it is necessary to determine a time step that correlates with the grid and mesh size. In addition, a sufficient amount of iterations for each time step has to be obtained, such that each time step converges.

A convergence study has been conducted to see how the cell size in the grid affects the solution. It is assumed that the solution is improved by decreasing the cell size. A convergence study is also useful for selecting the mesh size with respect to solution quality and computational time.

5.1 Sensitivity Analysis

The sensitivity analysis has been conducted for the mesh with the lowest number of cells. This is for the sake of the low CPU cost, and acceptable results for the purpose.

5.1.1 Residuals

The residuals indicate how well the governing equations for each solver quantity are being satisfied numerically. This will be different for each simulation due to the varying Δt, but as the Star-CCM+ user guide states: The amount that a residual decrease is dependent on the particulars of the simulations. Therefore a drop of 3-4 magnitude in the residuals might be sufficient for one simulations, but not for another. (Steve CD adapco, 2016) This does not indicate that the solution necessarily is the correct one, but the correct one for that mesh size with the corresponding Δt.

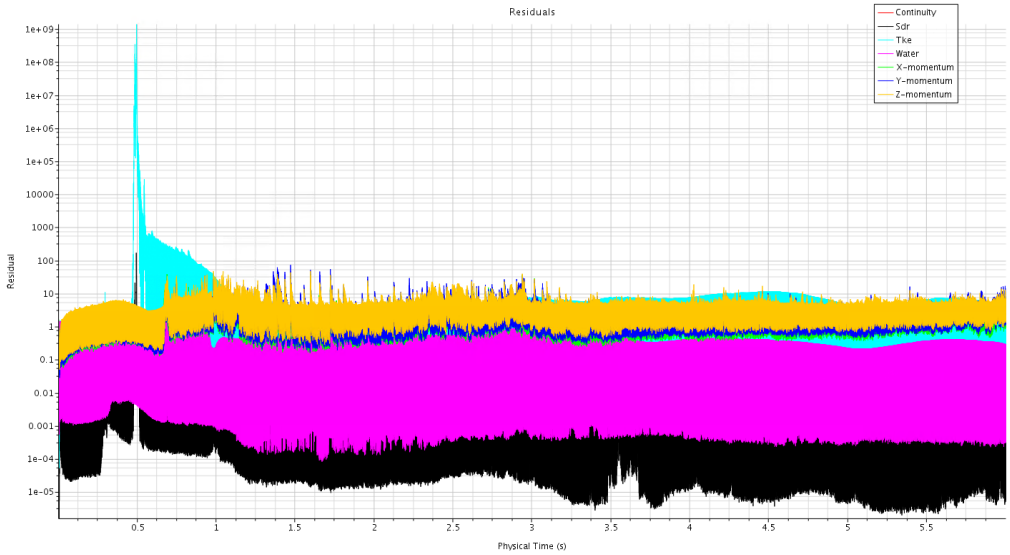

Figure 5.1: Residuals for the whole simulation with Δt =1.2ms and 10 inner iterations.

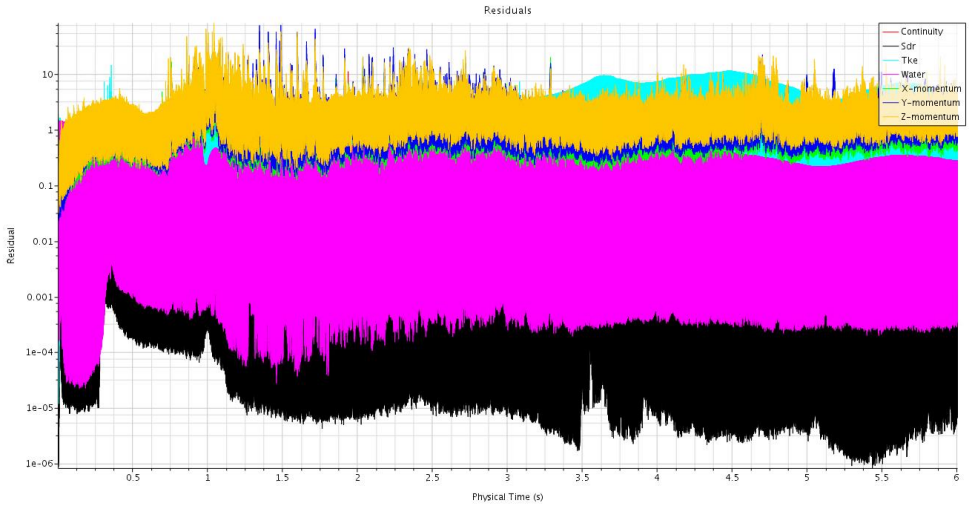

Figure 5.2: Residuals for the complete simulation with Δt=0.6ms and 10 inner iterations

By comparing the residuals values for each of the two time steps, Figure 5.1 and Figure 5.2, it is possible to see that the solver gets better residual values for lower time steps. The most critical area for the solver is around 0.3 s - 0.6 s, in the transition between water entry phase and submerged phase. As for the two time steps, 1.2 ms and 0.6 ms, the difference between the residuals in this critical region is in the order of approximately 10^9. Mentioned in 3.3.4, unphysical numerical solution might occur for sudden changes in geometry in connection with interaction with free surfaces, if the time step is not sufficiently low. Seen from Figure 5.1, the turbulence model (Tke) seems to diverge after approximately 0.45 s. This is when the sharp corners on the aft part of the body gets submerged, as seen in Figure 5.3, and unphysically high fluid accelerations may influence the

robustness of the turbulence model. Therefore, the lowest time step of 0.6 ms was chosen to correspond with the coarsest grid.

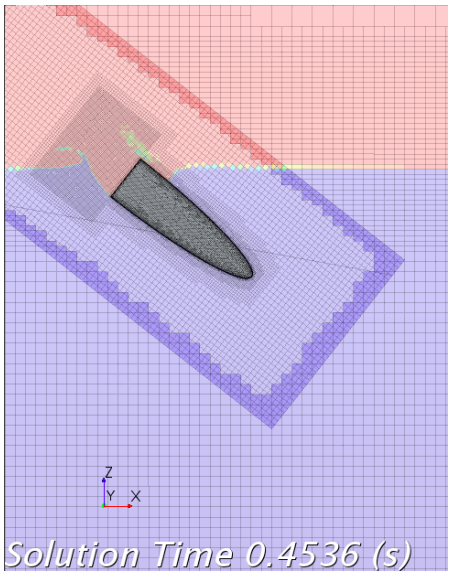

Figure 5.3: VOF picture approximately from where the turbulence model starts to diverge for larger time steps, even though the time steps are relatively small

5.1.2 Number of iterations

The maximum inner iteration is based on the number of inner iterations that the solver executes for transient analyses. As for the 6-DOF solver, it computes fluid forces, moment and gravitational forces on a 6-DOF body, in this case the lifeboat. Pressure and shear forces are integrated over the surface of the lifeboat. The forces and moments acting on the 6-DOF body are used to compute the translational motion of the center of mass of the body and the angular motion of the orientation of the lifeboat.

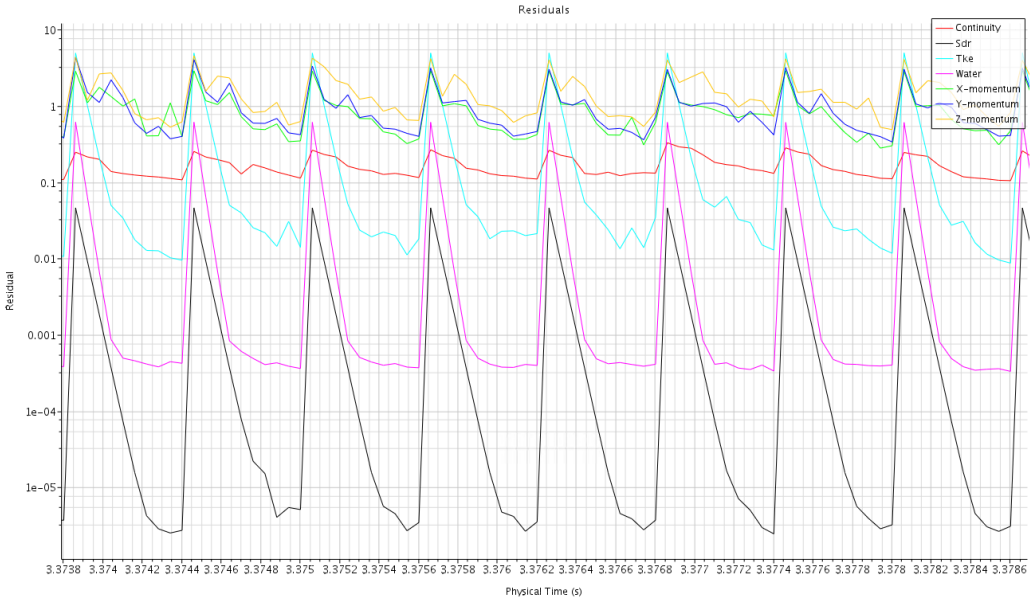

Figure 5.4: Residuals where the iterations for each time step is showed

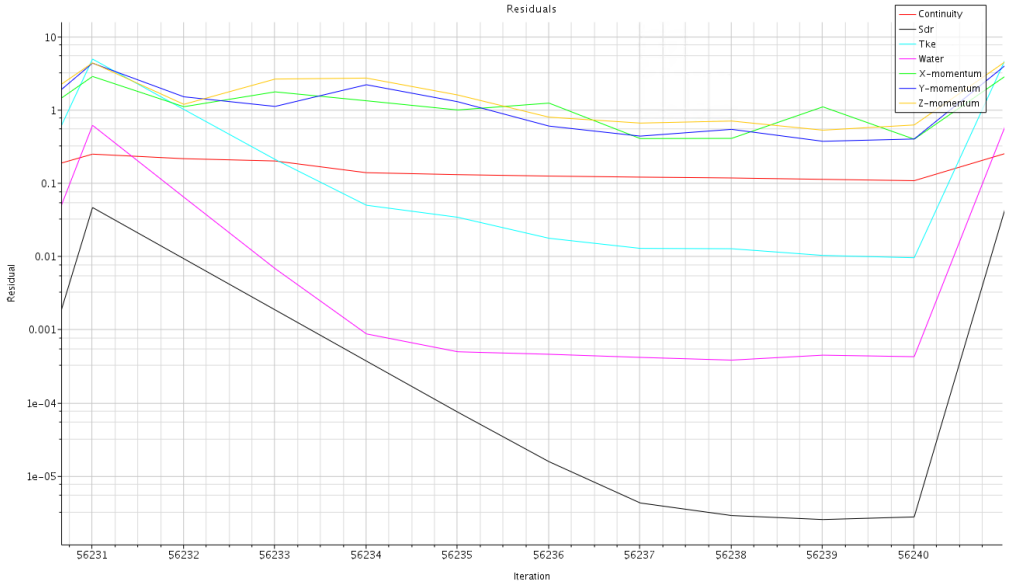

Figure 5.5: Residuals for one time step

An analysis to find the most efficient and precise number of inner iterations were conducted for respectively 6, 10 and 14 inner iterations. All the simulations were conducted with the same mesh and grid configuration for a time step of 0.6 ms, which was found from 0. With 10 inner iterations, the residual values seem to flatten out and converge at the end of each Δt after approximately 8-9 inner iterations, as seen in Figure 5.4 - Figure 5.5. Hence, 10 iterations are chosen as a basis for the varies simulations and 4 DOF-solver iterations.

5.1.3 CFL number analysis

Two different simulations with a time step of 1.2 ms and 0.6 ms were conducted to determine the sensitivity of the simulation with respect to the CFL value.

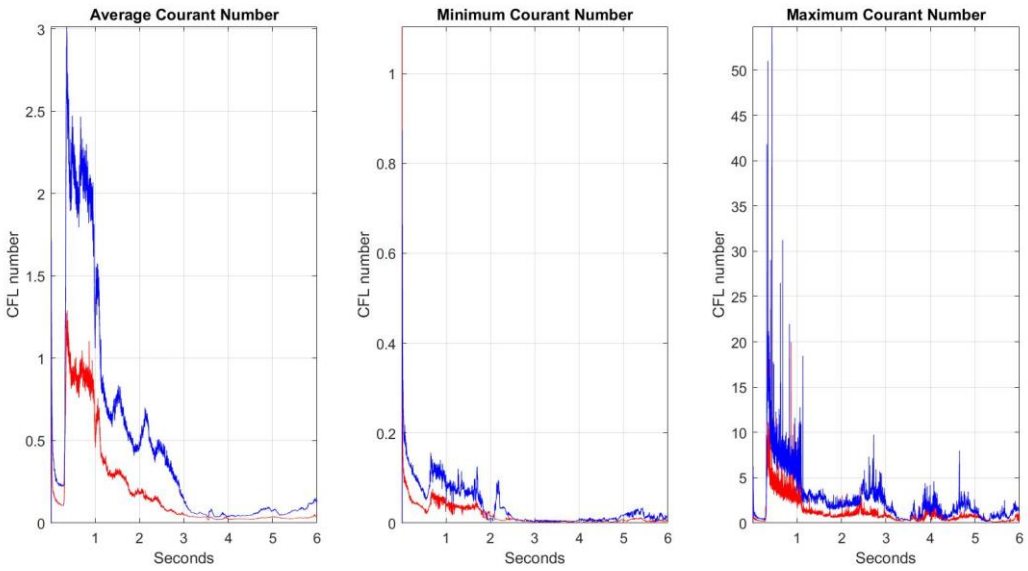

Figure 5.6: CFL values for free surface interaction, where blue is for Δt=1.2ms and red is for Δt=0.6ms

As described in section 3.3.4 the CFL number gives an indication of the ratio between the simulated fluid distance for a given time step, Δt, and the length of one cell, Δx. The values in the plots above are measured in the aft part of the body where the air cavity is located. The CFL plots for the two given time steps, seem to have the same trend, where the simulation with the lowest time step corresponds with lower CFL, which is reasonable.

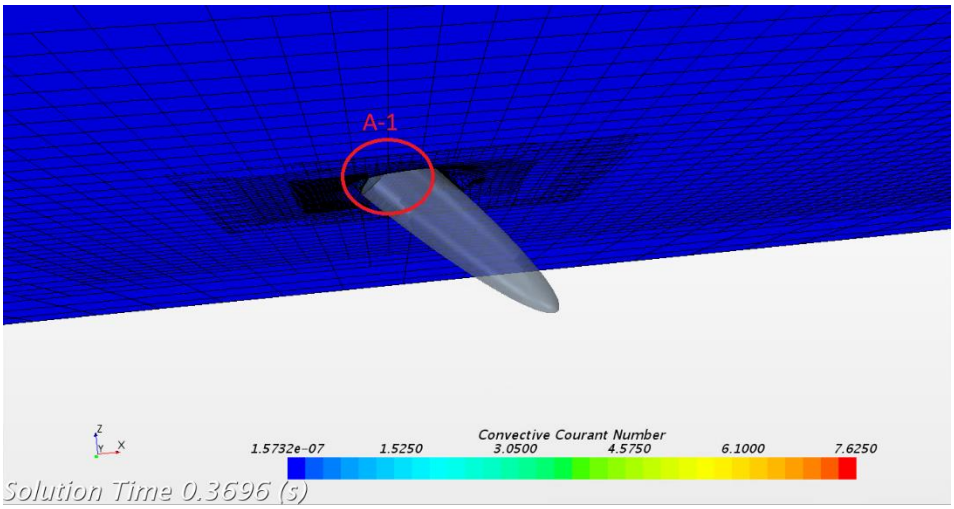

Figure 5.7: Courant scene for a global view at the end of water entry phase

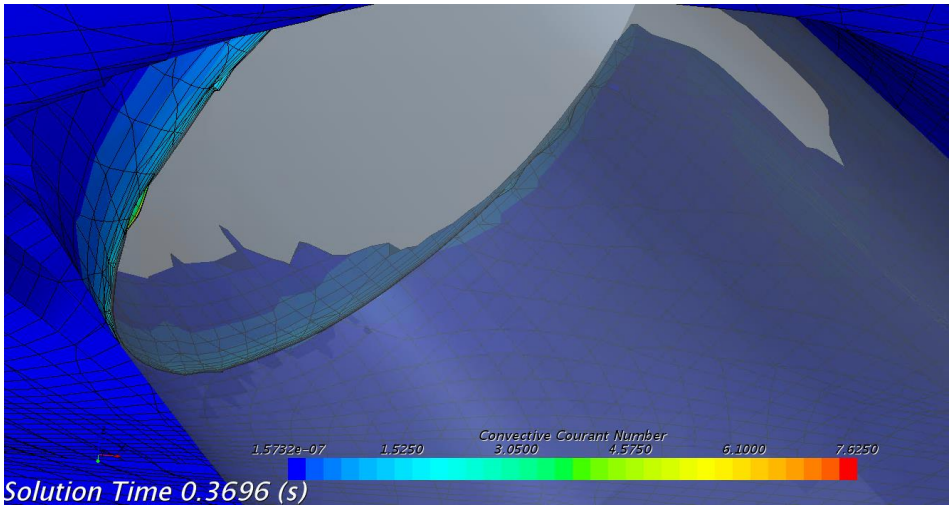

Figure 5.8: Local Courant scene from cut A-1 in Figure 5.7

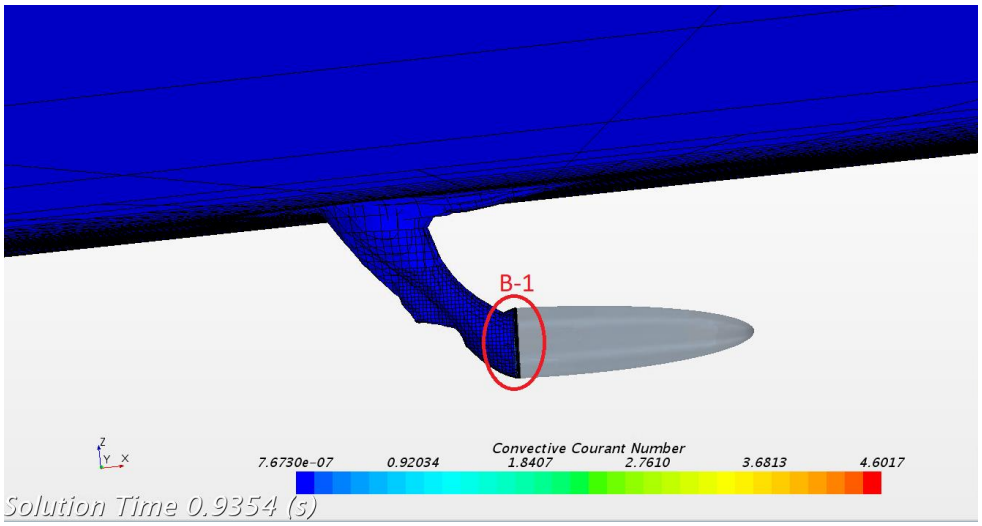

Figure 5.9: Global Courant scene right before cavity closure

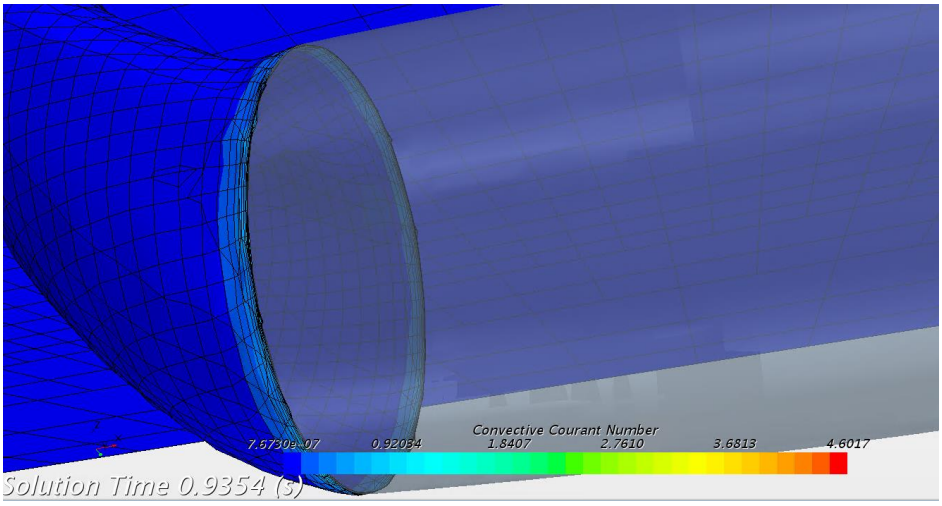

Figure 5.10: Local Courant scene right before cavity closure, cut B-1 from Figure 5.9

Both Figure 5.8 and Figure 5.10 shows the local CFL number, which indicates that the value has its maximum in the sharp corner on the aft part. This corresponds well with increased fluid acceleration around corners, and smallest cell size closest to the lifeboat surface (prism layer).

5.2 Convergence Study

In pursuance to investigate the convergence of the solution, the cell sizes in the grid has been changed. All the cells within the coarsest grid has been halved ones for the medium grid and twice for the finest grid. In order to have a more reliable convergence study, this is also done for the

timestep. Then the CFL-number will be quite similar, though cell sizes is different. Meaning that the main parameter influencing the solution will be the cell size. An overview of the meshes is given in Table 5.1, and for the prism layers in Table 5.2. The parameters that will be investigated in this convergence study is acceleration, motion and pressure on the aft part of the lifeboat. The plots are integrated for global convergence and local points are selected for interesting points of time.

SMALLEST CELL SIZE $[m]$	DISCRETIZATION	# CELLS LOCATED IN THE DOMAIN	# CELLS LOCATED IN THE OVERSET	TIMESTEP $[s]$
0,16	Δx_3	88 186	203 043	0.0006
0,08	Δx_2	585 083	1 003 599	0.0003
0,04	Δx_1	4 409 925	6 839 080	0.00015

Table 5.1: Mesh description, where the cell sizes from the prism layer is excluded as smallest cell

	Δx_3	Δx_2	Δx_1
# OF PRISM LAYERS	12	10	16
TOTAL PRISM LAYERS HEIGHT [M]	0.31858	0.1527	0.16023
STRETCH FACTOR	1.4983	1.516	1.2419
CELL HEIGHT CLOSEST TO THE BODY [M]	0.00125	0.00125	0.00125

Table 5.2: Prism layer specification for each mesh discretization

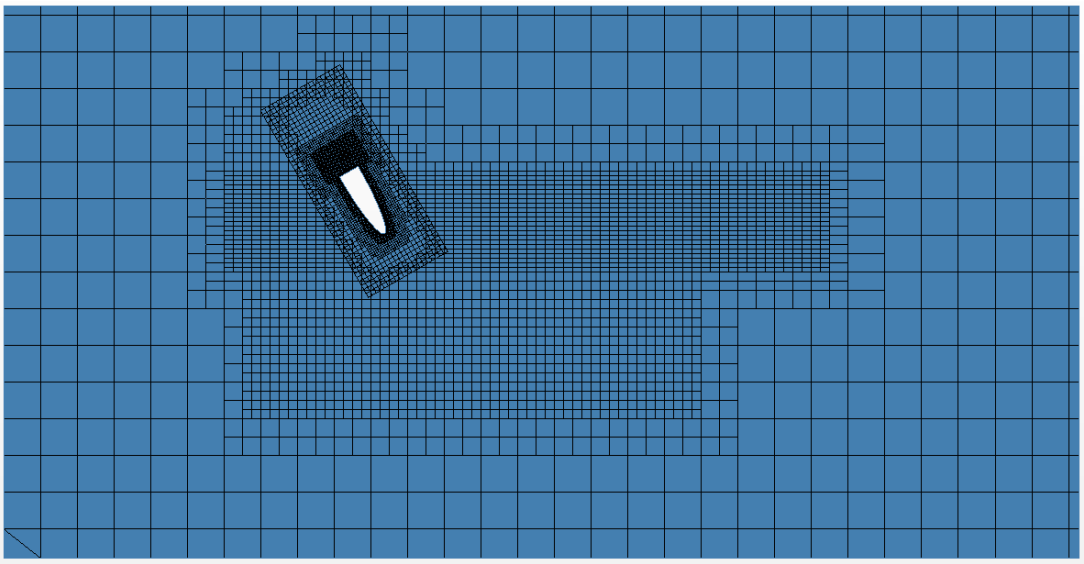

Figure 5.11: Mesh with 0,16 m as smallest cell, discretization Δx_3

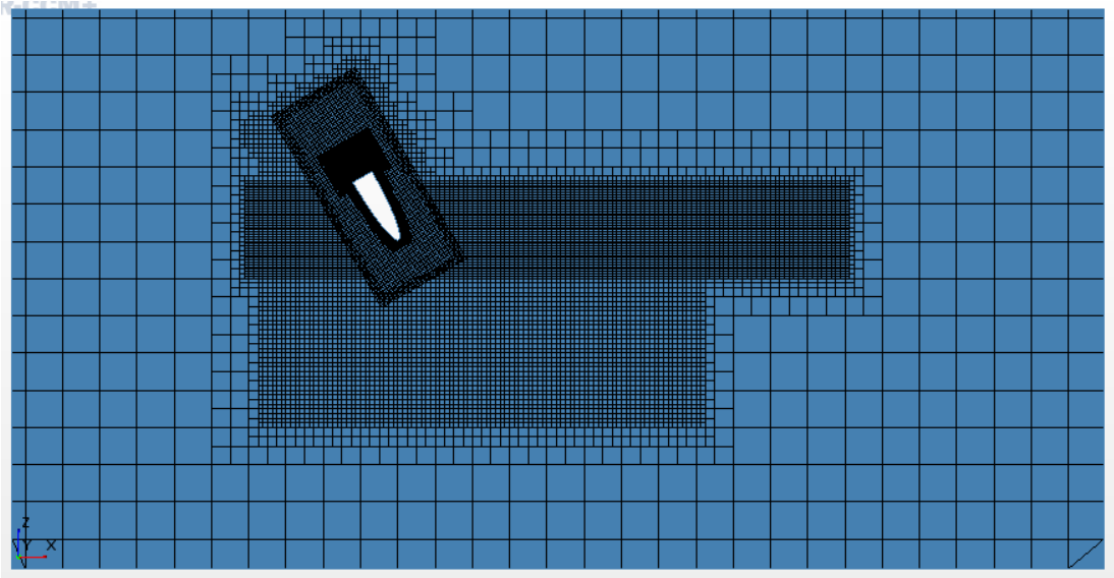

Figure 5.12: Mesh with 0,08 m as smallest cell, discretization Δx_2

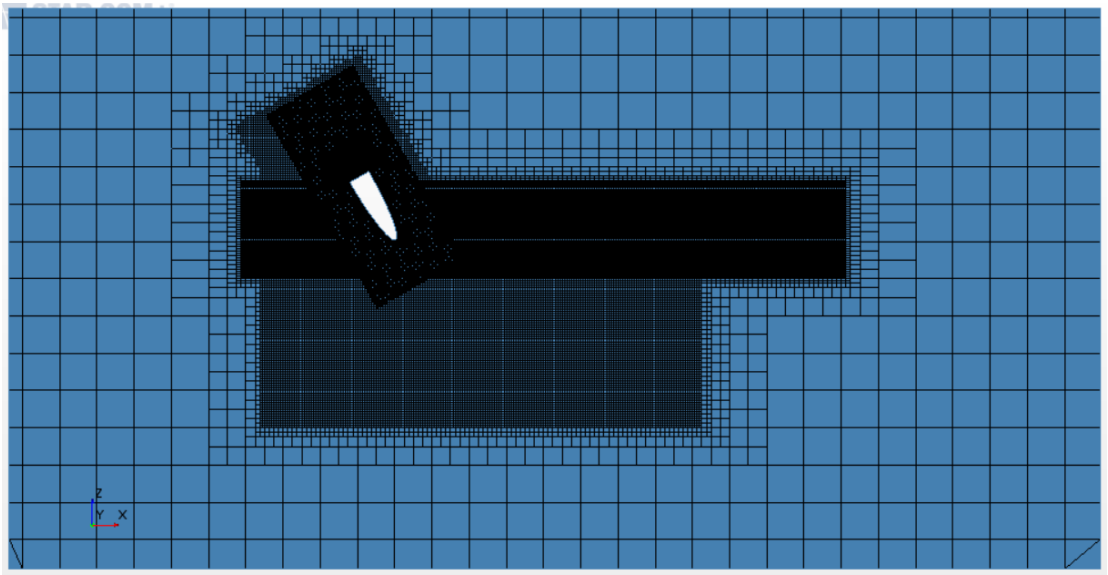

Figure 5.13: Mesh with 0,04 m as smallest cell, discretization Δx_1

As seen in Figure 5.11 - Figure 5.13 it is not only the cells located around the body that is reduced in size, the water surface and overlap regions are also reduced in size in the same manner as the cells around the body. This is because of the overset mesh interaction with the domain, and it is recommended by the user guide that the overset cells are of similar size as the overlap cells. (Steve CD adapco, 2016)

A convergence study has been carried out, inspired by the paper written by Colicchio, et al. (2006). Assuming that the error approximated for a given quantity, q is proportional to Δx^{OA}. OA is the order of accuracy and has been defined as:

[36]

$$OA := \frac{\log\left(\frac{\left|I_g(\Delta x_2) - I_g(\Delta x = 0)\right|}{\left|I_g(\Delta x_1) - I_g(\Delta x = 0)\right|}\right)}{\log\left(\frac{\Delta x_2}{\Delta x_1}\right)}$$

$I_q(\Delta x_1)$ and $I_q(\Delta x_2)$ are integrated values of given quantity, q, predicted numerically for discretization Δx_1 and Δx_2, representing different mesh resolutions. $I_q(\Delta x = 0)$ represent the exact time integral of the quantity q. Positive values are desired, where larger values mean that the results converge faster to a specific value. Since there has not been conducted experiments for similar lifeboat geometry and very small cell sizes causes too large CPU time, the exact integrated value for given quantities, $I_q(\Delta x = 0)$ is unknown. Hence, equation [36] has to be modified, where the exact solution can be derived by assuming a linear logarithmic relationship between $I_q$and Δx, by extrapolation from the integrals on three different meshes, $I_q(\Delta x_1), I_q(\Delta x_2)$ and $I_q(\Delta x_3)$. (Colicchio, et al., 2006)

[37]

$$-\frac{\log\left(\frac{\left|I_q(\Delta x_2) - I_q(\Delta x = 0)\right|}{\left|I_q(\Delta x_1) - I_q(\Delta x = 0)\right|}\right)}{\log\left(\frac{\Delta x_2}{\Delta x_1}\right)} = -\frac{\log\left(\frac{\left|I_q(\Delta x_3) - I_q(\Delta x = 0)\right|}{\left|I_q(\Delta x_2) - I_q(\Delta x = 0)\right|}\right)}{\log\left(\frac{\Delta x_3}{\Delta x_2}\right)}$$

The numerical solver uses a 2. order convection scheme. Hence, in order to have a satisfactory convergence, the order of accuracy should have a value close to 2.

Since the order of accuracy mostly is determined by integrated quantities, it is important to consider which time interval that is of interest and provide accurate predictions. Time intervals where the various plots intersect, will alter the accuracy since the integrated values may be of similar measure, even though the shape is not. Therefore, the first time interval (yellow area) is chosen from 0.22 s - 0.75 seconds, the second time interval is for the cavity closure peak (blue area) chosen from 0.985 s – 1.0125 s and the third time interval (purple area) chosen from 1.4 s – 2.4 s, shown in Figure 5.14

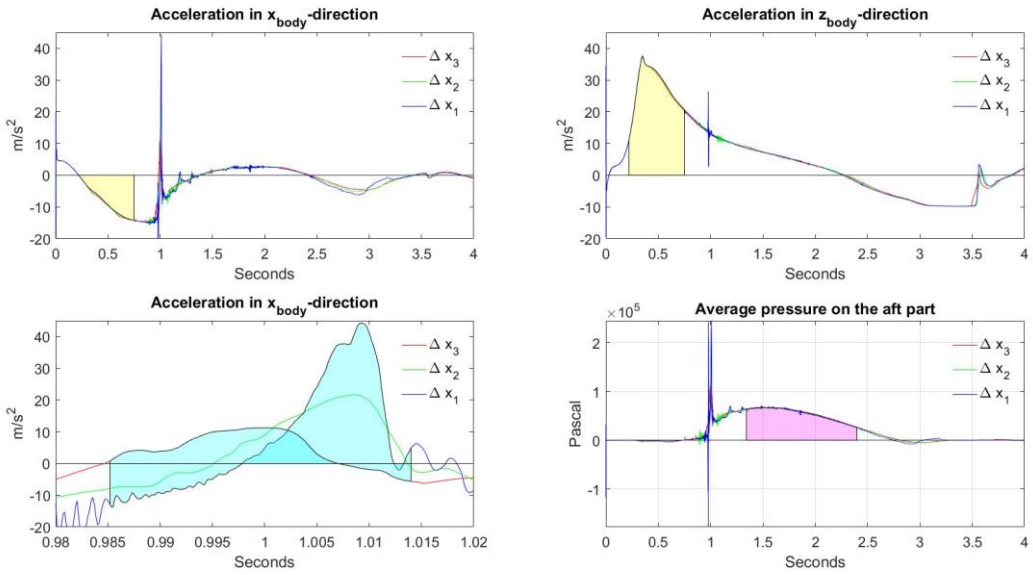

Figure 5.14: Convergence plots, where yellow is the time instance of 0.22 s – 0.75 s, blue 0.985 s – 1.0125 s and purple 1.4 s – 2.4 s

DESCRIPTION OF VALUES	TIME INTERVAL/SINGLE POINT	ORDER OF ACCURACY (OA)
INTEGRATED VALUE OF ACCELERATION IN x_{body}	0.22 s - 0.75 s (water entry phase)	0.545
INTEGRATED VALUE OF ACCELERATION IN z_{body}	0.22 s - 0.75 s (water entry phase)	0.958
INTEGRATED VALUE OF ACCELERATION IN x_{body}	0.985 s - 1.0125 s (air cavity closure peak)	1.190
INTEGRATED VALUE OF AVERAGE PRESSURE IN AFT PART	1.4 s – 2.4 s (Submerged phase, post air cavity closure)	0.546
CAVITY CLOSURE TIME	Single point	3.807
MAXIMUM SUBMERGENCE, z_{global}	Single point	1.384

Table 5.3: Order of accuracy for different integrals and points for selected time intervals and point of time.

All the measures of the order of accuracy are positive, indicating that the two finer grid discretization are more similar then the coarsest for the given quantities. Even though the plots shown in Figure 5.14 are very similar, they do not seem to converge with the order of accuracy that is expected for the solver. As mentioned above, intersection for the varies plot, will alter the reliability of the integrated quantities. This theory gets strengthen, since the OA is significantly higher for single point

values, though the cavity closure time indicates a convergence rate, faster than the solvers accuracy. Another error source influencing the order of accuracy, might be the turbulence and corresponding Y^+ model applied. A hybrid model of the Y^+ model was chosen because of the density differences, as mentioned in section 3.3.3, Wall Y^+. The code used for modelling of various Y^+ ranges for the hybrid model are not shown in the manual, hence an inaccurate solver method is not unlikely. As for the turbulence, the solver struggled to model the turbulence when the aft part intersected with the free surface even though a relatively low time steps were applied. This will surely alter the order of accuracy, even though it is of secondary importance for short duration of impact problems with flow separation from sharp corners. (Faltinsen & Greco, 2013) The low values in OA can also be caused by the inaccuracy of the coarsest mesh. If the mesh is to coarse, it can lead to large unreal manifestations in the solution. A finer mesh may result in a more satisfactory OA. For the peak interval in Figure 5.14 for the body fixed x-accelerations, it is easy to see that there is no local convergence due to the large difference in shape of the plot, even though the OA is quite high. However, the trend seems to converge, as the closure time is almost the same for the two finest grids and the maximum submergence point only have a difference of 4 cm between the finest grid and the coarsest grid, which implies global convergence.

DISCRETIZATION	**SOLVING TIME** $[\boldsymbol{hours}]$	**# OF PROCESSORS**	**CPU COST**
$\boldsymbol{\Delta x_3}$	25	9	225
$\boldsymbol{\Delta x_2}$	51	39	1989
$\boldsymbol{\Delta x_1}$	150	272	40800

Table 5.4: Mesh discretization with its specific solving time, number of processors used and computational cost

The solution does not seem to have local convergence. However, the quite similar position plots show that the local accelerations do not have large manifestations in the global behaviour of the body. It is assumed that the finest mesh gives the most accurate results, but it is not computational economic. The second finest mesh has a global solution very close to the finest one. Hence, a compromise between computational time and accuracy is made, and Δx_2 is the chosen mesh discretisation for further studies in this thesis.

6 Results with initial conditions

As concluded with in 5.2, the results presented is obtained with the Δx_2 mesh discretization. This is due to the low CPU cost for each simulation, as well as section 5.2 concludes with that this discretization gives accurate results for most of the phases. This will also give a better representation of the comparison of a change in different parameters in section 7, where this discretization has been used. The results are obtained with an initial condition seen in Table 6.1.

CONDITION	VALUE	DIMENSIONS
WATER ENTRY ANGLE	60	degrees
VELOCITY$_{\text{BODY FIXED}}$	[20, 0, -5]	m/s
ANGULAR ROTATION	15	degrees/s

Table 6.1: Initial conditions

a)

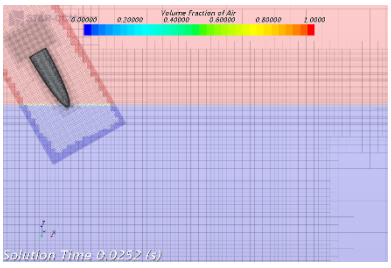

b)

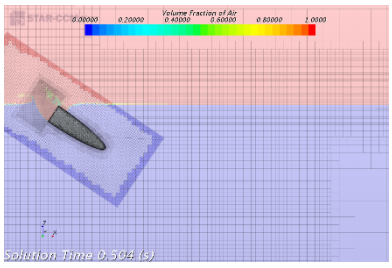

c)

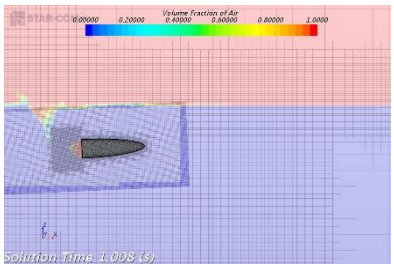

d)

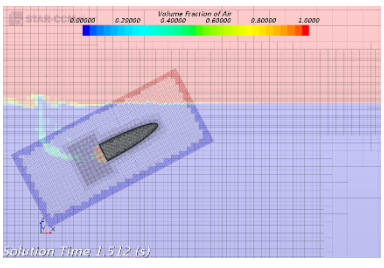

e)

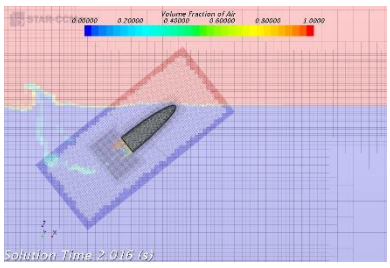

f)

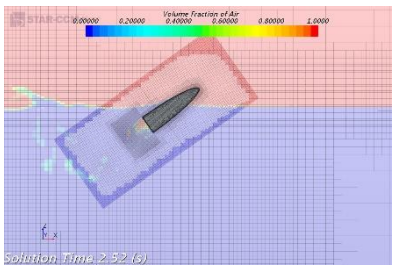

g)

h)

i)

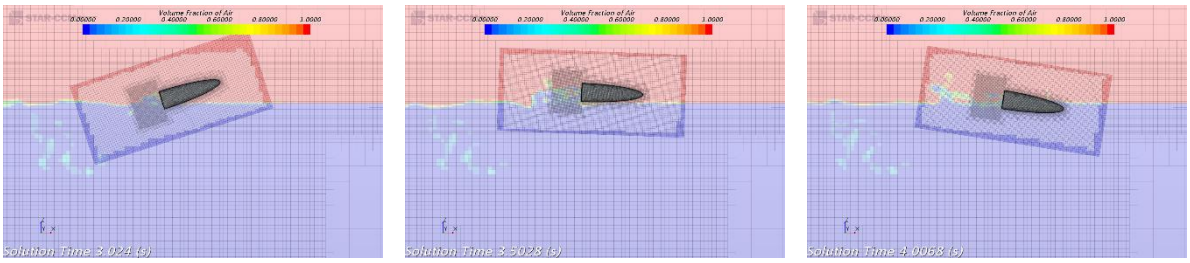

Figure 6.1: VOF of air representation of the path from water entry to sail away

From Figure 6.1 it is possible to see the global behaviour of the path of the lifeboat with its initial conditions.

6.1 Acceleration and angular acceleration

The acceleration results are divided into the different phases the lifeboat goes through, from water entry to sail away phase. The air cavity formation and collapse are also included here.

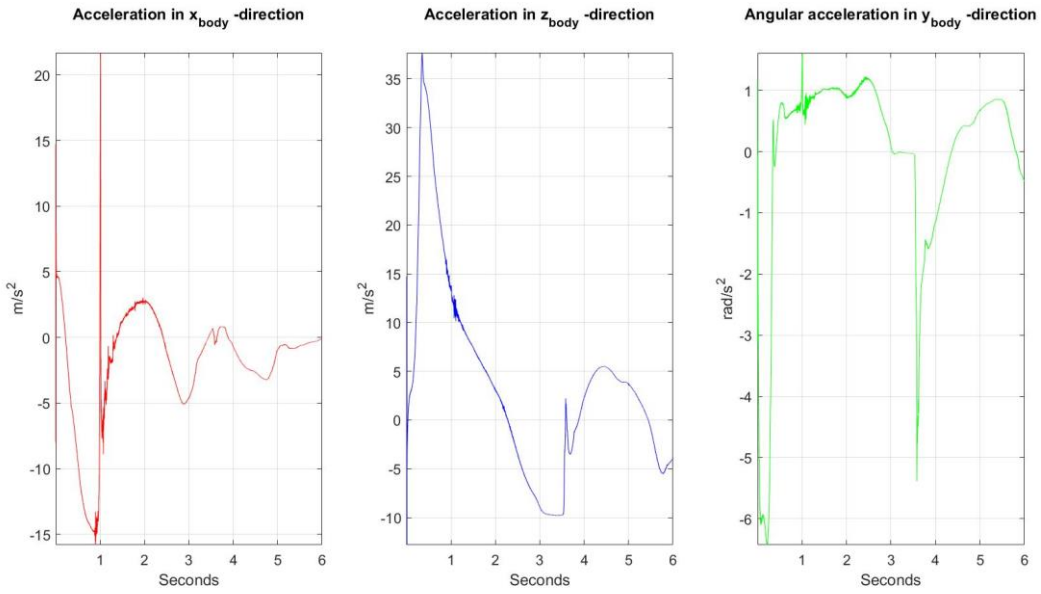

Figure 6.2: Acceleration and angular acceleration measured in the body fixed coordinate system

6.1.1 Water entry

The body has an initial free-falling acceleration, with a constant clockwise rotational velocity, until the water entry starts after 0.0085 s. As the lifeboat bow enters the water it is subjected to slamming forces. As mentioned in section 4.4, the segregated flow solver does not give a good representation of this phenomenon. From the acceleration plot (Figure 6.2), it is possible to see that the initial acceleration is counteracted in both x_{body} and z_{body}. The body will also get counter clockwise angular acceleration, the rotation is decreased and eventually reversed in the water entry. This occurs as the centre of gravity gets pulled down, while the bow is partially constrained in the fluid. When the added mass increases, there is a small clockwise angular acceleration which is slowly increasing for a while.

6.1.2 Air cavity formations

In the acceleration plot from Figure 6.2, the air cavity closure appears as a the large peak in x_{body} acceleration. It is caused by the pressure from the water on the newly formed air bubble located on the aft part of the body. The air in the bubble is modelled as incompressible. A consequence regarding this, is that the entrapped air bubble is rigid, hence the appearance of a single peak with a high value. The air in the entrapped bubble is in fact compressible, the acceleration plot is therefore not realistic at the point of air cavity closure. It is expected that the entrapped air bubble will oscillate in size, and that the first peak will be less pronounced than the peak in Figure 6.2.

a)

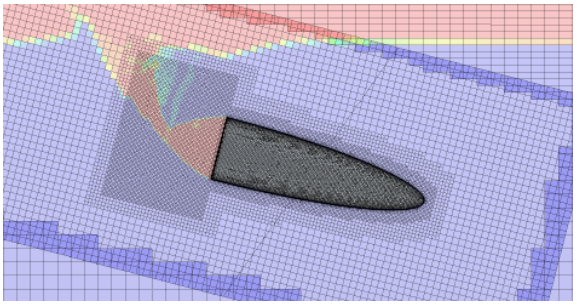

b)

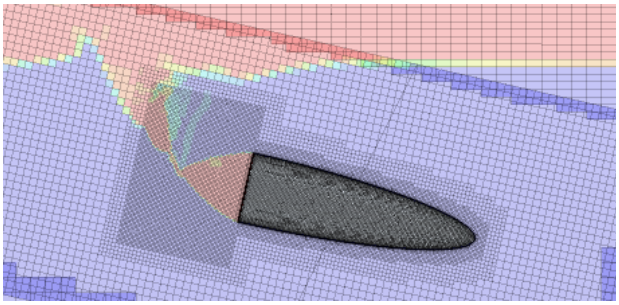

c)

d)

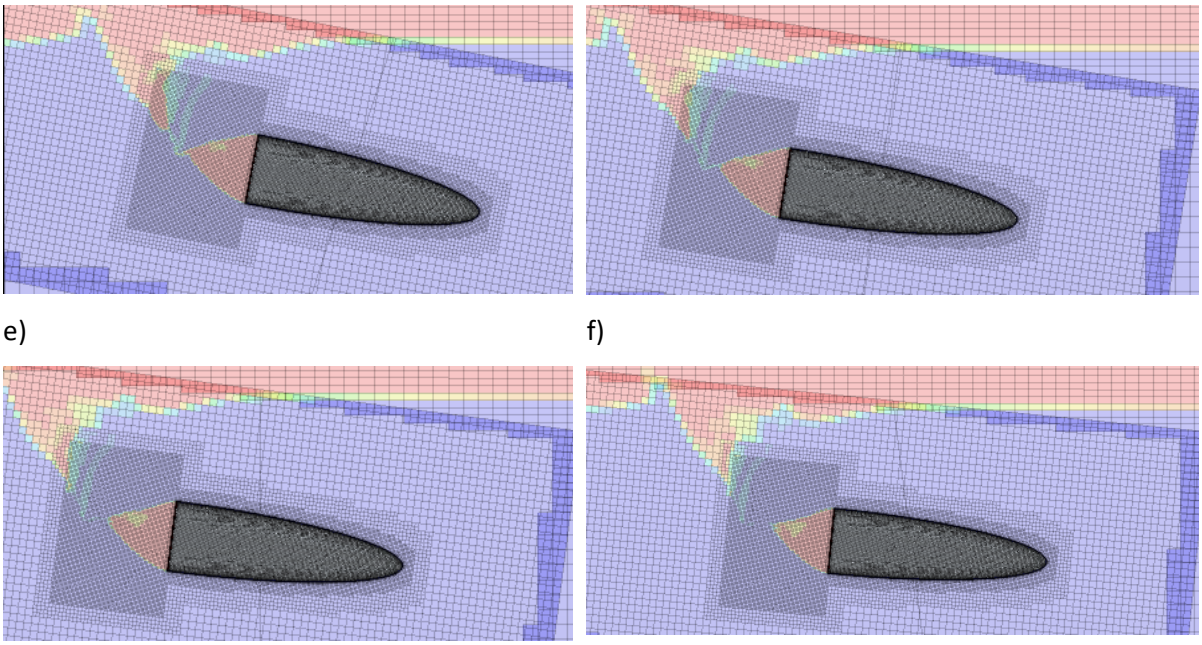

e) f)

Figure 6.3: Beginning of the air cavity closure, 2-D, starting from solution time 0.756s with $\Delta t = 0.025s$, until 0.882s

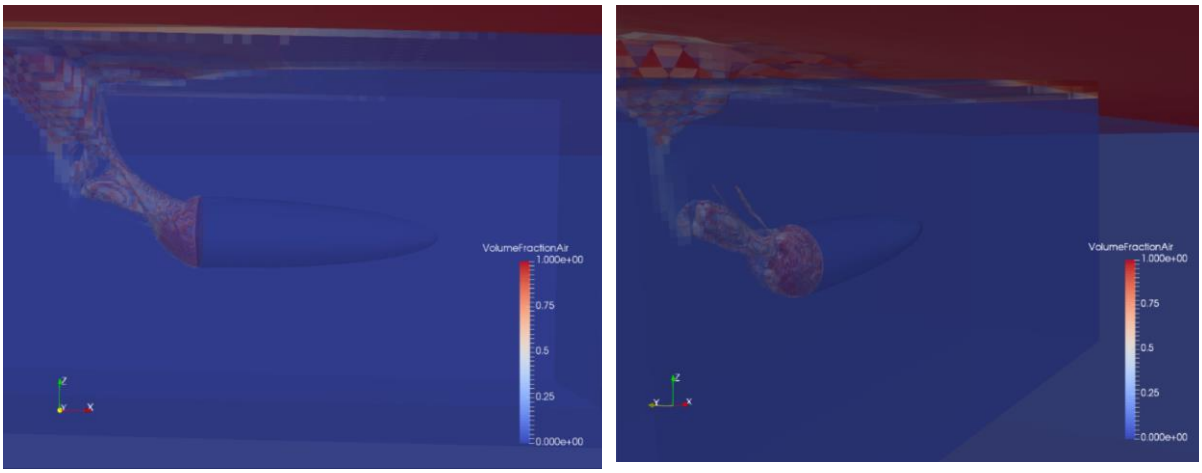

a) b)

Figure 6.4: Visualization of the air cavity closure in 3D where a) shows the solution time 1.002 s and b) shows solution time 1.102 s

Figure 6.3 shows the air cavity and the beginning of the closure in the period between Figure 6.1 b) and c). As the pictures are in 2D, it is difficult to see the exact moment of air cavity closure later in the time-series. A 3D representation of the air cavity closure is shown in Figure 6.4.

6.1.3 Submerged phase after air cavity formation

The body will continue to rotate, and eventually the x_{body}-direction will be parallel to the water surface. At this position, the body is close to maximum submergence. The body still has a counter clockwise rotation, this can be seen in Figure 6.5. Shortly after maximum submergence, when the bow is turning upwards, the x_{body} motion and the buoyancy force will both have a positive contribution in the global z-direction. The point can be seen at 1.375 s in the x_{body} acceleration in Figure 6.2, where the body gets a positive acceleration contribution. There is a positive x_{body} acceleration contribution until the point where the gravitational forces excide the buoyancy forces at the water exit.

6.1.4 Water exit

As the body exits the water, the buoyancy acts upwards on the aft part, while the gravitational force acts downwards on the fore part. This creates a large increase in clockwise rotation, while the body gets deaccelerated in the negative vertical direction by the gravitational force. The small positive x_{body} acceleration from the gravitational force before re-entering the water, is due to the x_{body}-motion changes in the vertical global direction. As the body has a certain pop-up height, it is subjected to a second slamming at the re-entering of the surface. It is apparent as the peak at 3.6 s in z_{body} acceleration, Figure 6.2.

6.1.5 Sail away phase

After water exit and the second water entry, the body will have a negative acceleration in the body fixed x-axis as it is slowed down by resistance forces, and the only thing driving it forward is the initial water exit velocity.

6.2 Velocity

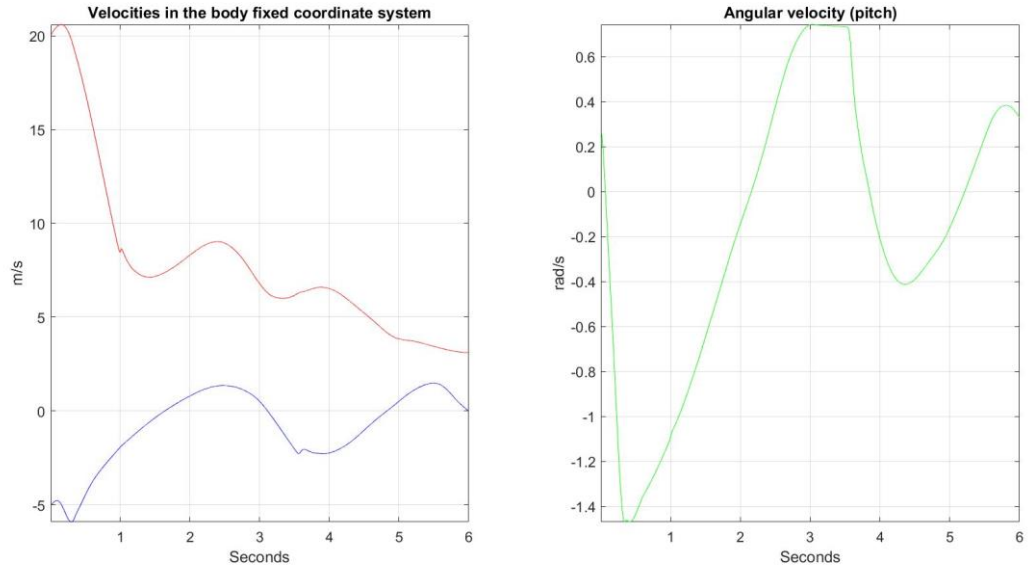

Figure 6.5: Velocity plot where the red is in the x_{body} -direction and blue in z_{body} -direction

The body fixed velocity in x-direction reaches its maximum value after approximately 0.25 seconds. After initial impact the velocity is rapidly decreasing. The body is resurfacing at 2.45 s, this is noticeable in the velocity plot as the body fixed velocities in both x and z has a local maximum for this point. The velocity plot is smother than the acceleration plot, which is logical as the acceleration is the time derivative of the velocity. The large acceleration peaks for the point of air cavity closure and second water entry are shown to have little effect on the velocity, they are noticeable as small discontinuities in the plot at 1.0 s in x_{body} and at 3.5 s in z_{body}, respectively. At 6 s, the body has a positive velocity in x-direction. This is beneficial as the sail away distance will increase as the time passes.

6.3 Motion

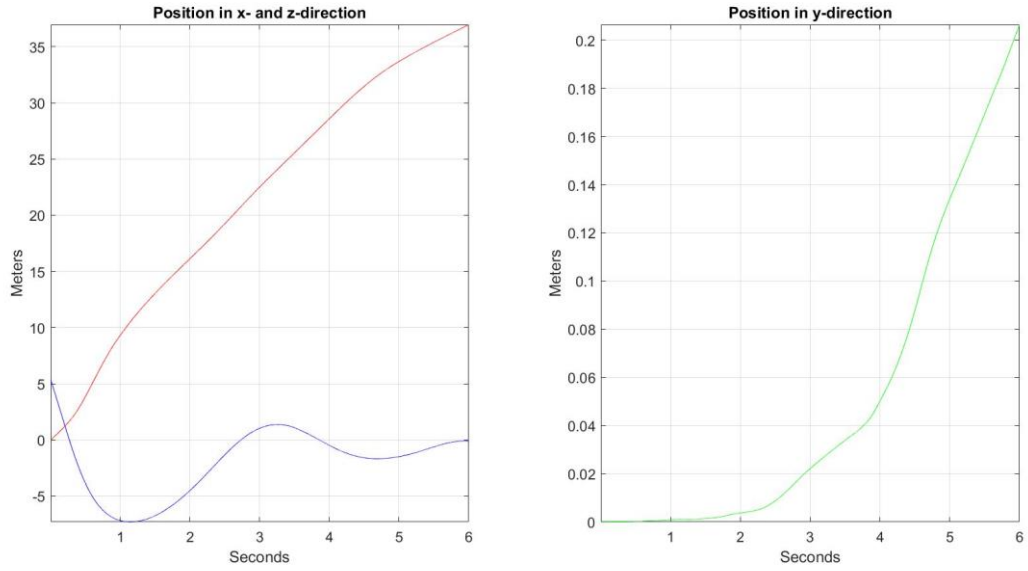

Figure 6.6: Position plot, where the red line is in the x-direction, blue in the z-direction and the green in y-direction

The position is the time integrated velocity. Figure 6.6 shows a continuous line which imply that the impulse forces inflicted at air cavity closure and at the second water entry are not large enough to make sudden changes in the position. The lifeboat reaches maximum submergence after approximately 1.2 seconds with a depth of 7 meters. After 6 seconds, the lifeboat has managed to sail 36 meters away from the point of initial water entry. As seen in Figure 6.5, the velocity is still positive at 6 s, which leads to an increase in sailing distance later on. By comparing the lifeboat motion in Figure 6.6 with Figure 2.8, the lifeboat trajectory shows resemblance with motion pattern 1, where the lifeboat pitches significantly at maximum submergence and ascent so that it surfaces with a positive forward velocity, as seen in Figure 6.1. According to DNV-GL, this is the preferred trajectory. (DNV-GL, 2016)

6.4 Pressure aft

The pressure on the aft part is mostly affected when the body is in the submerged phase, hence this is the period that will be discussed. To be sure of structural integrity in the aft part, e.g. for a weak part like a door, filtering of the pressure peaks is not an option since these large oscillations can

results in local structural failure. Hence, the air cavity should ideally be modelled as compressible for such calculations to be utilized, as Tregde (2015) concludes with in his paper. (Tregde, 2015)

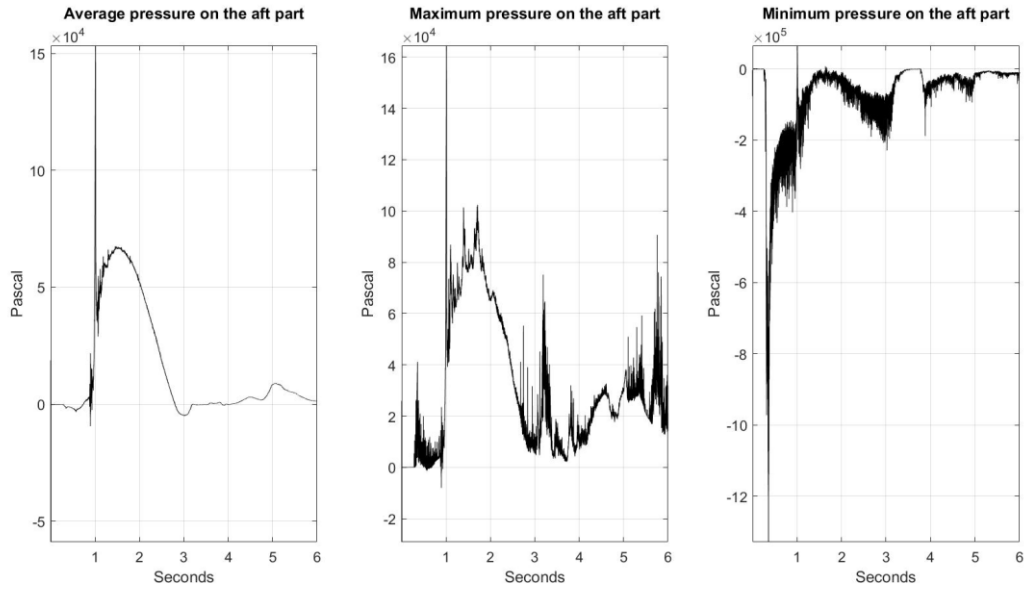

Figure 6.7: Pressure plots on the aft part

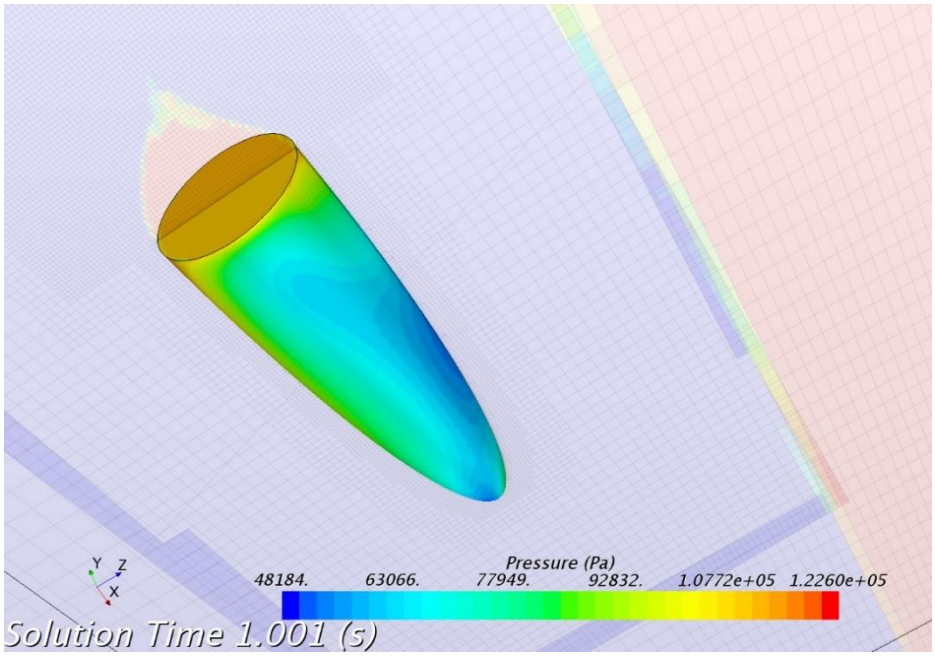

Figure 6.8: Pressure distribution on the lifeboat 7ms before the peak

The pressure is proportional to the acceleration, which means that the peaks should appear at the same distinctive time. By comparing Figure 6.2 and Figure 6.7 is it possible to see the resemblance of

this. The air cavity closure is seen as the large peak in Figure 6.7 for average, maximum pressure and also a smaller positive peak for the minimum pressure. Figure 6.8 shows that the high pressures is in the area where the air cavity is located and the lower pressures seen in the minimum pressure plot, Figure 6.7, is in the area where the air cavity ends and water attaches to the body. Throughout the submerged phase, the average pressure and maximum pressure in Figure 6.7 follows the same tendency. As seen in Figure 6.8 the pressure is close to uniformly distributed on the aft part during this phase. The pressure increases until the air bubble is at maximum submersion, due to the hydrostatic pressure. After this the pressure is decreasing until the aft part is above the calm water level.

a) b)

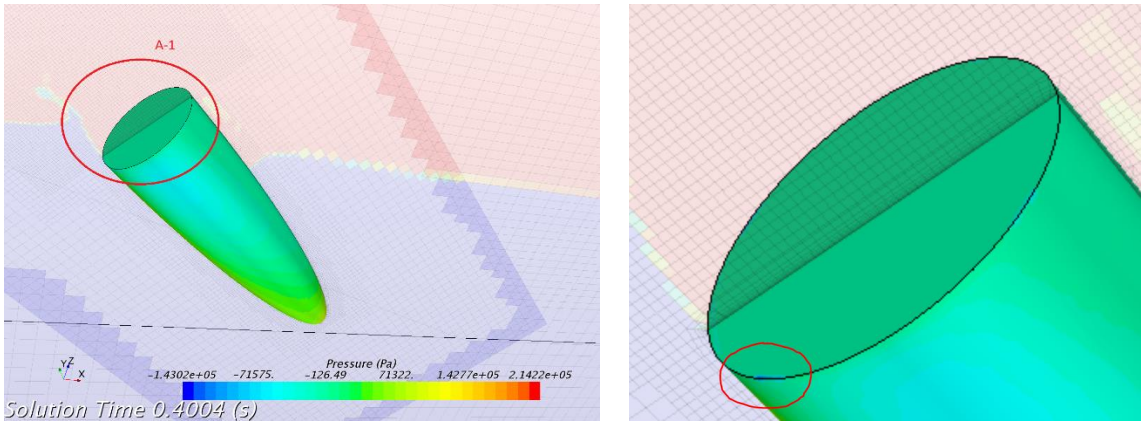

Figure 6.9: Minimum pressures from the splash crown, where a) shows the global and b) more locally of the same time instance

As seen in Figure 6.7 the minimum pressure has large negative values at approximately 0.4 s – 0.6 s, this indicates that the water entry splash crown and the air cavity formation creates a suction on the aft part. This is illustrated in Figure 6.9.

6.5 Comparison with theory

6.5.1 Air cavity investigation

As mentioned in 0, high Capillary number is beneficial to ensure air cavity formation. An air cavity was therefore expected, due to the relatively large viscous forces compared to the surface tension in water and the sharp corners in the aft part. In addition, surface tension has been neglected for the simulations due to its insignificance in the case of lifeboat diving, as mentioned in 2.3.2. For Bond

number higher then 10^3, only deep and surface seal occurs, where the transition from deep seal to surface seal occurs for $Fr > \sqrt{150}$. This corresponds to a velocity greater than 60 m/s for the body in this thesis. Hence, deep seal is expected, corresponding well to Figure 6.3. f).

In section 2.4.3, the derivation between Froude number and closure time is obtained in equation [14]. From studying the VOF-picture at approximatly1 s, a deep seal is apparent. The air cavity height is clearly less than one half of the distance travelled from the entry point in the water surface to the aft part of the body. By studying the VOF-pictures, the aft part of the body gets submerged after 0.4284 s, and the air cavity initiation starts after approximately 0.6 s. The air cavity seems to be largest in diameter for this time instant, meaning that the expansion time is short compared to the collapse time, since the collapse seems to happen at approximately 1.0 s. This results in a closure time $T_c = t_0 + \delta t_2 = 0.17\ s + 0.4\ s = 0.57\ s$. Then by solving equation [14] with a characteristic diameter of 3 m, and a velocity of 20 m/s, the theoretical closing time is calculated to be

$$T_c = \frac{3m}{20m/s}\left(\frac{3}{2^{5/3}}\right)\left(\frac{20m/s}{\sqrt{9{,}81m/s^2 * 3m}}\right)^{2/3} = 0{,}34\ s$$

The body investigated in this thesis has a long cylindrical shape, but the dimensions, centre of gravity and density is somewhat different than the body investigated in the paper from Yan, et al. (2009). (Yan, et al., 2009) An important assumption was that the cavity closure height, H_c was approximately $\frac{1}{3}$ of the cavity height H. For this case, the dimensions of H and H_c is difficult to measure, as the VOF pictures are in 2D. The main difference is that there is an oblique impact and a pitch velocity, the simplified lifeboat geometry has a low density and it is not axisymmetric as the centre of gravity is moved in z-direction. For this derivation, the vertical velocity is also assumed constant, though the decrease is significant. These differences prevent a good comparison.

6.5.2 Water exit

From theory (see section 2.5) the relationship between the pop-up height and the water exit velocity in the global vertical direction can be tested utilizing equation [16]. When the centre of gravity passes the water surface, the global vertical velocity is:

$$w_{global} = \frac{8.6m}{s} * \sin(27°) + \frac{1.25\ m}{s} * \cos(27°) = 5.02\ m/s$$

For the simplified case, then the pop-up height should approximately be

$$H_{pop-up} = \frac{v_{vert}^2}{2g} = 1.28\ m$$

From the motion plot, the pop up height is read to be 1.23 m, corresponding well with the assumption that energy is lost due to splash plume and wave making. (Truscott, et al., 2016)

6.6 Courant validation

An indication of the expected CFL were investigated for the coarsest grid discretization, mentioned in section 5.1. Therefore, a new validation is needed, though the time step used is two times smaller.

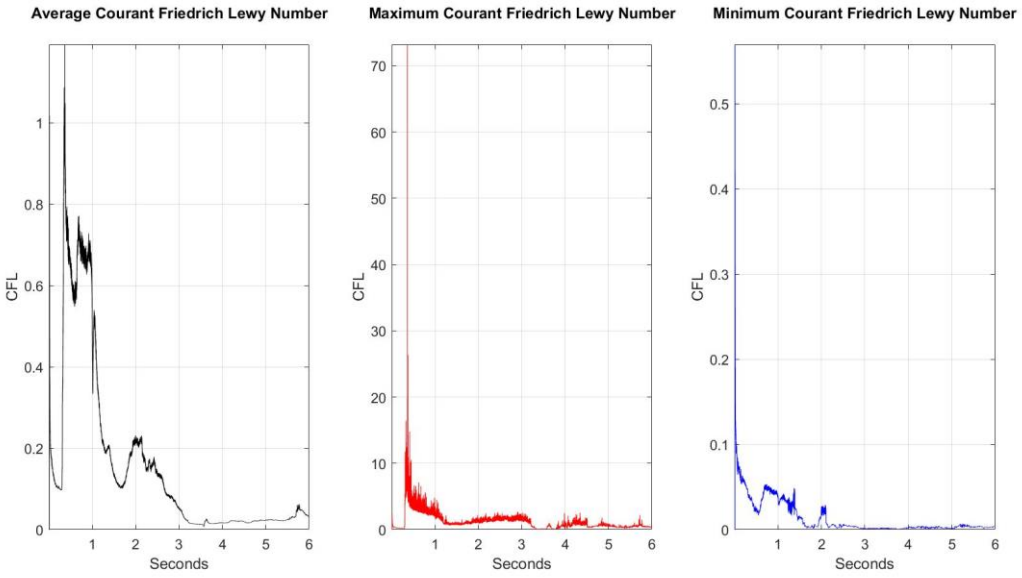

Figure 6.10: CFL number throughout the simulation

The average CFL number measured in the cells located around the aft part of the body bear resembles to the average CFL values for the coarsest mesh discretization, Δx_3, which is reasonable considering the solver approach for solving this value. There is still a distinctive peak at approximately 0.4 seconds, where problems related to solving the turbulence model occurred.

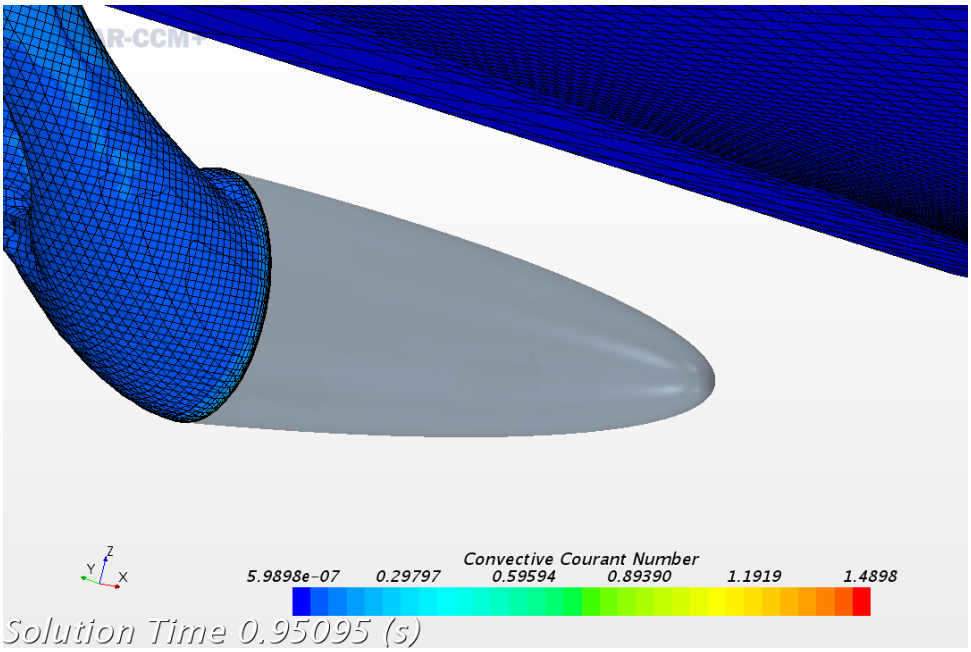

Figure 6.11: CFL visualization

The highest CFL values are still located around the sharp corners on the aft part of the body, but smaller in magnitude compared to the coarsest grid. This is probably a result of relatively similar prism layer distribution in terms of height for the varies mesh discretization's, though the time step is halved.

7 Parameter investigation

Since a lifeboat is a last resort solution of escaping the mother vessel, the weather conditions will not likely be ideal. The launching and free-falling phase can therefore be affected, which results in difference in the behaviour in the four later phases, as described in section 2. The water entry angle and the velocity are two parameters that can be affected by wind loads and by which wave phase it is entering. Also, the centre of gravity can change, as it depends on the number of passengers and their seating arrangement. Hence, an investigation of the effect these changes can have, has been carried out. The chosen values are shown in Table 7.1. Only one parameter will be changed for each simulation, in order to examining the influence of the different parameters. However, if the free-falling time and distance increases, both velocity and water entry angle is likely to increase.

PARAMETER		**-**	**IC**	**+**	**Δ**
$\boldsymbol{\theta}$	[°]	55	60	65	5
COG_z	[m]	-0.7	-0.5	-0.3	0.2
V	[m/s]	15.62	20.62	25.62	5

Table 7.1: Parameter investigation values

From these parameters, accelerations, velocities, air cavity formation, path and pressure has been studied to get an insight of how they are changing with the varying parameters.

7.1 Velocity

Three different velocities have been tested to investigate the effect they will have for the behaviour of the body. Their maximum values are 15.62 m/s, 20.62 m/s and 25.62 m/s. The ratio between the velocities in x_{body} and z_{body} is held constant.

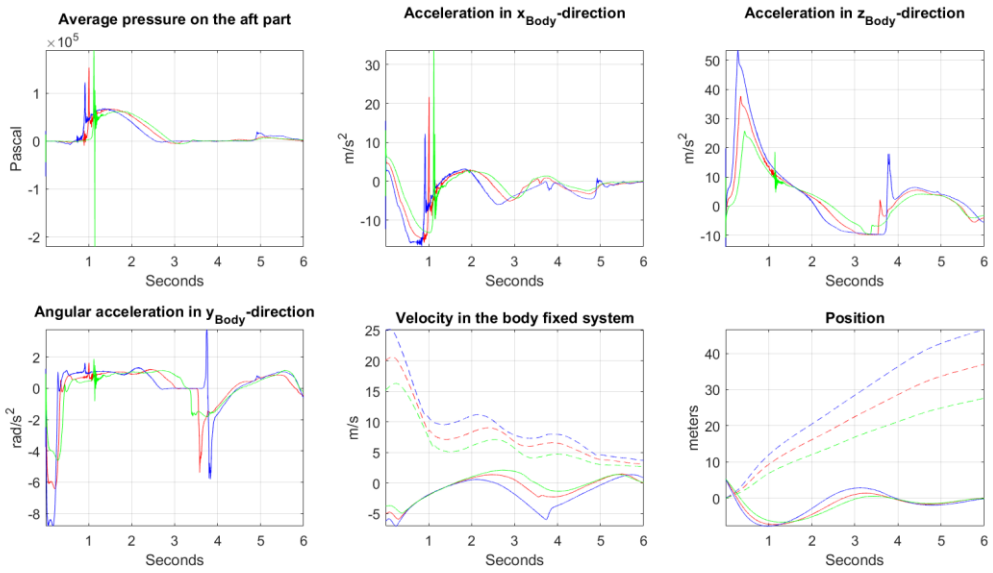

Figure 7.1: Green is 15.62 m/s, red is IC with maximum velocity 20.62 m/s and blue is 25.62 m/s. The accelerations and velocities are taken in the body fixed coordinate system. The dashed lines are in the x-direction, and the solid lines are in the z-direction in the velocity and position plots.

	15.62 m/s	**INITIAL CONDITION** **20.62** m/s	**25.62** m/s
CAVITY CLOSURE TIME (PEAK) $[s]$	1.121	1.009	0.915
WATER EXIT TIME $[s]$	3.073	2.730	2.366
POP-UP HEIGHT $[m]$	0.557	1.369	2.835
MAXIMUM SUBMERSION $[m]$	-6.633	-7.297	-7.700
SAILING DISTANCE AT 6 s $[m]$	27.635	36.969	46.619
VELOCITY x_{Body} **AT 6** s $[m/s]$	2.709	3.109	3.685
ACCELERATION PEAK MAGNITUDE $[m/s^2]$	33.720	21.678	12.189
MAX PRESSURE AFTER CAVITY CLOSURE $[kN/m^2]$	62.390	67.460	68.420

Table 7.2: Distinctive values for comparison the change in water entry velocity

The plots in Figure 7.1 reveal great differences. The accelerations in x_{body} and z_{body} is clearly largest for the high impact velocity case. It also has the most negative angular acceleration at the water impact phase, hence it will contribute the most to the counter clockwise rotation. The air cavity closure occurs earlier for the case with the highest velocity, this compares well with equation [14] The global horizontal velocity at the point of maximum submergence has a significantly larger value for the case with the highest initial velocity, than for the two other cases. This, combined with a

higher counter clockwise rotation, leads to high water exit velocity and angle. The result is an early water exit and a large pop-up height. As it "shoots" out of the water with high energy, it will get the longest sailing distance at 6 s. And since it also has the highest velocity at this point of time, it will have the best potential for sailing further away from the evacuation scene. The maximum submergence is also quite different, which is an important parameter since it is proportional to the hydrostatic pressure, when assuming constant density. High hydrostatic pressure is of concern for asymmetric geometry like appendages, as a result of the varying pressure loads. This can further cause implosions.

7.2 Water entry angle

A preferable water entry angle is approximately 60°. However, the different external forces affecting the lifeboat can change this. Three different water entry angles have been tested to investigate the effect they will have for the behaviour of the body. Their values are $55°$, $60°$ and $65°$.

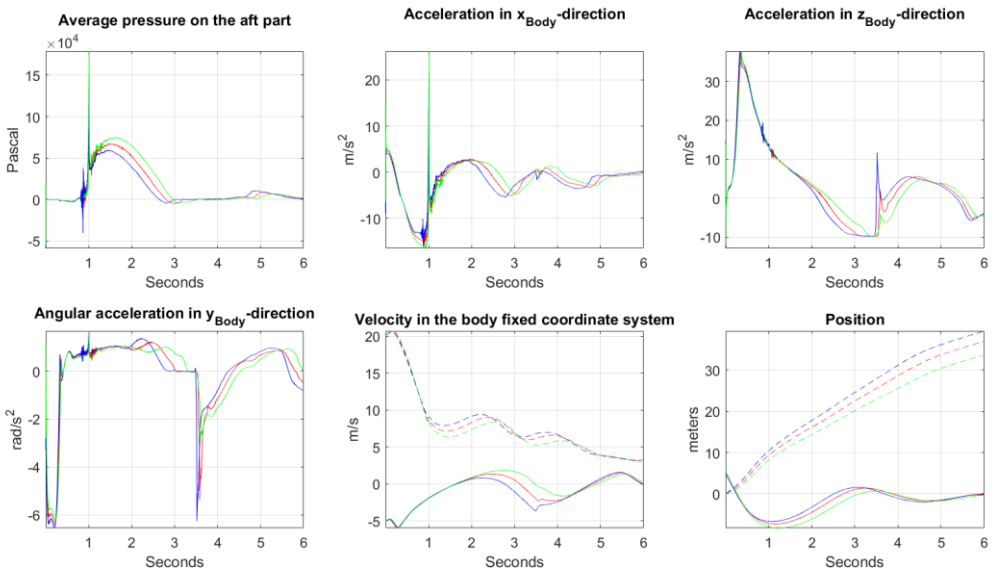

Figure 7.2: Plots of the results with different water entry angles, where blue is 55°, red is 60° and green is 65°. The accelerations and velocities are taken in the body fixed coordinate system. The dashed lines are in the x-direction, and the solid lines are in the z-direction for the velocity and position plots.

	55 DEGREES	INITIAL CONDITION	65 DEGREES
CAVITY CLOSURE TIME (PEAK) [s]	1.004	1.009	1.012

WATER EXIT TIME [s]	2.515	2.730	3.104
POP-UP HEIGHT [m]	1.542	1.369	0.657
MAXIMUM SUBMERSION [m]	-6.723	-7.297	-8.290
SAILING DISTANCE AT 6 s [m]	39.482	36.969	33.608
VELOCITY x_{Body} AT 6 s [m/s]	3.237	3.109	2.941
ACCELERATION PEAK MAGNITUDE [m/s^2]	18.511	21.678	26.194
MAX PRESSURE AFTER CAVITY CLOSURE [kN/m^2]	60.040	67.460	75.290

Table 7.3: Distinctive values for comparison for a change in water entry angle

The motion plot in Figure 7.2 shows that maximum submergence increases with increasing water entry angle. This is logical since the velocity is constant in the x_{body}- and z_{body}-direction, hence the body gets an increased initial velocity contribution in the vertical direction, in combination with small differences in angular acceleration. The maximum submergence is an important parameter, as discussed above and highly influenced by the water entry angle. Thus, the water entry angle is a crucial parameter. The smallest water entry angle gives the shortest submerged time and the highest body fixed velocity in x-direction at water exit. The contribution to counter clockwise rotation in the submerge phase seems to be independent of the three tested water entry angles. Hence, the case with the lowest water entry angle gives the highest water exit angle. Thus, an increase in pop-up height with decreasing water entry angle. The high exit velocity also leads to the longest sailing distance in global x-direction. The velocity is positive after 6 s for all the cases. It is most positive for the smallest water entry angle, as the decreasing rate is approximately equal for the three cases after second impact. The maximum pressure occurs just after the point of maximum submergence, where the hydrostatical pressure is at maximum. The case with water entry angle of 65° have the deepest maximum submergence point, and will also experience the highest pressure on the aft part.

a) b)

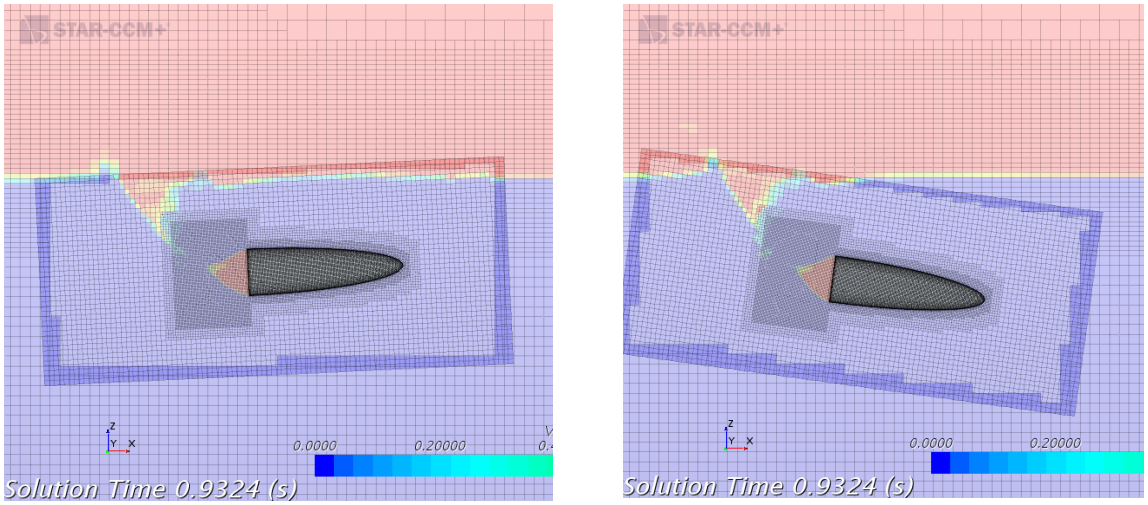

Figure 7.3: a) shows a picture of water entry angle 55° and b) shows a picture of water entry angle 65° at 0.9324s

The beginning of the air cavity closure can be seen from Figure 7.3, the time of the peak can be seen from Table 7.3. The VOF-pictures shows that case a) has started turning upwards, while case b) continues to decent.

7.3 COG

As earlier mentioned, the COG will be affected by the number of passengers and their seating arrangement. Three different values of COG in z-axis has been tested to see how the change in COG affects the behaviour of the free-falling lifeboat. The values are -0.3 m, -0.5 m and -0.7 m measure from the symmetrical centre line of the body.

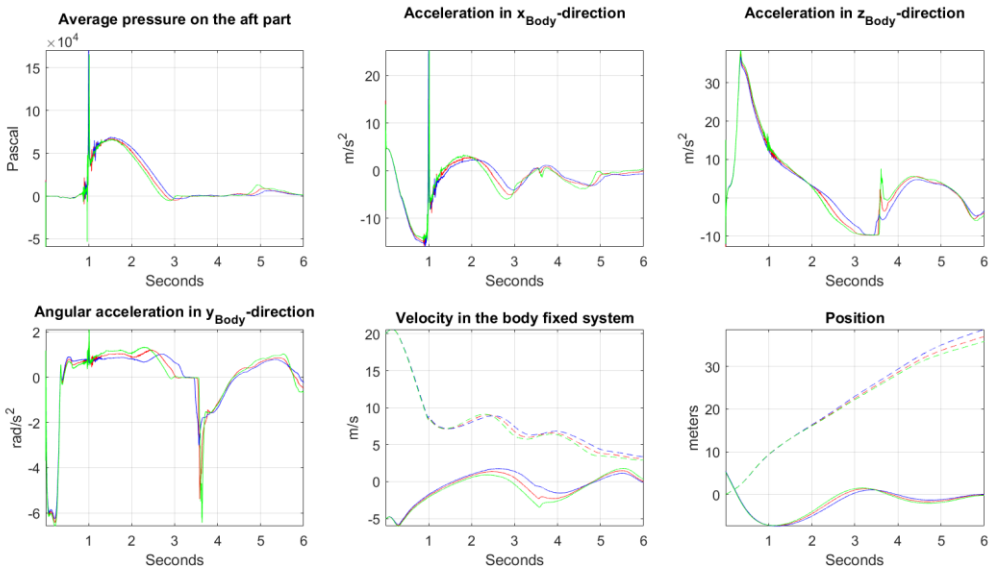

Figure 7.4: Result plots with different centre of gravity in z-direction, where blue is -0.3m, red is -0.5m and green is -0.7m. The accelerations and velocities are taken in the body fixed coordinate system. The dashed lines are in the x-direction, and the solid lines are in the z-direction for the velocity and position plots.

	-0.3 m	**INITIAL CONDITION**	**-0.7 m**
CAVITY CLOSURE TIME (PEAK) [s]	0.999	1.009	1.012
WATER EXIT TIME [s]	2.907	2.730	2.620
POP-UP HEIGHT [m]	1.083	1.369	1.516
MAXIMUM SUBMERSION [m]	-7.381	-7.297	-7.245
SAILING DISTANCE AT 6 s [m]	38.637	36.969	35.816
VELOCITY x_{Body} AT 6 s [m/s]	3.352	3.109	2.938
ACCELERATION x_{Body} PEAK MAGNITUDE [m/s^2]	25.306	21.678	25.297
MAX PRESSURE AFTER CAVITY CLOSURE [kN/m^2]	68.980	67.460	66.270

Table 7.4: Distinctive values for comparison of a change in centre of gravity in z-direction

The motion plot in Figure 7.4 reveals that the deepest maximum submergence, and the highest pressure after cavity closure, occur when the COG_Z is moved upwards. However, the difference is relatively small between the different cases. When the COG_Z is moved upward, the gravity-buoyancy arm becomes relative smaller. This result in a small counter clockwise rotation contribution in the water entry and in the submerged phase to the point where the body lies horizontal in the water. After this point, the gravity-buoyancy arm will contribute to a clockwise rotation. The behaviour is

the same when moving the COG_Z downward, but the arm is now longer, and contributes to a larger counter clockwise rotation before taking the horizontal position. This leads to the highest water exit angle, despite that the gravity-buoyancy arm counteract this rotation in the ascent. The water exit speed is approximately the same for all three cases, thus the most negative COG_Z gives the highest pop-up height. The water exit occurs last, and with the lowest water exit angle, for the case with the least negative COG_Z. This case gives the longest sailing distance as it has the largest water exit velocity.

7.4 Conclusion/ Discussion for the parameter investigation

The results shows that changing the maximum initial velocity with $\pm$ 5 m/s has the largest effects on the behaviour of the body. It manifests as the highest and lowest values in the air cavity closure time, pop-up height, acceleration peak magnitude, horizontal sailing distance and velocity at 6 s. It also manifests as the least maximum submergence and earliest water exit time for the lowest and highest initial velocity, respectively. By changing the water entry angle with $\pm 5°$, it shows great effect in the maximum average aft pressure, as it also has the largest maximum submergence. The highest and lowest values in maximum submergence is found for the highest and lowest water entry angle, respectfully. The latest water exit time and deepest submergence is also found for the highest water entry angle. The rearrangement of the COG with $\pm$ 0.2 m in z_{body} gave smallest effects, the only significant difference was the angular accelerations and the pop-up height difference.

8 Finite Element Method

In DNVGL-ST-E406 section 6.1.7 it is stated that “The ultimate strength capacity at material level (metal yield, FRP rupture, core fracture) and at structural level (buckling, collapse) shall be assessed for all structural elements based on a rational and justifiable engineering approach. FEM can be used for this purpose.” (DNV-GL, 2016) This gives a good indication that FEM models of a free-falling lifeboat can be used for analysing the structural behaviour in a lifeboat dive. The next sections accounts for the structural response to the initial conditions used in the CFD simulations.

8.1 FEM introduction

The Finite Element Method (FEM) is a method for computing displacements, stresses and strains in a structure. It uses numerical solutions of the equations that is govern in the problems found in nature. These equations can be expressed as in differential or integral form. Therefore, FEM is known as a numerical technique for solving these partial differentials or integrals in the nature. A finite element can be visualized as a small portion of a continuum, in this thesis a structure. The mesh in FEM is therefore a “set” of finite elements, where i.e. the displacements in a structure is expressed within each element by means of a polynomial expansion. (Oñate, 2009)

When modelling larger structures, in 2D or 3D, with different material properties, the partial differentials or integrals in the nature becomes more complex and time consuming. Here the aid of FEM programs is a valuable tool. In most of the programs the user can select a variety of element types, this involves Timoshenko and Euler-Bernoulli beam theory and plate theories from Reissner-Mindlin and Kirchhoff. Since the FEM program creates the elements, with suitable number of nodes and degrees of freedom specified by the user, it is necessary to know if the selected elements can converge to exact (mathematical) results in problems, as the mesh is refined towards infinity. In this case the patch test can be used, which is a numerical test that is carried out on a “patch” of elements loaded by a consistent load vector which gives a state of constant stress within the patch. A stable element that passes the patch test is able to display a) a rigid body motion without strain, b) states of constant strain and c) compatibility with adjacent elements when a state of constant strain prevails in adjacent elements. Meeting these requirements is sufficient to guarantee that the mesh of these elements will converge to exact (mathematical) results in problems other than a patch test as the mesh is refined towards infinity. (Mathisen, 2016)

8.2 Abaqus

For FEM program in the thesis Abaqus version 6.14-1 has been used. In Abaqus the partial differentials or integrals are solved by the use of principle of virtual work, and the definition of it is seen in equation [38].

$$\int_V \boldsymbol{\sigma} : \delta \boldsymbol{D} \, dV = \int_S \boldsymbol{t}^T * \delta \boldsymbol{v} \, dS + \int_V \boldsymbol{f}^T * \delta \boldsymbol{v} \, dV \qquad [38]$$

Equation [38] is one of many basic finite element equations to obtain the end results in Abaqus, see the Abaqus Theory Guide section 2.1 for the complete formulation. (Simulia - Abaqus 6.14, 2016) The principle of virtual work is described as “A structure is in equilibrium under a set of external loads if after imposing to the structure arbitrary (virtual) displacements compatible with the boundary conditions, the work performed by the external loads on the virtual displacements equals the work performed by the actual stresses on the strains induced by the virtual displacements.” (Oñate, 2009)

There have been conducted a convergence and eigenmode check for the FEM model before the structure were implemented into a fluid-structure-interaction.

8.2.1 Modelling

The modelling process was done in a combination of AutoDesk Inventor and Abaqus, where Inventor created the overall geometry and in Abaqus each part would be assigned correct properties with respect to shell, beams and material. DNVGL-ST-E406 section 6.1.5.4 Figure 6-1 shows an example of longitudinal stiffeners placement, which is applied to the simplified geometry in the same manner. Section 6.1.5.5 states also that a system of continuous transverse frames shall be fitted, therefor ring stiffeners with a distance of Δx_{Stiff} = 1.5m were also applied to the body, as seen in Figure 8.1.

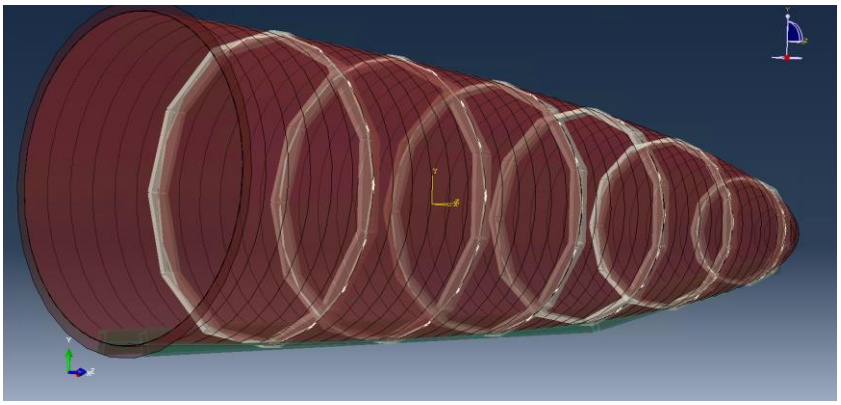

Figure 8.1: Abaqus model of the geometry, shell (hull and aft) labelled as red, ring stiffeners as white and bottom stiffeners as green

Shells and beams were merged after the mesh operation to ensure that the nodes had correct DOF's.

In DNVGL-ST-E406 steel and aluminium is tested, and with comparison of the work by Andrea Califano & Brinchmann (2013), the material selected is steel, with technical specifications described in Table 8.1. (Califano & Brinchmann, 2013)

DENSITY	$\boldsymbol{\rho_s}$	7850 $[\boldsymbol{kg/m^3}]$
POISSON RATIO	ν	0.3
E-MODULE	E	209 [GPa]
YIELD STRESS	σ_y	235 [MPa]
ULTIMATE STRENGTH	σ_u	400 [MPa]

Table 8.1: Technical specifications for material selection

It is assumed for the simulations that the material only has elastic behaviour with no plastic properties. This was done because Abaqus requires a detailed list from a Strain-Stress curve for the material in the plastic zone, and that the solving time for Abaqus is reduced with only elastic properties. The yield stress and ultimate strength will be used as the upper limits of stresses the model can excite.

8.2.2 Beam element

The ring stiffeners was applied with a rectangular beam profile, HxW = 50x100 [mm], while the bottom stiffeners with a box beam profile with a thickness of 20mm and HxW = 200x100 [mm]. The bottom stiffeners were placed 11.25° from the midline of the body, which results in 22.5° spacing between them. The bottom stiffeners were also oriented such that they face towards the midline in the body, [x, y, z] = [0,$\pm 0.196349541, -1$]. Because of the orientation of the longitudinal stiffeners their length does not cover the full length of the lifeboat, this is due to an overlap between them.

The beam elements were modelled as generalized profiles in Abaqus, due to the necessity of translating the centre of the profile inside the lifeboat hull. This means the moments of inertia was calculated by the following equations.

$$I_{11} = \int_A (x_2 - x_2^c)^2 dA \quad [39]$$

$$I_{22} = \int_A (x_1 - x_1^c)^2 dA \quad [40]$$

$$I_{12} = \int_A (x_1 - x_1^c)(x_2 - x_2^c) dA \quad [41]$$

$$J = \beta h b^3 \text{ (Bell, 2011)} \quad [42]$$

Where (x_1, x_2) is the position of the point in the local (1,2) beam section axis system and (x_1^c, x_2^c) is the position of the centroid of the cross-sectional area. (Simulia - Abaqus 6.14, 2014) β is a constant depending on h/b, where h is the length of the long side and b is the length of the short side.

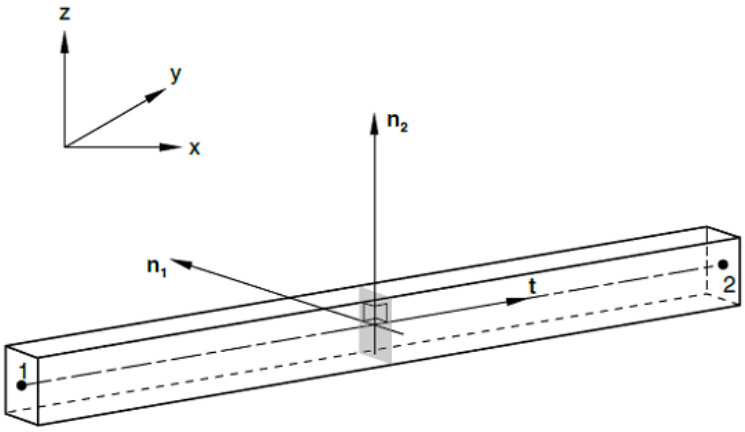

Figure 29.3.4–1 Local axis definition for beam-type elements.

Figure 8.2: Example of local axis definition for beam-type elements (Simulia - Abaqus 6.14, 2014)

From equations [39] - [42] the properties of the two types of beam elements became as seen in Table 8.2.

	BOTTOM STIFFENER [LONGITUDINAL]	**RING STIFFENER [TRANSVERSE]**
AREA $[m^2]$	0.0104	0.005
I_{11} $[m^4]$	$1.501867*10^{-4}$	$4.1667*10^{-6}$
I_{22} $[m^4]$	$1.37867*10^{-5}$	$4.1667*10^{-6}$
I_{12} $[m^4]$	0	0
TORSIONAL CONSTANT $[m^4]$	$5.3334*10^{-5}$	$2.8625*10^{-6}$

Table 8.2: Beam section properties

The beam elements are modelled as a Timoshenko beam in space with linear interpolation, which is element type B31 in Abaqus. Which Abaqus has done a patch test for and it is stated: “All elements yield exact solution except the cubic beams, which differ from the analytical solution by about 2% for the NLGEOM step and the subsequent perturbation step. The elements are recommended only for linear analysis. “ (Simulia, 2014)

At a given stage in the deformation history of the beam, the position of a material point in the cross-section is given by the expression

$$\hat{x}(S, S^{\alpha}) = x(S) + f(S)S^{\alpha}n_{\alpha}(S) + w(S)\,\psi(S^{\alpha})t(S)$$

Where x(S) is the position of a point on the centreline, $n_\alpha(S)$ are unit orthogonal direction vectors in the plane of a beam section, t(S) is the unit vector orthogonal to n_1 and n_2, $\psi(S^\alpha)$ is the warping function of the section, w(S) is warping amplitude, and f(S) is a cross-sectional scaling factor depending on the stretch of the beam.

8.2.3 Shell element

Shell elements were assigned to the surface of the simplified geometry. The choice of this element type is due to the same behaviour as for a plate, and allows the modelling of curved, intersecting shells that can exhibit nonlinear material response and undergo large overall motions (translations and rotations). Three different shell thicknesses have been assigned to the lifeboat, 20 mm, 10 mm, 5 mm and 2.5 mm which is equal for the whole body.

The shell is modelled as a conventional stress/displacement shell with 4 nodes, element type S3. Which Abaqus has done a patch test for and states: “All elements yield exact solutions except S8R. S8R will pass the test if the element shapes are rhombic, but they fail the test for general quadrilaterals.” (Simulia, 2014)

8.3 System properties

The difference between the Star-CCM+ model and the Abaqus model should not differ too much, with respect to mass, moments of inertia and centre of gravity. For this reason, point masses, non-structural masses and moments has been applied to the FEM model to ensure the same model properties. It would be preferable to distribute some of the mass directly inside of the model to create the illusion of an engine and passengers, but the mass and moments must be connected to a node (for point masses and moments) and elements (for non-structural masses) in the FEM model. Which means all the weight added to the model has been applied to the hull and aft, since it is hollow.

	STAR-CCM+	ABAQUS	Δ	DIMENSIONS
MASS	23561.94	23561.94	0	kg

I_{xx}	21205.8	37136.17	15930.37	kg*m^2
I_{yy}	150501.9	150501.9	0	kg*m^2
I_{zz}	150501.9	150501.9	0	kg*m^2
$COG_{x_{body}}$	3.7500	3.75180	0.0018	m
$COG_{y_{body}}$	0	-5.923*10^{-3}	5.923*10^{-3}	m
$COG_{z_{body}}$	-0.50000	-0.50017	0.00017	m

Table 8.3: Star-CCM+ and Abaqus model properties

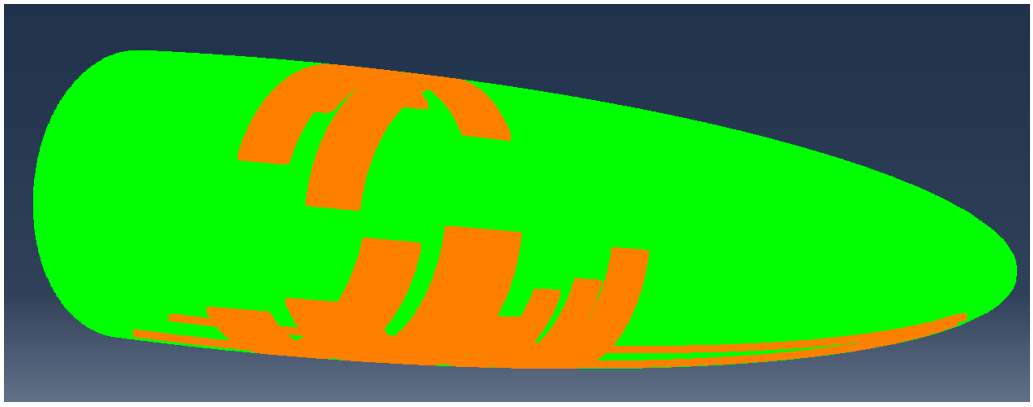

Figure 8.3: Distribution of the mass and moments to ensure same properties in both programs, where green is the point masses and moments applied and orange is the non-structural mass

As seen in Table 8.3 the difference between the two programs is of minor order. Where the main difference lies in moment of inertia about the x_{body} – axis, with a difference of 15930.37 kg*m^3. Since the body is symmetric in the CFD simulations, this is assumed to be of negligible effects. The reason for the large difference is due to the point masses and non-structural mass, as seen in Figure 8.3. They will have a large contribution in the rotation about the x_{body} – axis since they are not located on the axis.

It should be noted that the change in shell thickness affects all the properties, but it is only the centre of gravity that will differ from Table 8.3, and this will differ by mm's, which is neglectable. The moments of inertias have been distributed such that it is equal for all thicknesses, and the mass on the aft plate is of minor differences.

8.3.1 Coordinate systems used

Since the lifeboat has an initial water entry angle of 60 degrees, the structural model is also needed the same incline. Such that it stands 5.613 m in the z-direction with its midline, with respect to the origin at mean water surface, [0, 0, 0]. Because of this, two coordinate systems in Abaqus has been used, as seen in Figure 8.4.

a) b)

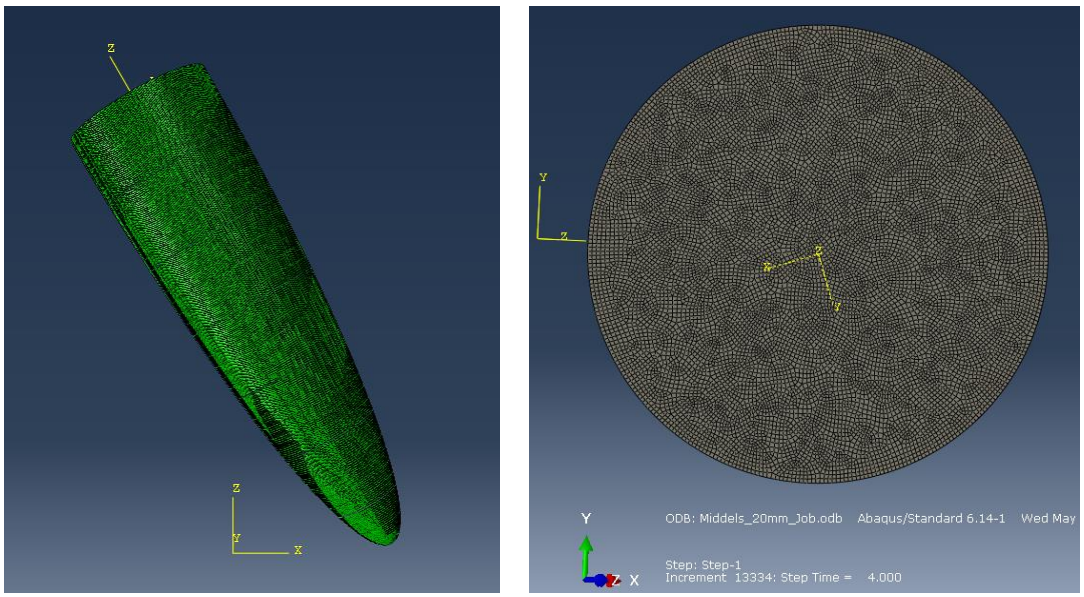

Figure 8.4: Coordinate systems in Abaqus, where a) is the origin and b) is located on the aft

Figure 8.4 shows the two different coordinate systems used in Abaqus. Figure 8.4 a) shows the origin located at [0, 0, 0], while Figure 8.4 b) shows the coordinate system located at the mid-point of the aft plate. Figure 8.4 b) is connected with three nodes, these nodes are 889, 16 253 and 7 129, which is located on the outer diameter of the aft. The coordinate system in [0, 0, 0] will be referred to n_{origin} and the coordinate system following the three nodes n_{nodes}, where n = x, y or z.

8.4 FEM convergence study

In order to get accurate results of the FEM-model, with as low CPU cost as possible, a convergence study was conducted with three different mesh sizes for the shell thickness of 20 mm. This was done with the pressure exported from the Star-CCM+ simulation, with air modelled as incompressible, combined with a Butterworth lowpass filter to get unnecessary disturbances cleared, as seen in

Figure 8.6. The cut-off frequency was set to 20 Hz, it should be noted that the filter used was distributed in the course “TMR 7 Experimental methods in Marine Hydrodynamics”. The reason for the frequency filter was because of the eigenmodes is not known, such that these would not affect the convergence results.

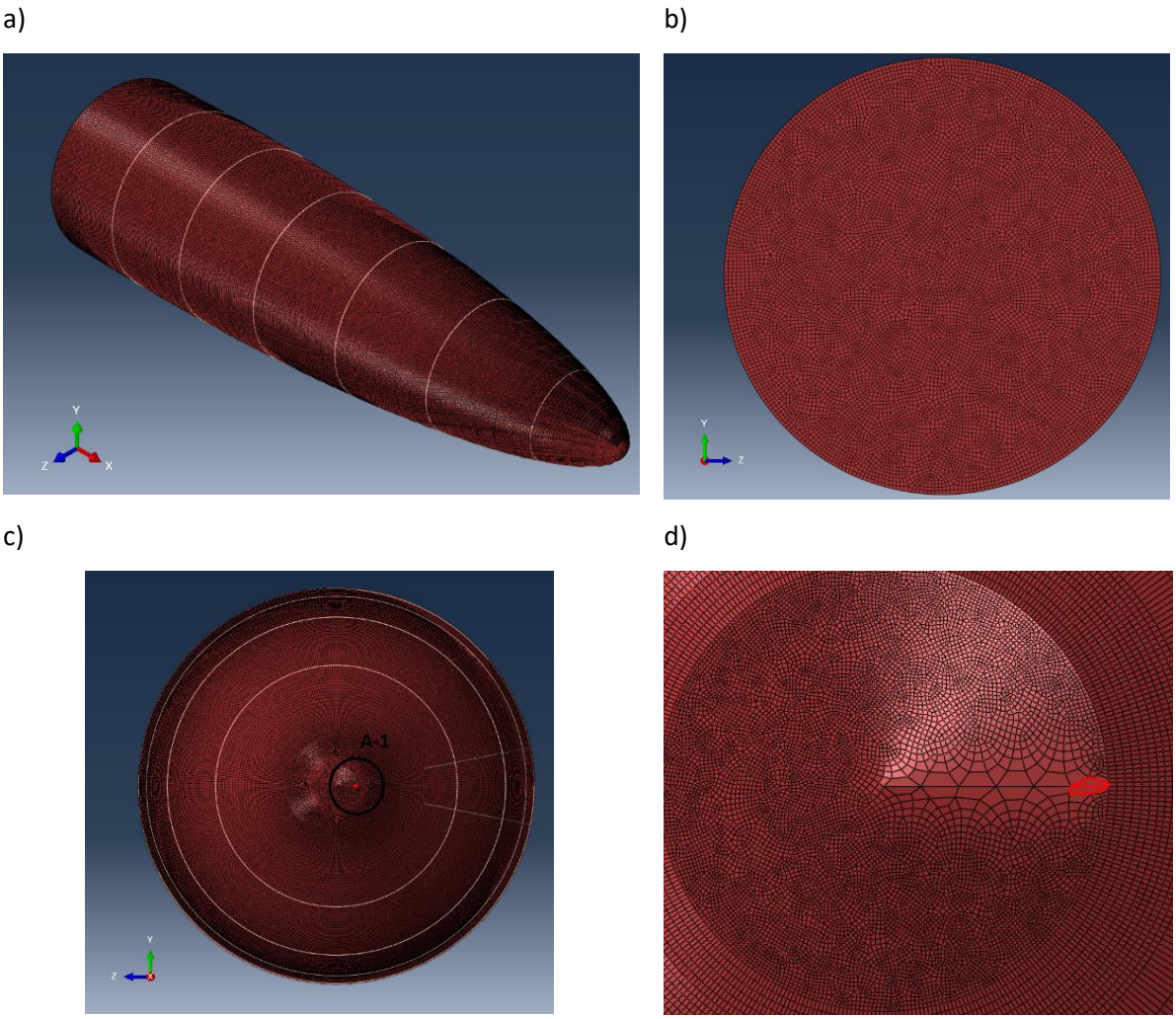

Figure 8.5: Mesh discretization $\Delta x_{2_{FEM}}$, where a) is of hull, b) only of the aft, c) the location of two poor elements in the fore part of the hull and d) zoomed in on the poor elements (A-1 from c))

The different FEM mesh types will be referred to as $\Delta x_{i_{FEM}}$, where i = 1, 2 or 3, to distinguish between the CFD mesh and FEM mesh. In Figure 8.5 a) and b) $\Delta x_{2_{FEM}}$ gives an image of how the mesh has been developed. Where Figure 8.5 c) and d) shows the two cells with poor quality, element number 80 751 and 89 632. These two elements are referred to as poor quality elements since the isoparametric angles are out of the suggested limits. Since it is only two elements and not a major error, because it is a suggested limit, their warning is not accounted for in the rest of the thesis.

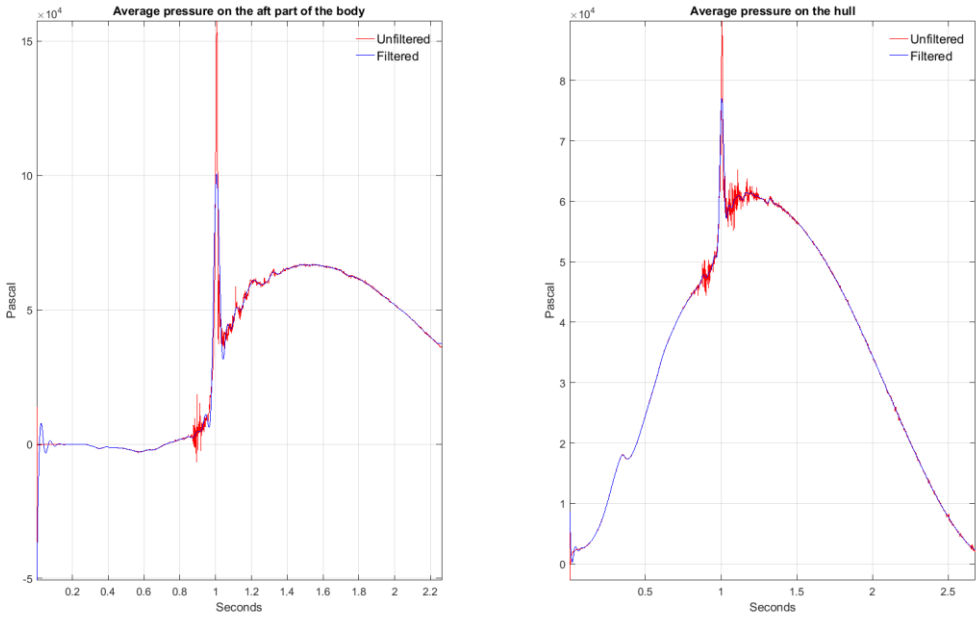

Figure 8.6: Pressure plots from CFD Δx_2, where red is unfiltered and blue is filtered

The pressure was evenly distributed over the aft part, such that a mapping method was not used. This goes under the assumption from 6.4 that most of the pressure in the submerged phase can be seen as evenly distributed for large periods of time for the aft part. To simplify the convergence check for the hull, the pressure on this part was also evenly distributed. For the convergence of the aft, all the nodes on the hull were applied boundary conditions with no translation or rotations in x, y and z. For the convergence check of the hull, boundary conditions at all the nodes on the aft where applied in the same manner as for the convergence of the aft, which means no translation or rotation in x, y and z.

	# ELEMENTS $\Delta x_{3_{FEM}}$	**# ELEMENTS $\Delta x_{2_{FEM}}$**	**# ELEMENTS $\Delta x_{1_{FEM}}$**
AFT PART	1 021	12 320	32 994
HULL	17 302	100 626	276 702

Table 8.4: Elements in each type of mesh

	DISPLACEMENT	
	AFT	**HULL**
$\Delta x_{3_{FEM}}$	5.23225e-7	5.11577e-5
$\Delta x_{2_{FEM}}$	5.24239e-7	5.1124e-5

$\Delta x_{1_{FEM}}$	5.24209e-7	5.10866e-5

Table 8.5: Displacement from mesh types

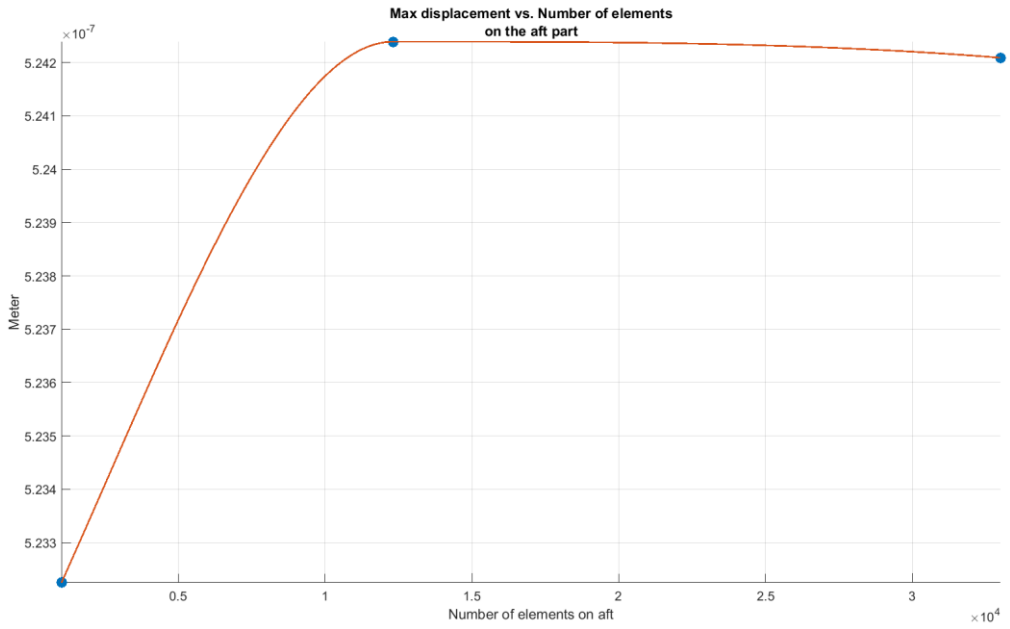

Figure 8.7: Max displacement versus number of elements on the aft with the applied pressure from Figure 8.6, blue dots are the results

As seen from Table 8.5 the values do not differ much from each other, and that the displacement is quite low. The reason for the low displacement is because the convergence was done for a shell thickness of 20 mm, which is the thickest shell in this thesis. From Table 8.5 and Figure 8.7 it is possible to see that the $\Delta x_{1_{FEM}}$ and $\Delta x_{2_{FEM}}$ has only a difference of $3*10^{-11}$ m, where $\Delta x_{2_{FEM}}$ overpredicts the value slightly. Figure 8.7 gives the indication of that $\Delta x_{2_{FEM}}$ would be of sufficient accuracy to predict the displacements for the aft.

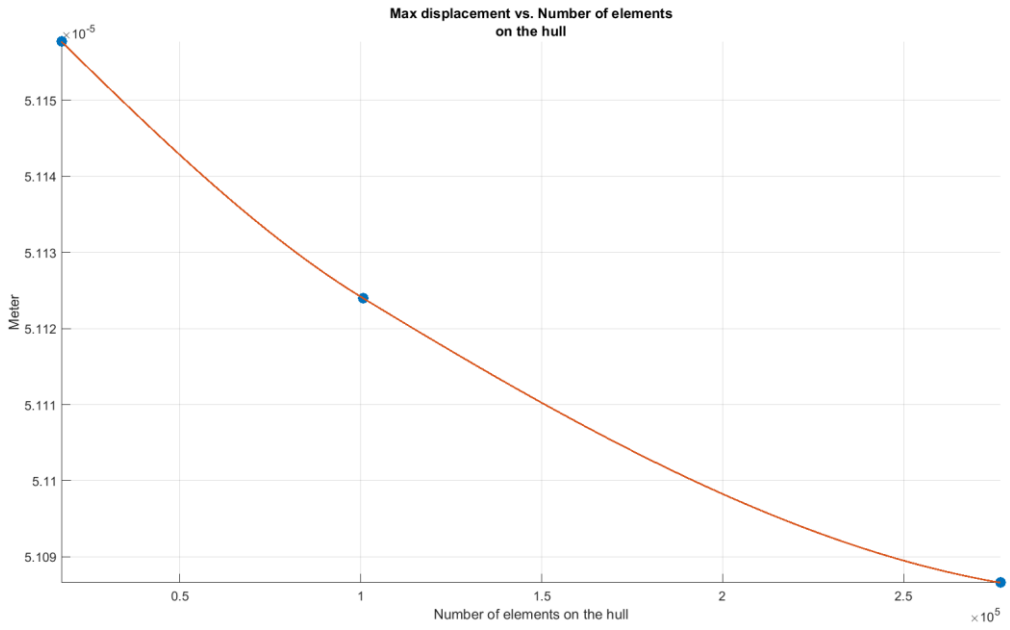

Figure 8.8: Max displacement on the hull versus number of elements on the hull with the applied pressure from Figure 8.6, blue dots are the results

As seen in Figure 8.8 the results have not converged properly, but a limitation of the geometry is that the elements at the front and aft will be too distorted with a higher number of elements than $\Delta x_{1_{FEM}}$. For this reason, it would be a reasonable choice to use the $\Delta x_{1_{FEM}}$ mesh, but since $\Delta x_{1_{FEM}}$ and $\Delta x_{2_{FEM}}$ differ by only 3.74*10^{-8} m, and most of the load cases will affect the aft, $\Delta x_{2_{FEM}}$ would give sufficient results.

8.5 Eigenmodes of the structure

As seen in the results from section 6 the accelerations and pressure has disturbances. These disturbances, or oscillations when the air is modelled as compressible, can be in the same period as the natural frequencies of the lifeboat. Also, the loads from the air cavity closure will affect the structures response, both with air as incompressible and with compressible. Therefore, the eigenmodes of the structure should be known. The eigenmodes is calculated in Abaqus with the use of a linear perturbation analysis with frequencies, which uses the Rayleigh-Ritz method for the calculations. From section 8.4 it was found that $\Delta x_{2_{FEM}}$ would give sufficient results, which is the mesh the eigenmodes has been found from.

The eigenvalue problem for the natural frequencies of an undamped finite element model is found in

$$(-\omega^2 M^{MN} + K^{MN})\phi^N = 0 \quad [43]$$

Where $\mathbf{M}^{MN}$ is the mass matrix (which is symmetric and positive definite), $\mathbf{K}^{MN}$ is the stiffness matrix (which includes initial stiffness effects if the base state included the effects of nonlinear geometry), $\boldsymbol{\phi}^N$ is the eigenvector (the mode of vibration) and M and N are degrees of freedom (DOF). (Simulia - Abaqus 6.14, 2014)

PLATETHICKNESS		**1**	**2**	**3**	**4**	**5**
20 MM	Frequency [Hz]	13.278	19.173	21.430	25.296	26.361
	Period [s]	0.075	0.052	0.047	0.0395	0.038
10 MM	Frequency [Hz]	1.946	2.572	2.683	3.245	3.284
	Period [s]	0.514	0.389	0.373	0.308	0.304
5 MM	Frequency [Hz]	0.907	1.192	1.284	1.514	1.548
	Period [s]	1.102	0.839	0.779	0.660	0.646
2.5 MM	Frequency [Hz]	0.397	0.517	0.583	0.660	0.687
	Period [s]	2.516	1.933	1.716	1.514	1.455

Table 8.6: Eigenfrequencies and eigenperiods for the aft plate with corresponding modes

a) b) c)

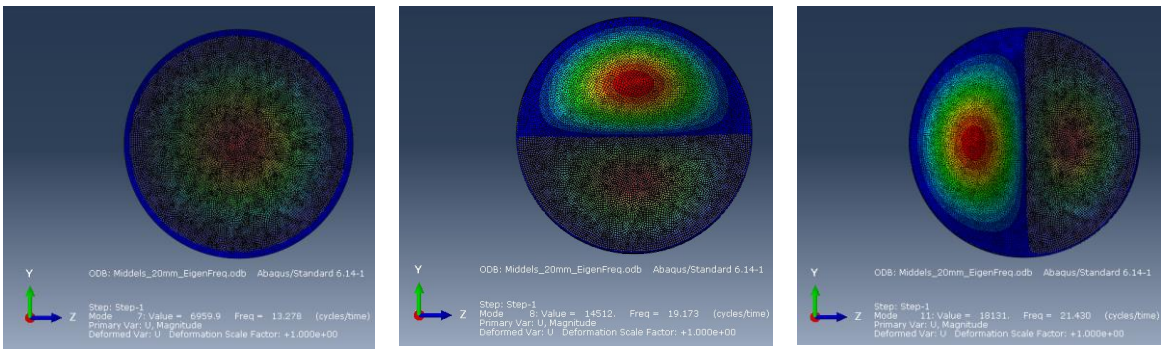

d)

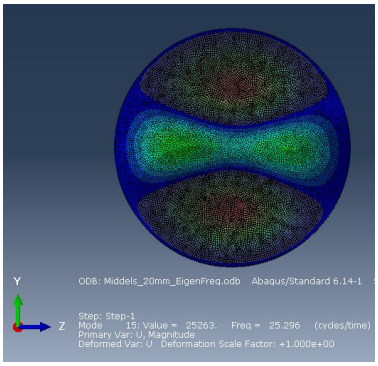

e)

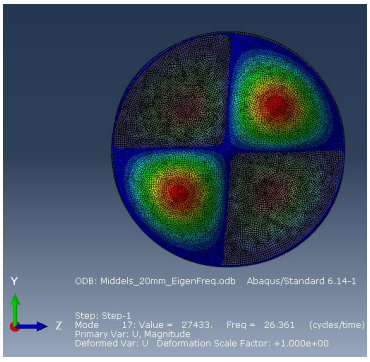

Figure 8.9: Visualization of the 20 mm eigenmodes listed in Table 8.6, the behaviour is equal for all thicknesses, where a) is connected to eigenmode **1**, b) is connected to **2**, c) is connected to **3**, d) is connected to **4** and e) is connected to **5**

As seen in Table 8.6 and Figure 8.9 this are only the eigenmodes connected to the aft part of the body, this is because of the aft part do not have any stiffeners which will affect the bending motions. The eigenmodes connected to the hull of the structure has not been conducted.

From Table 8.6 it is seen that the frequency changes with the difference in thickness, which indicates that the plate is stiffness-dominated. This is because the weight is approximately the same for the aft part, as mentioned in 8.3. As seen in section 6 the eigenperiods is out of reach for the disturbances obtained in the pressure in Figure 6.7**,** where the period of most of the disturbances right after the air cavity closure lies in the area of 0.001 s – 0.01 s for the average pressure, 0.005 s – 0.018 s for the maximum pressure and 0.001 s – 0.003 s for the minimum pressure. This shows that the disturbances from CFD will have low influences on the structure.

9 Fluid-Structure-Interaction

In Andrea Califano & Brinchmann (2013) it was used a weak coupling between the CFD and FEA program, the results presented in sections 10 - 13 are obtained with two different strong couplings. The main difference of a weak and strong coupling is the time step, whereas the weak coupling requires one solution of each problem during a time step and no iterations are performed between the two programs time steps, while for the strong coupling the programs has the same time step and the two programs exchange data between them before one time step is complete. For the strong coupling a co-simulation has been performed, this means that Star-CCM+ uses a built-in function to run both programs, whereas one program “sleeps” when the other is running. Here the time step is equal and an exchange rate of data between the two programs has been established. This method will be described further as a Fluid-Structure-Interaction (FSI) problem.

9.1 Communication between CFD and FEM

In a FSI problem the two programs interact with each other to create a mapping field of various inputs, such as acceleration, pressure, deformations etc. Here it can be established a one-way interaction or a two-way interaction. This is the strong coupling method, whereas a one-way interaction means that Star-CCM+ will give input to Abaqus, where Abaqus uses this input to calculate the displacements, stresses etc. Two-way interaction means that Star-CCM+ gives the forces to Abaqus and Abaqus returns the displacements back to Star-CCM+. In both cases it can be decided if Star-CCM+ should give the inputs from its boundaries to the surface in Abaqus (surface-to-surface coupling) or between Star-CCM+ boundaries and Abaqus nodes (surface-to-point coupling), the coupling in this thesis is done with a surface-to-surface coupling.

9.1.1 FSI interaction between Star-CCM+ and Abaqus

The inputs exported/imported from Star-CCM+ or Abaqus is referred to as mapping. The data mapper uses various interpolation schemes to transfer source data to target meshes, in the FSI problem with one-way interaction it would be Star-CCM+ which obtains the source data and the target mesh is the Abaqus FEM model. There are mainly five different methods Star-CCM+ offers to

map the data, in all coupling methods used in the thesis, the option Least Squares method has been applied.

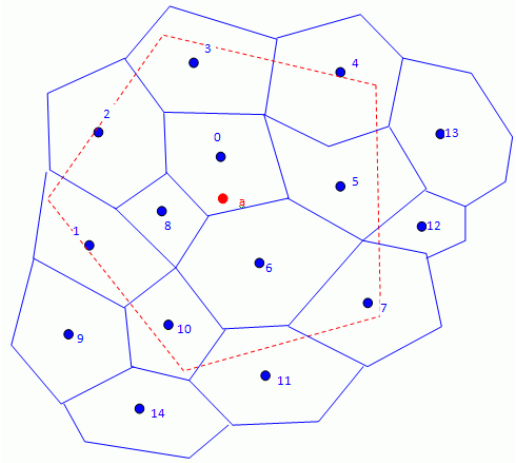

Figure 9.1: Mapping interpolation option Least Squares method

The Least Squares method, Figure 9.1, consider mapping data from faces of the blue background mesh to faces of the red mesh using a least squares scheme. In this case the Face 0 (blue) is the closest source to the target Face a (red). For this method, all neighbours of Face 0 are defined as any face that shares at least one vertex with Face 0. Such that in Figure 9.1 the neighbours included as a part of the interpolation stencil are faces 0, 2, 3, 4, 5, 6 and 8. The drawback of this method is that some of the blue faces (for example 1, 7, 10, and 11) that the target imprint upon are not included in the stencil. On the other hand, the advantage of this method is that it is applicable for all element types and for source and vertex source stencils. (Steve CD adapco, 2016)

For the FSI problem to be successful, a new time scheme between the two programs is also needed, the two options are;

- Abaqus Explicit Coupling: to exchange data at a specific coupling time-step
- Abaqus Implicit Coupling: to exchange data more than once per time-step

The difference between the two time schemes are that the explicit coupling is for cases where the effect of the structure on the fluid is much larger than the effect of the fluid on the structure. Whereas the implicit coupling allows the simulations to exchange data more than once per-time step. For all cases in this thesis an implicit coupling has been used, this is because it is expected to occur hydroelastic effects.

9.2 Criterions and assumptions

Since the geometry is simplified and the material is only modelled with elastic effects, some assumptions and criterions has been established for the structure, with respect to FEM solving method, hydroelastic effects, boundary conditions and material, and when the air is modelled as compressible in the CFD simulation.

9.2.1 FEM solving method

The load cases in the FEM model has been established with a dynamic implicit quasi-static approach, which means the inertia term in the dynamic equation [44] will have small contribution due to the acceleration values are taken as low in the solving method. The equations for this solving method has not been distributed to the author, such that the exact behaviour of the solving method is unknown.

[44]

$$\underbrace{M\ddot{y}(t)}_{Inertia} + \overbrace{C\dot{y}(t)}^{Damping} + \underbrace{Ky(t)}_{Stiffness} = F(t)$$

Where M is the mass, C is the damping, K is the stiffness and $\ddot{y}, \dot{y}$ and y is acceleration, velocity and position, respectively. The main difference between a static analysis and dynamic analysis is that a dynamic load can have larger effect than a static load of the same magnitude due to the structure's inability to respond quickly to the loading (by deflection). When using a quasi-static approach, a dynamic amplification factor (DAF) is often used to account for the dynamic effects. The factor can be calculated by equation [45]. (Larsen, 2016) (Faltinsen, 2005)

[45]

$$DAF = \frac{y_{maks}}{y_{statisk}} = \frac{|y_p|}{|y_{st}|}$$

The DAF has not been accounted for any of the load cases for the structure. Which means that the response of the structure in the results will be of smaller magnitude than with a dynamic solver. On

the other hand, the large pressure peak from the air cavity will be larger when modelling the air as incompressible. This unrealistic large peak can account for any loss of dynamic effects.

The contribution from the inertia term from the solving method can be checked with the use of the energy balance equation

$$E_U + E_{\mathrm{K}} + E_F - E_W - E_{QB} = constant \quad [46]$$

Where E_U is the internal energy, E_K is the kinetic energy, E_F is the energy by contact friction between the contact surfaces, E_W is the work done by external forces and E_{QB} is energy by the damping effect of solid medium infinite elements. (Simulia - Abaqus 6.14, 2016) If the kinetic energy is small compared with the energy from external forces it can be assumed that the FEM model has been solved with a quasi-static approach.

9.2.2 Response and hydroelastic effects

Hydroelasticity means that the fluid flow and the structural elastic reaction are considered simultaneously and that they have mutual interaction, that is;

- The elastic vibrations cause a fluid flow with a pressure field
- The hydrodynamic loading affects the structural elastic vibrations

A slamming load is an example of impulsive loads in which the force has a limited duration, T_d. The character of response is dependent on the ratio T_d/T_n, where T_n is the natural period. For short duration loads, $T_d/T_n <\approx 0.25$, the force impulse can be written as

$$I = \int_0^{T_d} f(t)dt \quad [47]$$

determines the maximum response. By assuming the maximum response occurs on the time scale of T_n, the integral can be approximated as

[48]

$$y_p(t) = \frac{1}{m\omega_n}\sin(\omega_n t)\exp(-\xi\omega_{n0}t)\int_0^{T_d} f(\tau)d\tau$$

This shows that the maximum response is proportional to the force impulse as a function of time. Where m is the mass, ω_n the natural frequency, ξ the damping ratio, ω_{n0} the undamped natural frequency and the integral is the force integrated over time. The damping ratio can be found from

[49]

$$\xi = \frac{b}{b_{cr}}$$

Where b is the damping, found from equation [50], and b_{cr} is the critical damping, found from equation [51]. (Faltinsen, 2005)

[50]

$$b = \sqrt{mc}\ln\left(\frac{y_i}{y_{i+n}}\right)/\pi n$$

Where c is the stiffness, y_i and y_{i+n} is the response and n is an integer.

[51]

$$b_{cr} = 2\sqrt{mc}$$

If the ratio $\frac{T_d}{Tn}$ is smaller than 1 the load operates in such a low duration that the structure does not have time to react, and the response becomes low. If the ratio is over 1 the response of the structure is large, since the load excites in the eigenperiode of the structure. The tendency is that the longer the rise time of the loading to its maximum value, the lower DAF is. (Faltinsen, 2005)

To check if hydroelastic effects can occur, Figure 9.2 can be used. It shows the structural response as a function of a parameter that is proportional to the wetting time of a rigid wedge and natural period, based on beam theory. By assuming that the load duration from the air cavity closure is taken as the wetting time, due to the water jet impact from the air cavity closure, Figure 9.2 can give an indication if hydroelastic effects occurs.

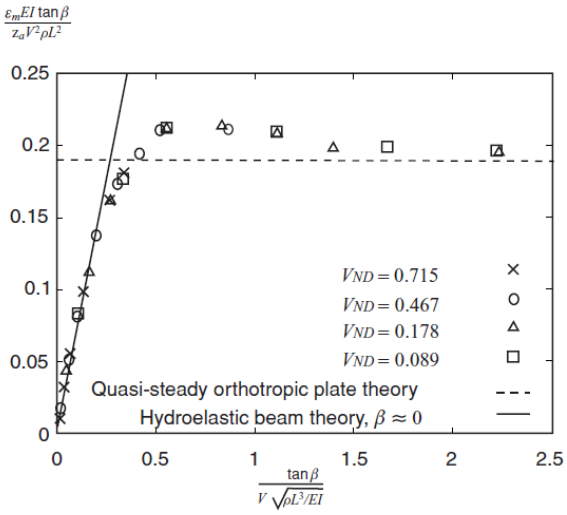

Figure 8.20. Nondimensional maximum strain ε_m in the middle of the second longitudinal stiffener from the keel. The strain is presented as a function of a parameter that is proportional to the ratio between wetting time of a rigid wedge and natural period of the longitudinal stiffener based on beam theory. Different nondimensional constant impact velocities V_{ND} (see eq. (8.32)) are given. β = deadrise angle. Calculations by hydroelastic orthotropic plate theory (Faltinsen 1999) are shown.

Figure 9.2: The response in the structure as a proportional to the ratio of T_d over T_n (Faltinsen, 2005)

9.2.3 Boundary conditions

Boundary conditions has been applied to the FEM model for the surface that is not solved for, which means to input files for the FEM model. One input file where only the hull has boundary conditions and one input file where only the aft has boundary conditions applied. The boundary conditions applied is no translation or rotations for the body in x, y and z.

As DNVGL-ST-E406 section B.3.10 states that the boundary conditions should be located away from areas of interest, as the loads transferred from the hydrodynamic load analysis may otherwise lead to imbalance in the model.

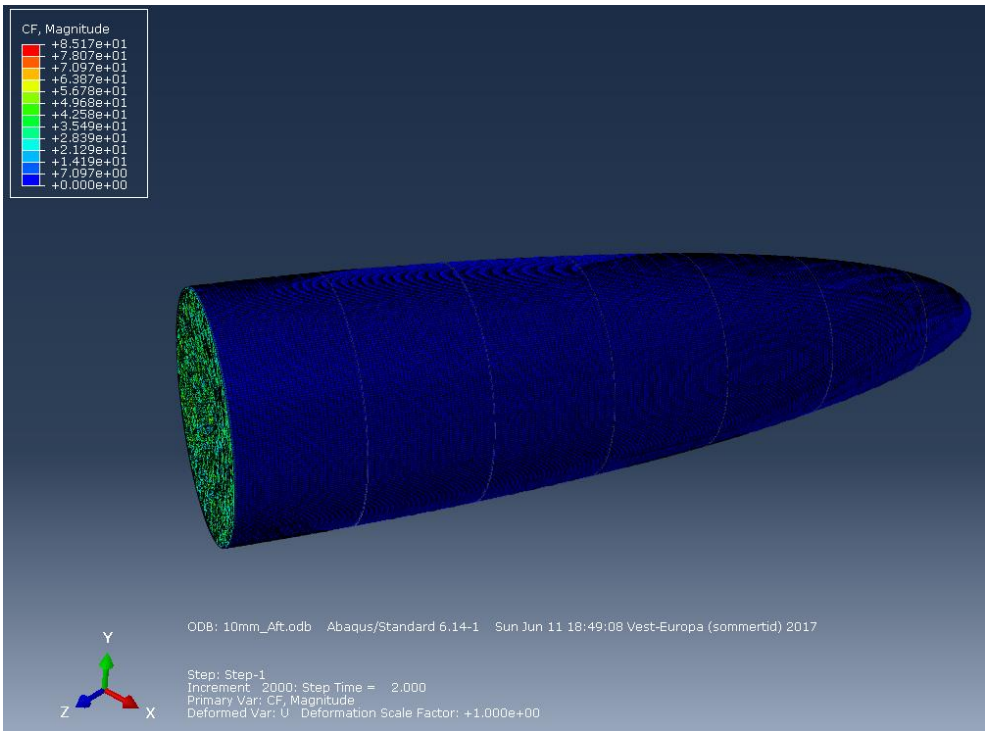

Figure 9.3: Concentrated forces (CF) from Star-CCM+ to Abaqus

As seen from Figure 9.3, where the area of interest is the aft, the hull does not experience any forces acting on it. From this it is assumed that the boundary conditions applied to the structure is accurate.

9.2.4 Von-Mises and Tresca

For metals, it is normal to use one of the yield criteria in which yielding can be identified as having occurred once a certain combination of the principal stress reaches the yield stress. Since the results is obtained under the assumption that the material is only elastic, the von-Mises criteria and the Tresca criteria will be used to check for yielding. The difference between the two can be seen in Figure 9.4.

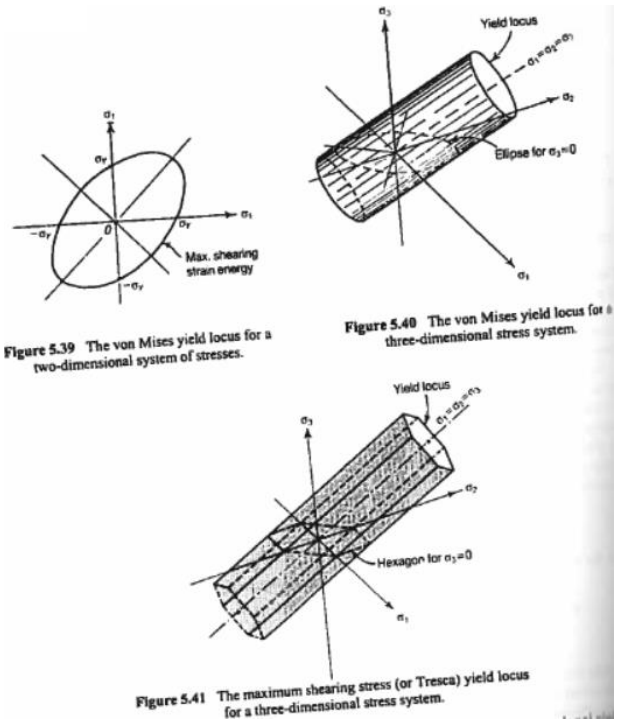

Figure 5.39 The von Mises yield locus for a two-dimensional system of stresses.

Figure 5.40 The von Mises yield locus for a three-dimensional stress system.

Figure 5.41 The maximum shearing stress (or Tresca) yield locus for a three-dimensional stress system.

Figure 9.4: Von Mises and Tresca criterion (Case, et al., 1999)

Both of the two criteria can be calculated directly in Abaqus, for Von Mises this involves equation [52] - [54]. (Simulia - Abaqus 6.14, 2016)

$$q = \sqrt{\frac{3}{2}(S_{ij}S_{ij})} \quad [52]$$

Where S_{ij} is the deviatoric stress, defined as

$$S_{ij} = \sigma_{ij} + p\delta_{ij} \quad [53]$$

Where δ_{ij} is the Kronecker delta, which is the identity matrix, and p is the equivalent pressure stress, defined as

$$p = -\frac{1}{3}\sigma_{ii} \quad [54]$$

The general Von-Mises criteria can also be written as equation [55]

$$2\sigma_y^2 = (\sigma_1 - \sigma_2)^2 + (\sigma_2 - \sigma_3)^2 + (\sigma_3 - \sigma_1)^2 \quad [55]$$

Where σ_y is the yield stress, σ_1, σ_2 and σ_3 is the principal stresses in x, y and z, respectively. (Reuben, 1994)

The Tresca criterion can be calculated by equation [56]. (Reuben, 1994)

$$\sigma_y = (\sigma_1 - \sigma_3) \quad [56]$$

9.2.5 Air modelled as compressible

In one of the load cases for the structure the air is modelled as compressible, here a 1st order implicit time scheme in Star-CCM+ has been used, with 24 inner iterations. This was recommended by personal discussions with Andreas Svendsen, where he used the same geometry in his CFD simulations with air modelled as compressible. The air is modelled with a polytrophic relation, where equation [57] has been used to determine the air properties.

$$\frac{P}{P_0} = \left(\frac{\rho}{\rho_0}\right)^k \quad [57]$$

Where P is the pressure in the cavity, P_0 the reference pressure, ρ is the density in the cavity, ρ_0 the air density and k is a polytrophic index equal to 1.375. (Svendsen, 2017)

10 Loads on the aft with incompressible air and one-way coupling

When the lifeboat is in the submerged phase an air cavity as described in section 6.1.2 will form, this air cavity combined with hydrostatic pressure will create pressure on the aft part of the lifeboat. When the air cavity closes a high pressure peak occurs. The lifeboat should be able to withstand the pressure and pressure peak without large deformation, because this is normally the location of the entrance/exit to the lifeboat. With large deformations this door can be damaged and exiting the lifeboat after the dive would be hard.

For these simulations, the air is modelled as incompressible and a one-way coupling between the two programs has been established, where Abaqus solves with a dynamic implicit quasi-static approach, as mentioned in section 9.2.1. Since there are being used an implicit co-simulation time scheme, the exchange of data from Star-CCM+ to Abaqus is set to two times between each time step, one time in the middle of the time step and one time at the end of the time step. All shell thicknesses have been used for this case.

10.1 Validation of the forces and solver

The imported forces from Star-CCM+ boundaries are mapped onto each unique nodal in Abaqus. These forces should follow the same tendency, but some discrepancies due to the mapping interpolation is expected.

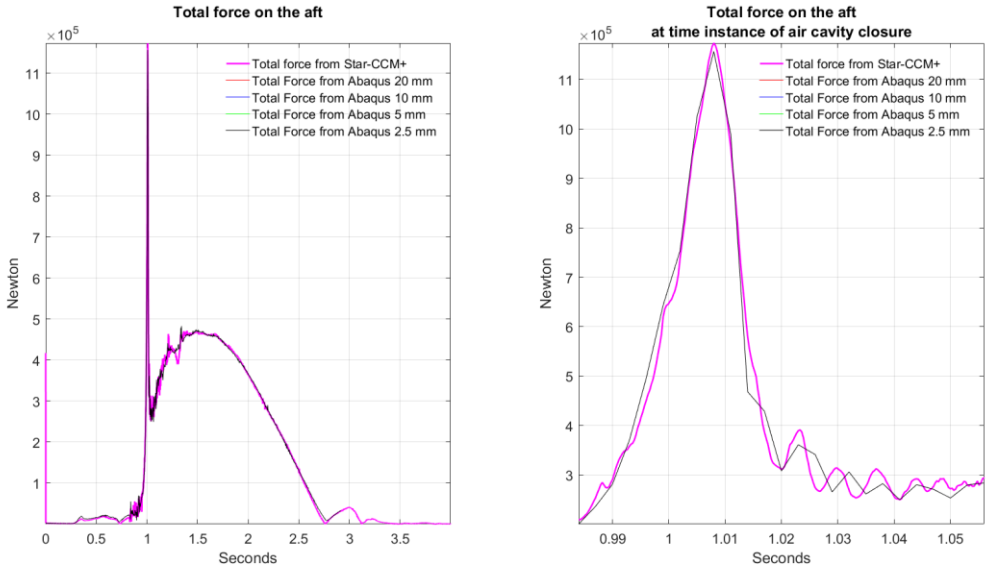

Figure 10.1: Total force from Star-CCM+ vs total force from Abaqus on the aft

As seen in Figure 10.1 the two programs have the same tendency of the forces on the aft. This implies that the establishment between them is successful. There are some discrepancies, mainly for the forces acting on the 5 mm and 2.5 mm shell thickness, where the peak value is slightly lower in Abaqus. Other than that, the forces are of similar size and follows the same tendency.

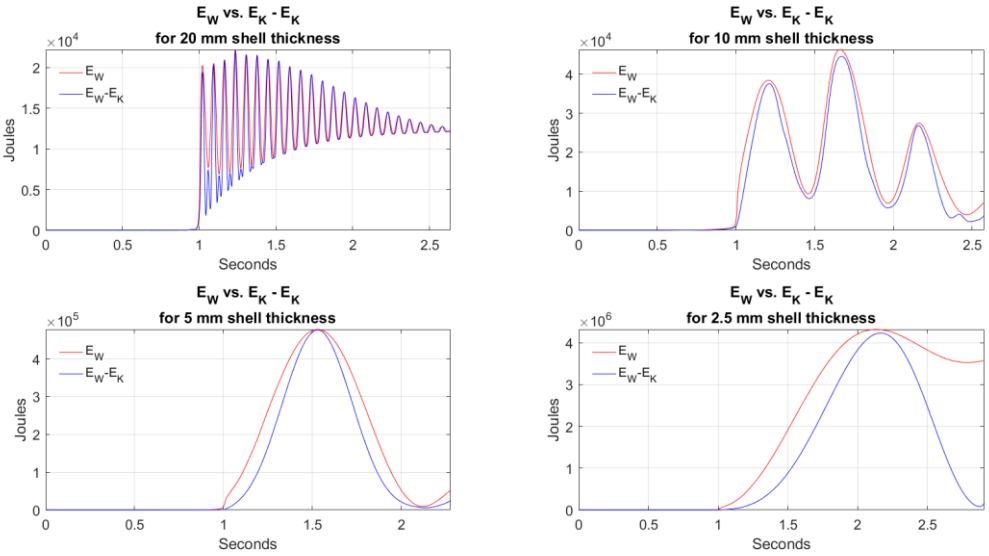

Figure 10.2: External work versus external work minus kinetic energy for the quasi-static solver check, when air is modelled as incompressible

As seen from Figure 10.2 the difference between the work energy, E_W, and work energy minus the kinetic energy, $E_W - E_k$, increases as the shell thickness decreases. This implies that the inertia term

becomes stronger in the solver for a decrease in shell thickness. The difference for the 20 mm thickness is relatively small, but still too large to assume a fully quasi-static solution. It is therefore assumed that the results are obtained with some dynamic effects for all shell thicknesses.

10.2 Stresses

The low duration of the high force from the air cavity closure can be seen as an impulse load. This force makes the aft part oscillate and it is necessary that the aft can withstand this load and the oscillations without yielding.

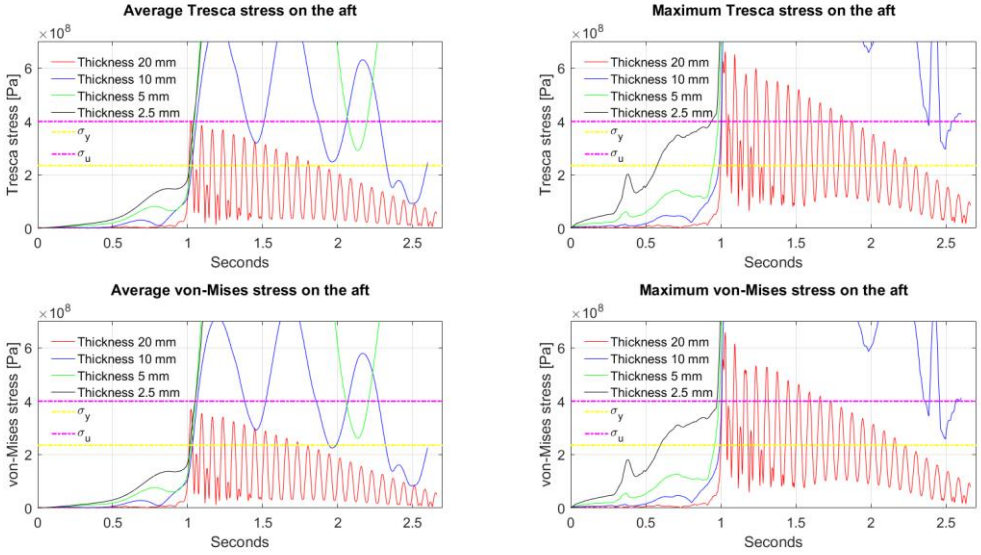

Figure 10.3: Plots of average and maximum Tresca and von-Mises stress on the aft

As seen in Figure 10.3, the average von-Mises and Tresca stresses for a shell thickness of 20 mm is barely within the ultimate strength, while for all the other shell thicknesses it is exceeded. The maximum von-Mises and Tresca both exceeds the ultimate strength for the 20 mm shell. This implies that plastic deformations are a strong factor on the aft when the air is modelled as incompressible. Since the material is modelled as elastic with no plastic properties these large stresses do not result in buckling in the simulations, and as seen for shell thickness 10 mm, 5 mm and 2.5 mm the average von-Mises and the maximum von-Mises is well above the yield criterions and therefore the plots in Figure 10.3 is zoomed in to capture the 20 mm thickness.

a) b)

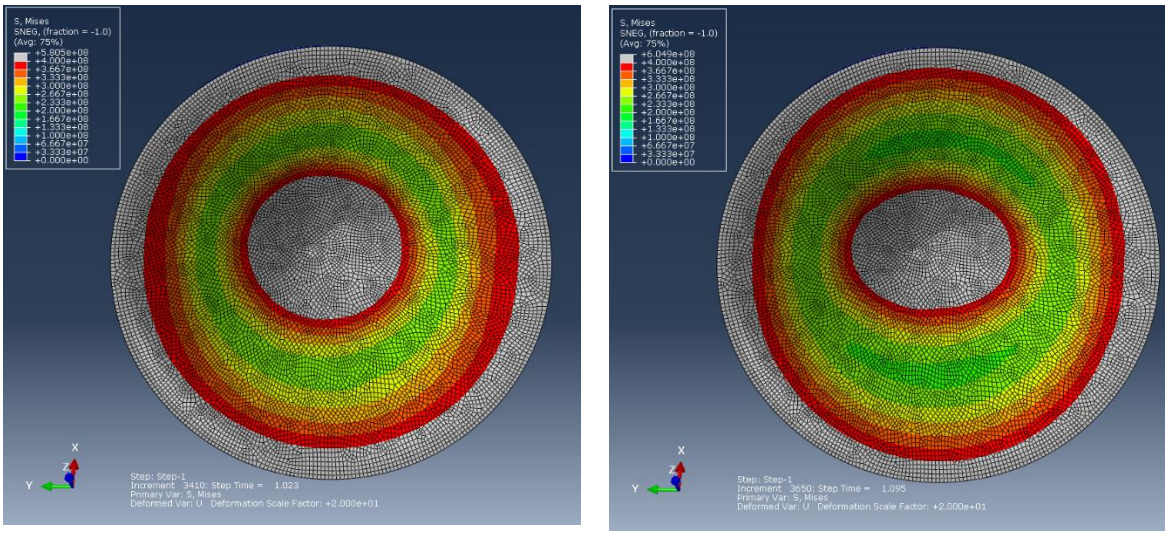

Figure 10.4: Shows the von-Mises stress on the aft with shell thickness 20 mm and a deformation scale factor of 20, where the grey area is above the ultimate strength and a) shows Δt = 1.023 s and b) shows Δt = 1.095 s

Figure 10.4 shows the time instance of the two largest peaks in von-Mises stresses for both average and maximum from Figure 10.3. As seen from Figure 10.4 a) and b) the largest stresses occur on the elements at the outer and inner diameter.

As seen from the time instance for where the air cavity closure, at 1.008 s until 2.5 s in Figure 10.3, the stresses oscillates. The period of these oscillations decreases as the shell thickness goes down, which is due to the change in stiffness of the material and the different natural frequency of the aft plate.

10.3 Displacements

The displacements are obtained from Abaqus with each unique node displacement from the coordinate system defined in the middle of the aft, as seen in Figure 8.4. The values presented is taken from four nodes in the middle of the plate, as seen from Figure 10.5. The four nodes selected is the nodes which will have the max displacement, as seen from Figure 10.6, where the figure shows the second oscillation after the impulse load hits the aft, and that it is node 8757 and 8759 which has the largest displacement for all shell thicknesses.

a)

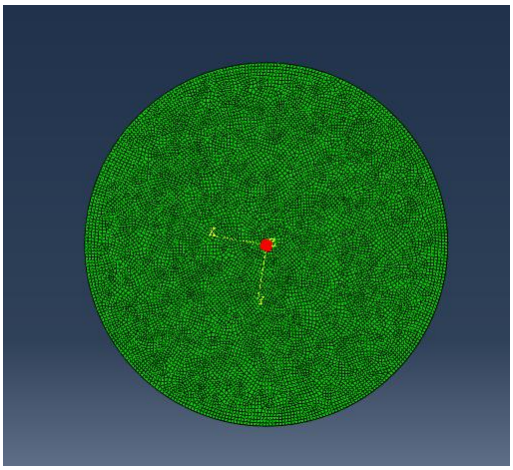

b)

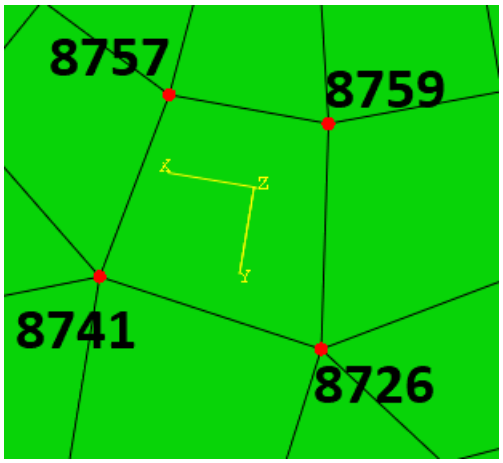

Figure 10.5: Nodes used for displacements a) Location of the four nodes b) zoomed in on the nodes

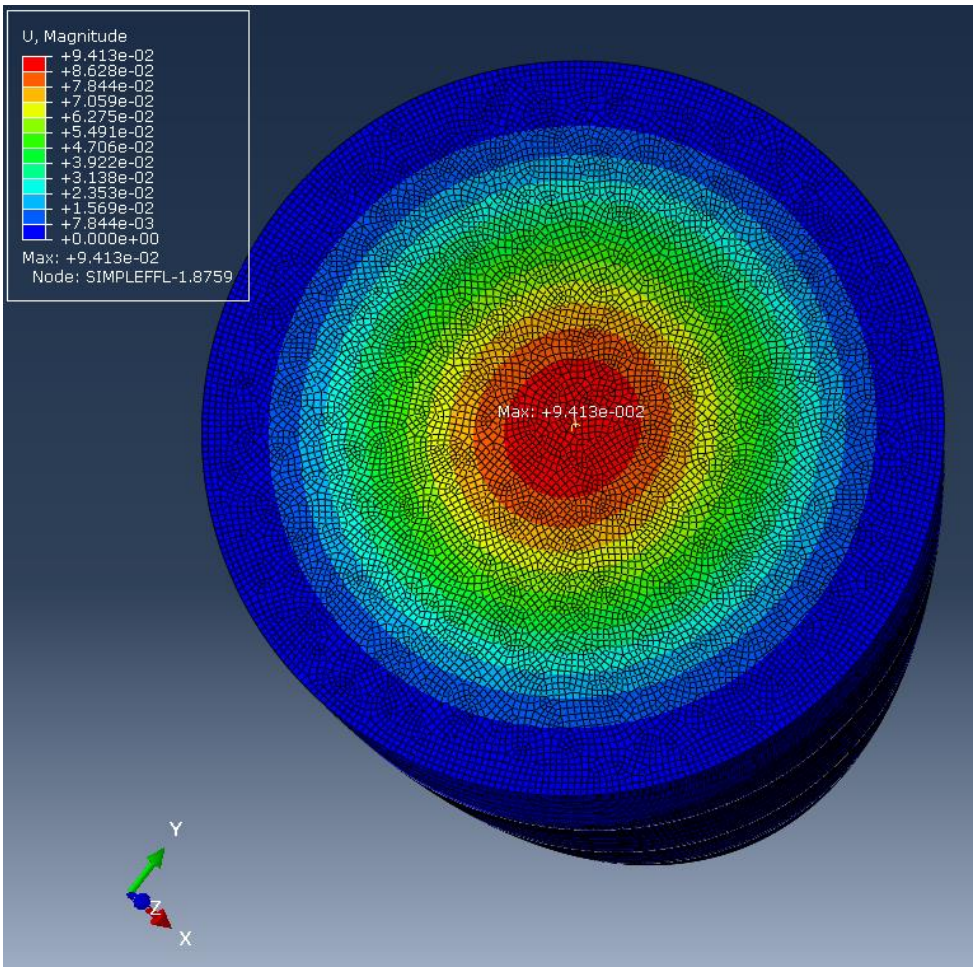

Figure 10.6: Displacement of all the nodes on the aft part at $\Delta t = 1.095\ s$, where node 8759 excites the largest deformation

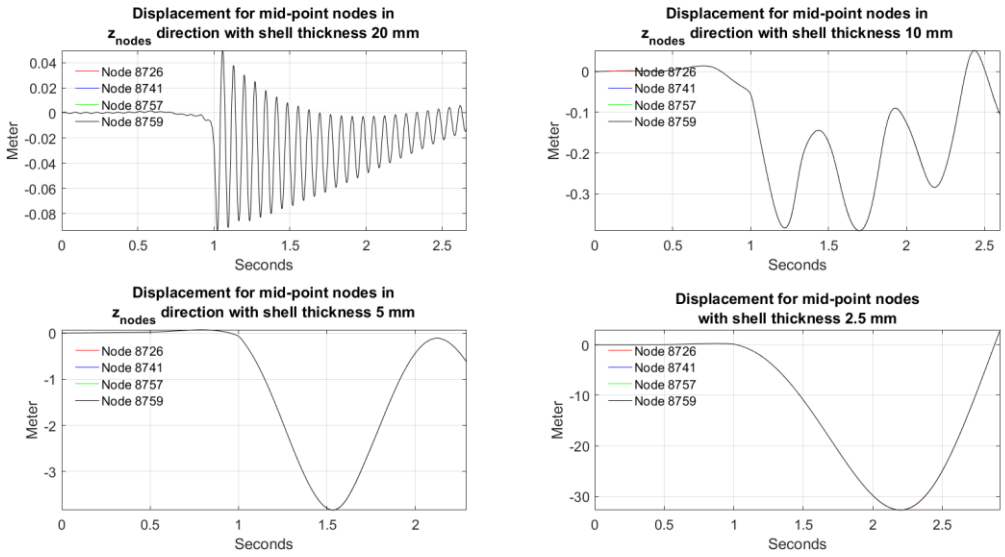

Figure 10.7: Displacement for nodes 8726, 8741, 8757 and 8759 for all shell thicknesses where the values are taken in the z_{nodes}-direction

SHELL THICKNESS	**20 mm**	**10 mm**	**5 mm**	**2.5 mm**
OSCILLATION PERIOD $[s]$	0.072	0.483	-	-
MAX DISPLACEMENT $[m]$	-0.0937	-0.3908	-3.8345	-32.6560
NODE 8726 $[m]$	-0.0937	-0.3902	-3.8306	-32.6797
NODE 8741 $[m]$	-0.0936	-0.3906	-3.8324	
NODE 8757 $[m]$	-0.0937	-0.3908	-3.8345	-32.6941
NODE 8759 $[m]$	-0.0937	-0.3906	-3.8341	-32.6840

Table 10.1: Average oscillation period and node displacements in z_{nodes} direction for each plate thickness

As seen from Figure 10.7 and Table 10.1 the displacement for the four nodes is almost equal for all thicknesses. If the assumed max displacement before fracture is taken as 0.22 m, as in Andrea Califano & Brinchmann (2013), it is only the thickness 20 mm which will not suffer from fracture by the displacements. While all the other shell thicknesses do not withstand the loading from the air cavity closure, when air is modelled as incompressible. (Califano & Brinchmann, 2013)

As seen from Figure 10.7 the largest oscillation occurs at 1.023 s, 1.218 s, 1.53 s and 2.199 s for a shell thickness of 20 mm, 10 mm, 5 mm and 2.5 mm, respectively. While the air cavity closure happens at 1.008 s. This difference is due to the force acting as an impulse and therefore the structure needs time to respond to the load, due to the inertia effects.

a) b)

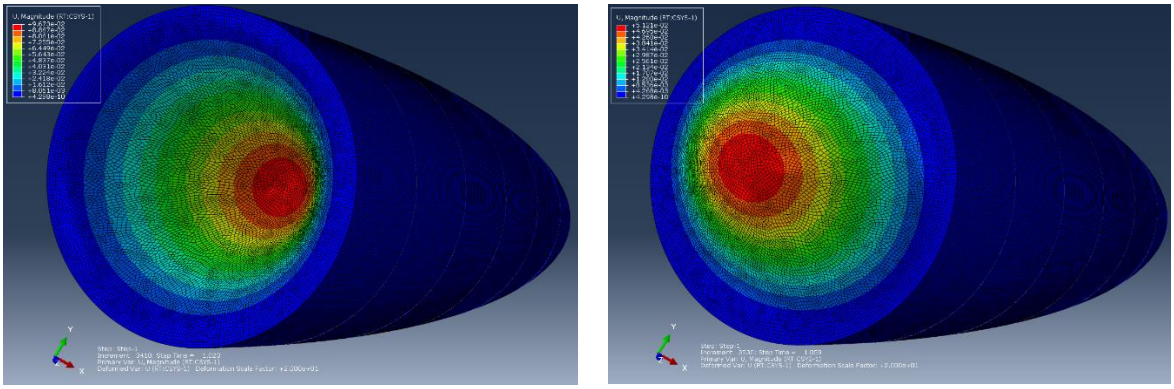

Figure 10.8: Shows the displacements of the shell thickness 20 mm with a deformation scale factor of 20, where the time instance of a) is 1.023 s and b) is 1,044 s

The oscillation periods obtained from the displacements lies close to eigenmode 1 for 20 mm and 10 mm, as seen in Table 8.6 and Table 10.1, while the exact period of oscillation is hard to predict for the two thinner shells due to an abort of the simulation due to too large displacements for the solver. For the 20 mm shell thickness it is shown in Figure 10.8 a) and b) that the oscillation follows eigenmode 1.

The duration of the load, T_d, is taken as 0.0291 s, from 0.9909 s to 1.02 s in Figure 10.1, and by the use of the equation $\frac{T_d}{T_n}$ the ratio becomes 0.404 for the 20 mm shell thickness, where T_n is taken as 0.072 s from Table 10.1. As the shell thickness decreases this ratio will decrease due to the larger natural frequencies. Which implies that the force from the water jet can be seen as an impulse when the air is modelled as incompressible. By utilizing this assumption into equation [48], where the impulse load is equal to $1.9386*10^4$ Ns in the negative z_{nodes}-direction, and $\xi = 0.0169$ by using equation [49]. The natural frequency as $\omega_n = \frac{2\pi}{0.072}$ and the undamped natural frequency, ω_{n0}, as eigenmode 1 for the 20 mm shell thickness in Table 8.6. The particular response in the structure is found, as seen in Figure 10.9.

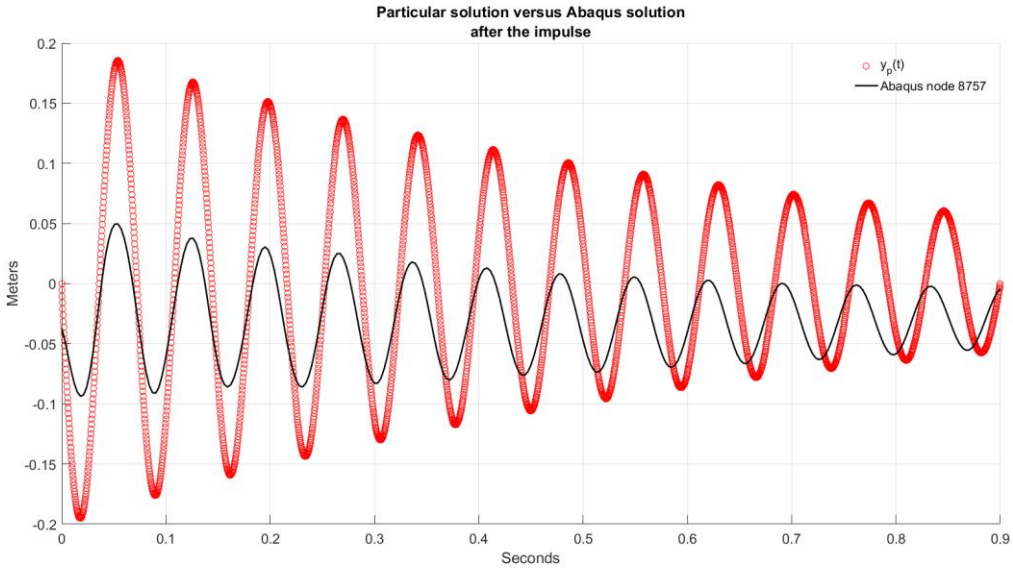

Figure 10.9: Maximum response by equation [48] versus Abaqus results, where the Abaqus results are superimposed such that the maximum response from both methods are in phase. This is done for a shell thickness of 20 mm.

The difference in oscillation period is connected with the solving method, this is because of the density in the air bubble will not change, due to the incompressible air, and therefore the oscillations will be close to the oscillations if the whole body was dry. This means that the inertia effects in the dynamic implicit quasi-static is not fully accounted for, and by using equation [48] to get the theoretical maximum response, it is seen by Figure 10.9 that this assumption seems valid. The difference of the oscillation periods increases as the time goes on, due to the hydrostatic pressure in the Abaqus solution. From this it is assumed that the plate does not behave quasi-static, and by using Figure 9.2 it can be assumed that hydroelastic effects is of importance.

11 Loads on the aft with incompressible air and two-way coupling

As it is found from section 10.3 that hydroelastic effects is of importance, the two-way coupling should take this effect into account in the simulation. This is due to the constant interaction between the two programs. Since it was only the shell thickness of 20 mm which had close to realistic results, at least with respect to displacements, this thickness is the only one with a two-way interaction between Star-CCM+ and Abaqus which will be conducted. The two-way interaction means that the forces are given as input to Abaqus, and the nodal displacements from Abaqus as input to Star-CCM+. The mapping settings is set to the Least Square method and that it is Star-CCM+ that controls this mapping. Since the rate of this exchange of inputs/outputs can affect the end results the exchange rate were set to 5 times between each time step.

Due to large computational time, and therefore CPU cost, this was done with mesh discretization Δx_3 in Star-CCM+ and $\Delta x_{2_{FEM}}$ in Abaqus. Even with this simplification the results obtained after a solving time of 120 hours, were equal to a solution time of approximately 3 s. By using Δx_3 it means that the forces of the air cavity closure on the aft will be smaller than with mesh discretization Δx_2, with a difference of approximately 230 kN.

The results with the two-way interaction will be compared with the results obtained for Δx_3 in the convergence study.

11.1 Validation of forces and displacements

The same Abaqus input file as in section 10 is used, but since there is used another mesh discretization for Star-CCM+, a new validation of forces is conducted. A validation of the displacements obtained in Star-CCM+ from Abaqus is also conducted.

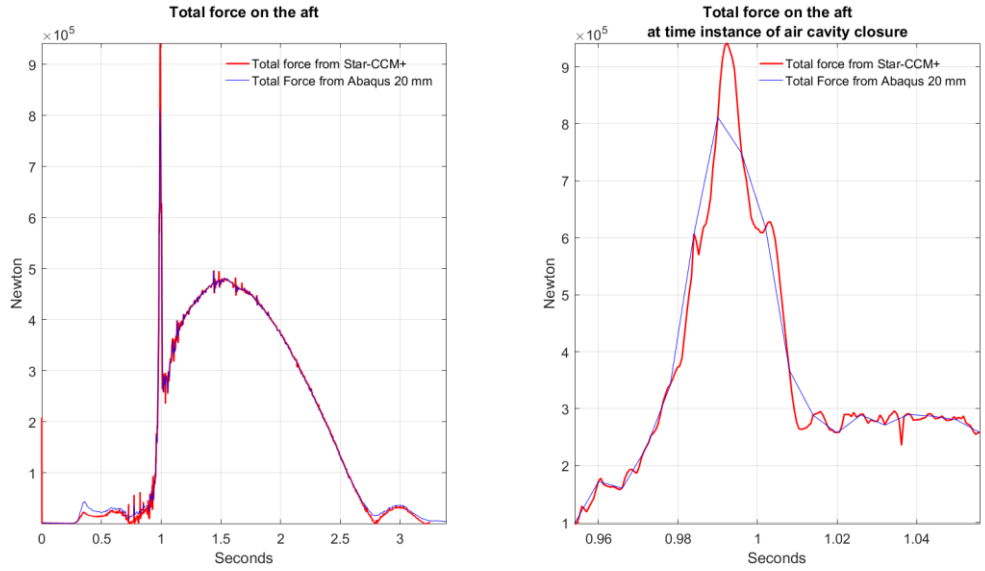

Figure 11.1: Force, taken as magnitude, on the aft with two-way coupling

As seen in Figure 11.1 the force magnitude between the two programs are of the same tendencies, but with more discrepancies than in the one-way coupling (Figure 10.1). As the aft starts to submerge Abaqus overpredicts the forces, while for the air cavity closure Abaqus underpredicts the forces. The two programs still have the same tendency of the forces.

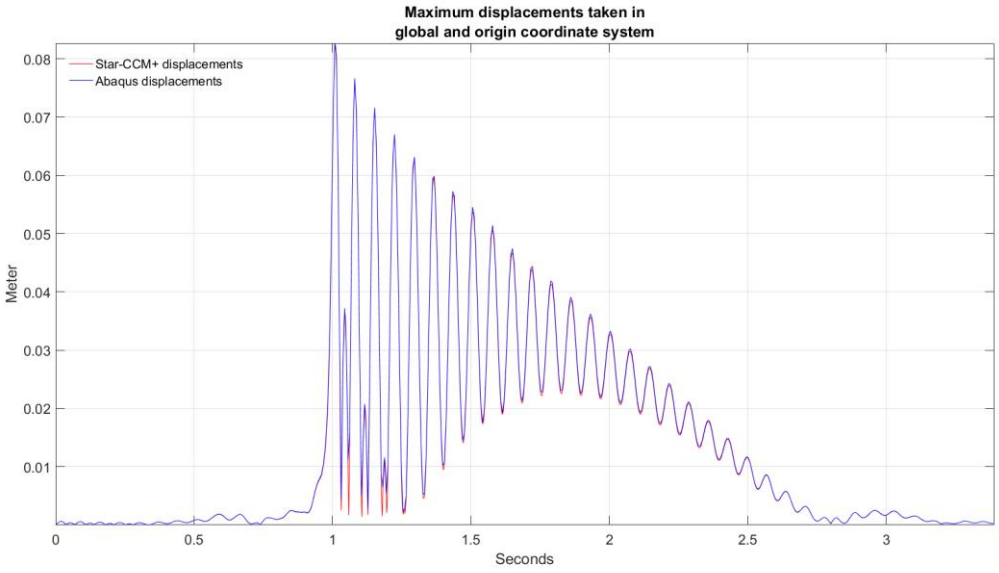

Figure 11.2: Maximum displacement magnitude of the aft, where Star-CCM+ has used n_{global} coordinate system and Abaqus n_{origin} coordinate system

Due to a moving body in Star-CCM+ versus a stationary body in Abaqus, the coordinate systems used in Figure 11.2 are with respect to [0, 0, 0], which is n_{global} for Star-CCM+ and n_{origin} for Abaqus. As seen

in Figure 11.2 the two programs communicate well with respect to the displacement, the main difference is the lowest values after the air cavity closure. While the maximum values are predicted well by both programs.

By using Figure 11.1 and Figure 11.2 it is seen that the two programs communicate well, and that the two-way coupling in this regard seems well-established.

11.2 Path

The trajectory of the lifeboat with two-way coupling is presented in Figure 11.3.

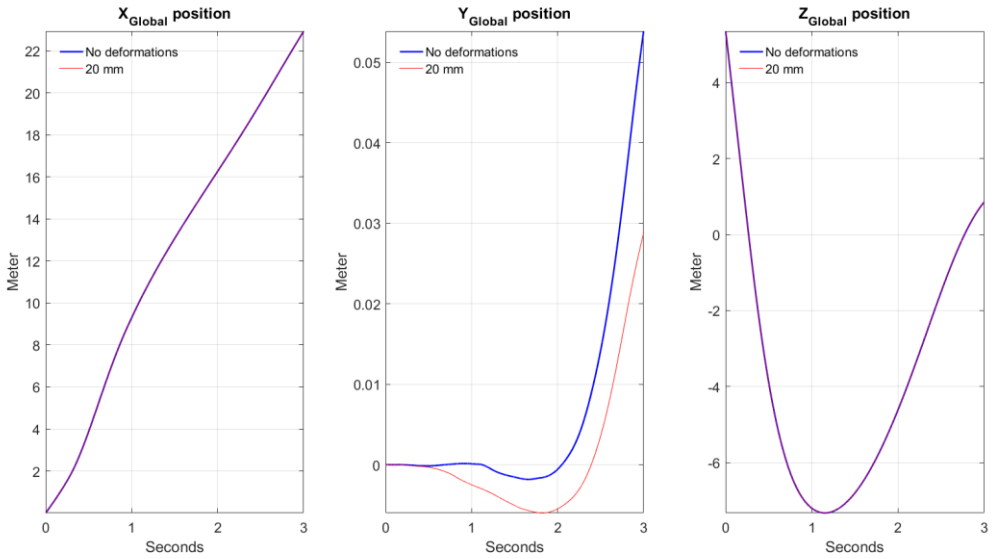

Figure 11.3: Position from Star-CCM+ with two-way coupling

Figure 11.3 shows that there is small difference in x_{global} - and z_{global} – direction when the hydroelastic effects are accounted for. While in the y_{global} – direction the difference is larger, the lifeboat starts earlier to translate into the negative y_{global} – direction, and with a larger magnitude than without deformations. On the other hand, the maximum translation in the positive y_{global} – direction is smaller. The lifeboat still follows the preferred trajectory, motion pattern 1, from DNV-GL. (DNV-GL, 2016)

11.3 Pressure

The average pressure on the aft with the two-way coupling is presented in Figure 11.4.

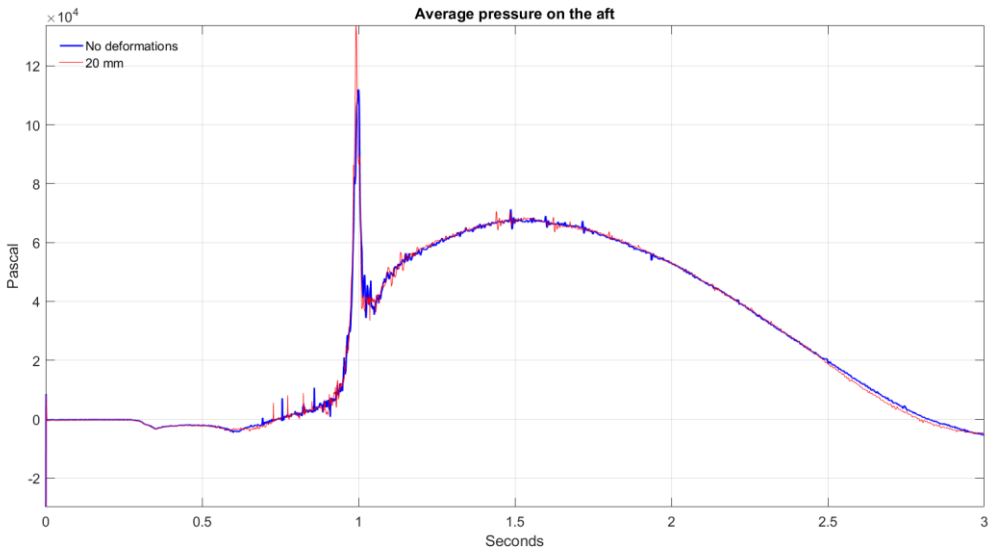

Figure 11.4: Average pressure from Star-CCM+ with two-way coupling

Figure 11.4 shows that the two-way coupling affects the air cavity closure. The air cavity closes 7 ms sooner, the magnitude of the pressure from the air cavity closure is larger and the average pressure has a small decrease in size as the lifeboat is closer to the water surface. Even with these changes the tendency is the same.

11.4 Acceleration

The accelerations in x_{body} – and z_{body} – direction with the two-way coupling are presented in Figure 11.5.

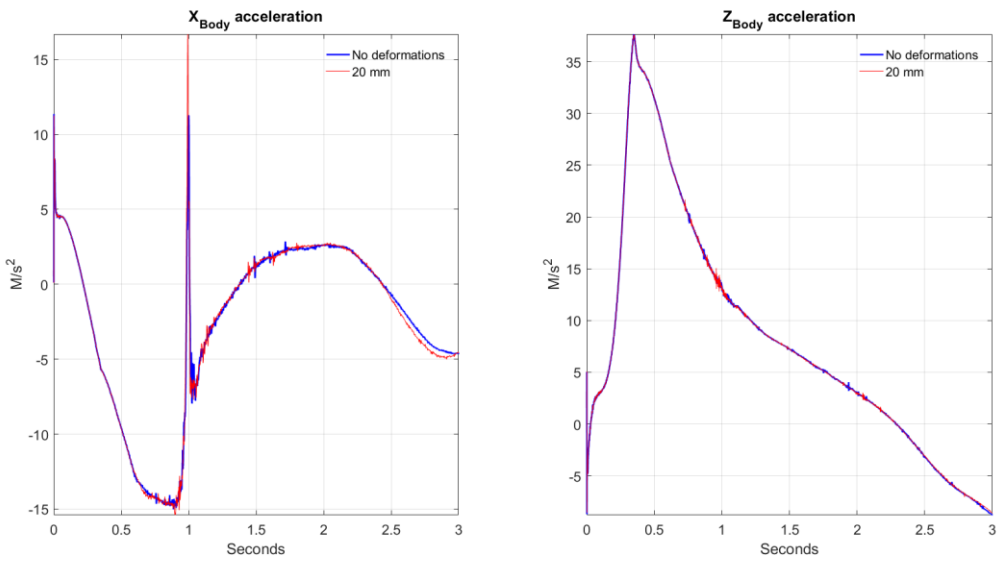

Figure 11.5: Acceleration from Star-CCM+ with two-way coupling

Figure 11.5 shows that there is difference in the acceleration in the x_{body} – direction, while for z_{body} – direction there are close to zero difference. As it is mentioned in section 6.4 the acceleration and pressure is proportional. Which means, as mentioned in section 11.3, the air cavity closure behaviour is different and that there is difference of the values when the lifeboat starts its trajectory upwards, in the same manner as with the average pressure in Figure 11.4.

11.5 Stresses

As the force acting on the aft is higher in section 10, due to the mesh discretization in Star-CCM+ is different, the stresses acting on the structure in this section will be of a lower magnitude.

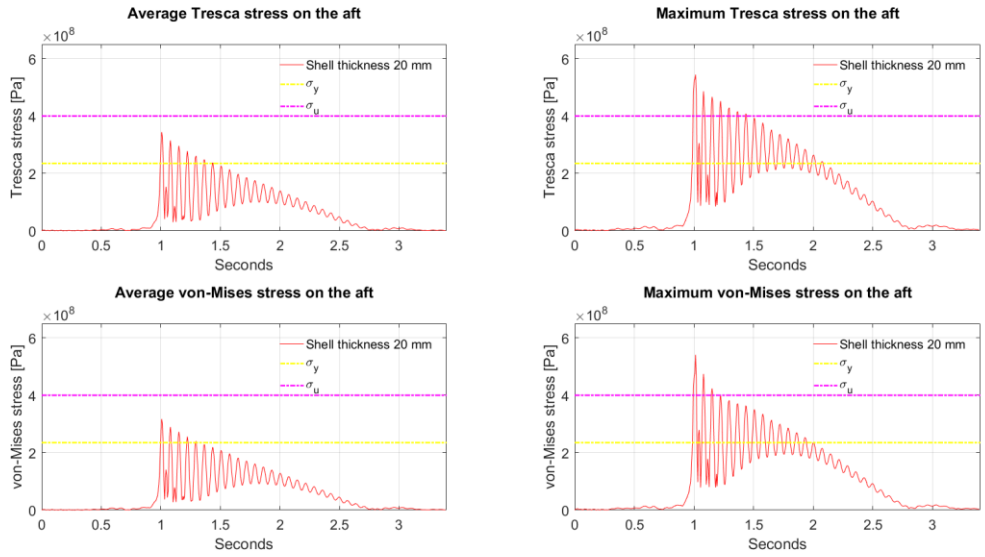

Figure 11.6: Plots of average and maximum Tresca and von-Mises stress on the aft with two-way coupling

By comparing Figure 10.3 and Figure 11.6 it is seen that the stresses from the criterions is of a lower magnitude, as expected due to the different Star-CCM+ mesh discretization's. In this case the average von-Mises and Tresca stresses are within the ultimate strength capacity, while the maximum values of the two criterions is well above.

As seen by Figure 11.6 the aft oscillates in the same manner as in section 10.

12 Loads on the hull with incompressible air and two-way coupling

Since the lifeboat hull experiences large slamming loads in the water-entry phase this is only been done with a two-way interaction. This is due to the assumption that hydroelastic effects matter in this phase. The frequency of the exchange between the two programs will have an effect of the end results, such that the exchange rate was set in the same manner as in section 11.

Due to the large computational time, as for the case in section 11, also here the mesh discretization used is Δx_3 for Star-CCM+ and $\Delta x_{2_{FEM}}$ for Abaqus. For the 5 mm shell thickness it will only be presented as Abaqus values due to an error under the saving of the Star-CCM+ file at Vilje.

12.1 Validation of displacements and solver

Due to a mistake when creating plots from the CFD simulations, the plots of the forces which is used for the mapping has not been obtained from Star-CCM+. Meanwhile, as the mapping of the forces was successfully mapped in the two other cases, section 10 and 11, it is assumed that this is the case for the hull as well.

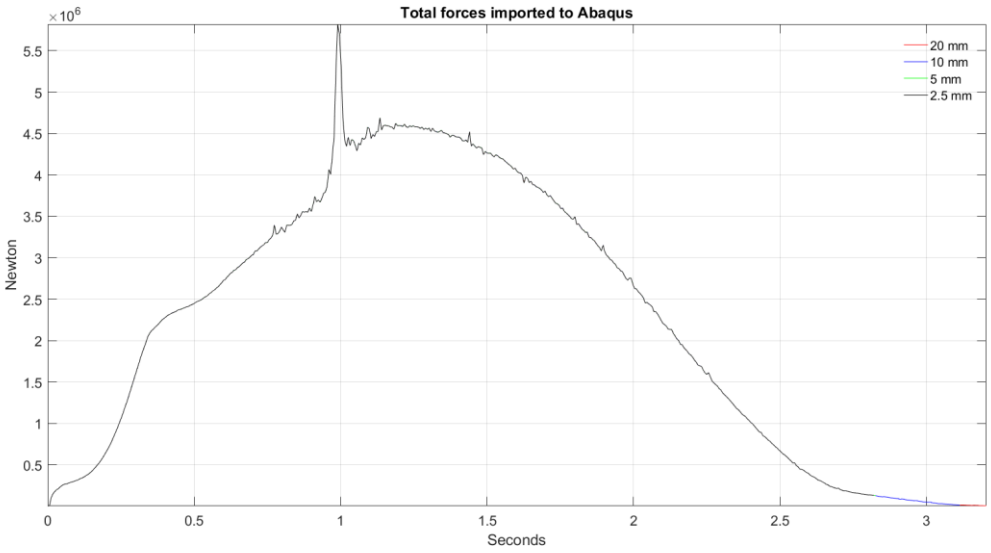

Figure 12.1: Star-CCM+ forces mapped to Abaqus for all shell thicknesses, plot values obtained only from Abaqus

As seen in Figure 10.1 the total forces acting on the hull is identical for all shell thicknesses, which gives an indication that the establishment is successful. A validation of the displacements obtained in Star-CCM+ for all shell thicknesses, except for 5 mm, have also been conducted.

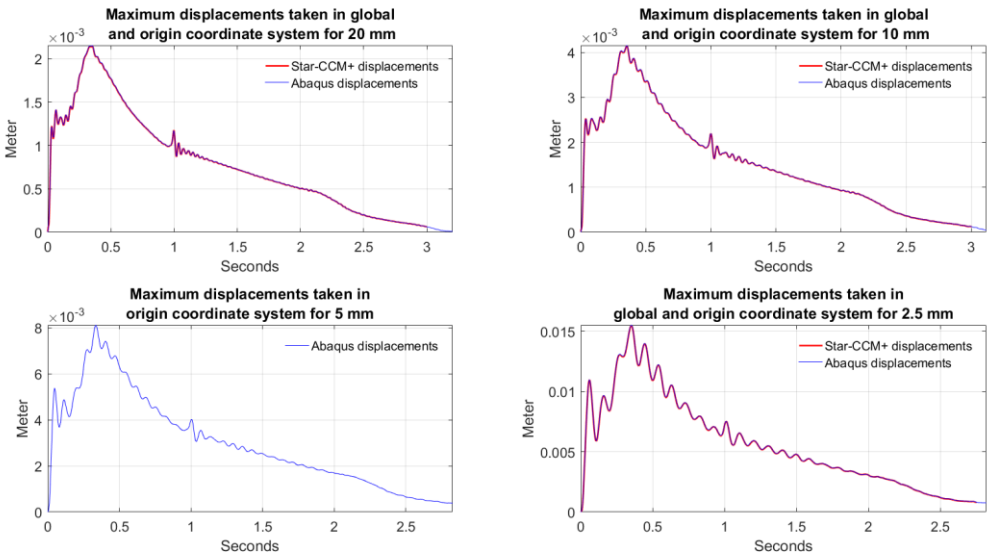

Figure 12.2: Maximum displacements for all shell thicknesses, where Star-CCM+ has used coordinate system n_{global} and Abaqus n_{origin}. The Star-CCM+ displacements for shell thickness of 5 mm is not included

As seen in Figure 12.2 the displacements between the programs are close to identical, which implies that the establishment of Star-CCM+ and Abaqus is good.

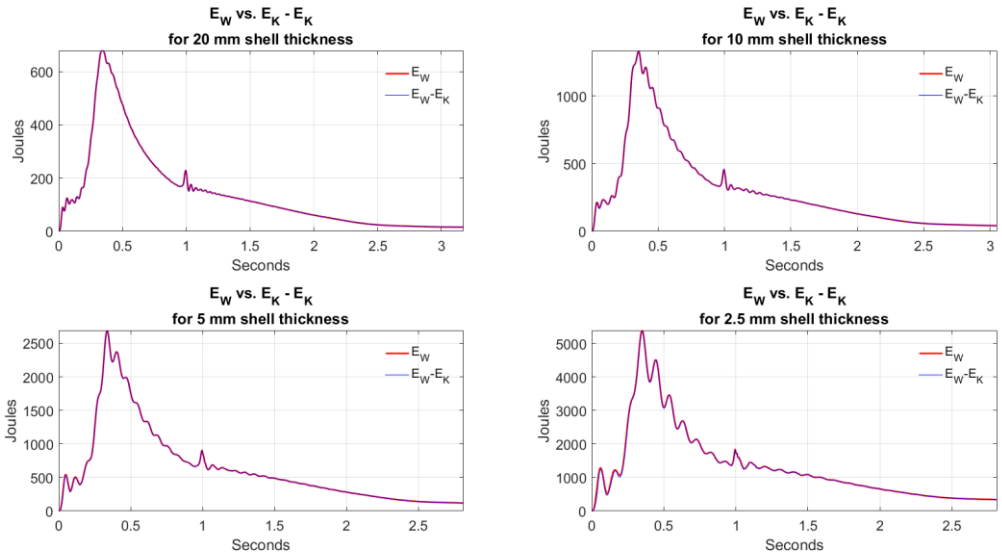

Figure 12.3: External work versus external work minus kinetic energy for the quasi-static solver check for hull, when air is modelled as incompressible

As seen in Figure 12.3 the difference of E_W and $E_W - E_K$ is insignificant, which implies that the solution is obtained with a quasi-static approach.

12.2 Path

The trajectory of the lifeboat with the two-way coupling when Abaqus solves for the hull is presented in Figure 12.4.

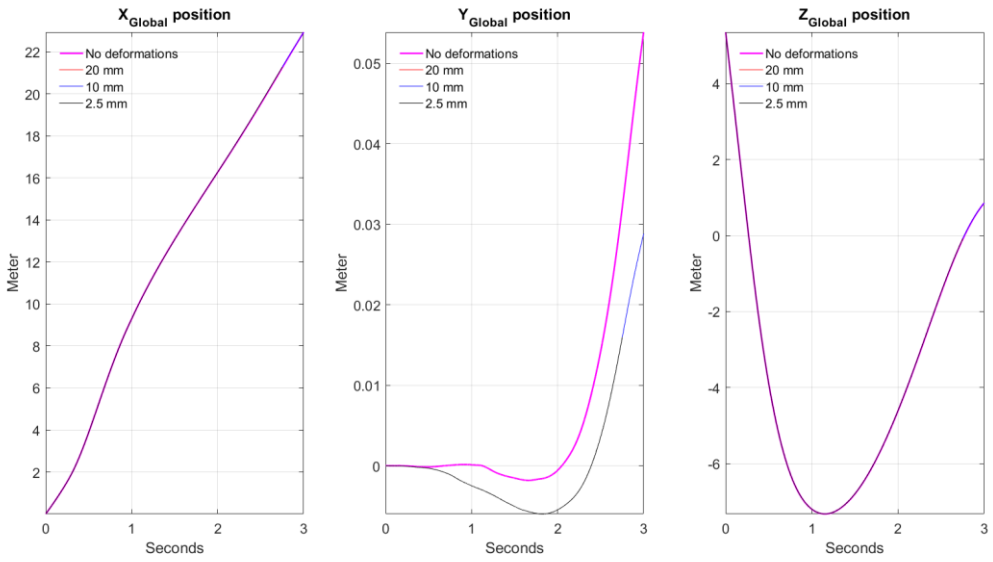

Figure 12.4: Position from Star-CCM+ of the lifeboat with two-way coupling when Abaqus solves for the hull

Figure 12.4 shows that there is only difference in the y_{global} – direction for the lifeboat, as in section 11.2. The lifeboat still follows the preferred trajectory, motion pattern 1, from DNV-GL. (DNV-GL, 2016)

12.3 Pressure

The average pressure on the hull of the lifeboat with two-way coupling is presented in Figure 12.5.

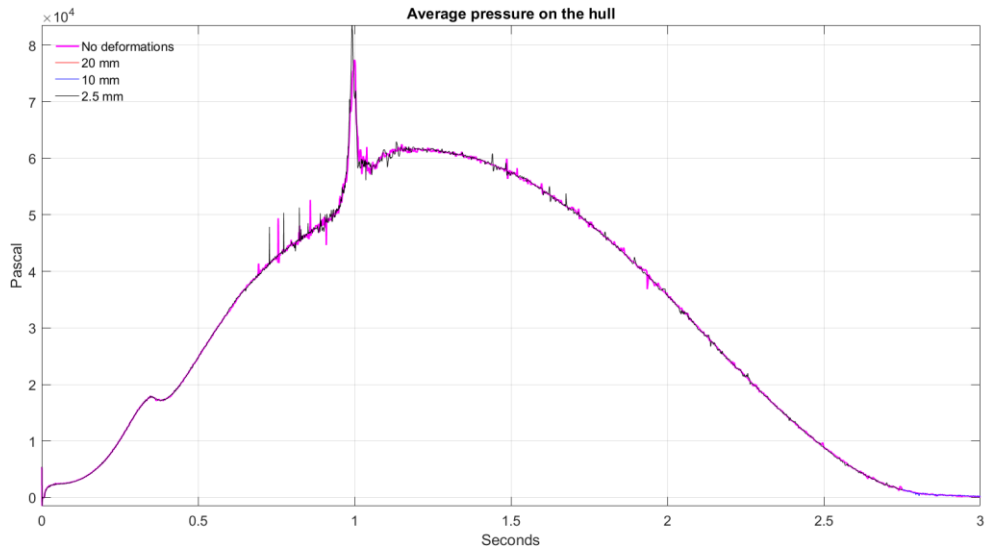

Figure 12.5: Average pressure from Star-CCM+ on the hull with the solution from the two-way coupling, when Abaqus solves for the hull. Shell thickness 5 mm is not included

Due to the limited solution time, the impact from the pop-up height is not covered in Figure 12.5. The pressure increases almost linearly until the air cavity closure, where the hull experiences the pressure in the same manner as for the aft. At approximately 1.25 s the pressure starts to decrease, which is due to the hydrostatic pressure decreasing as the lifeboat starts its trajectory towards the water surface.

12.4 Accelerations

The accelerations in x_{body} – and z_{body} – direction with two-way coupling for the hull are presented in Figure 12.6.

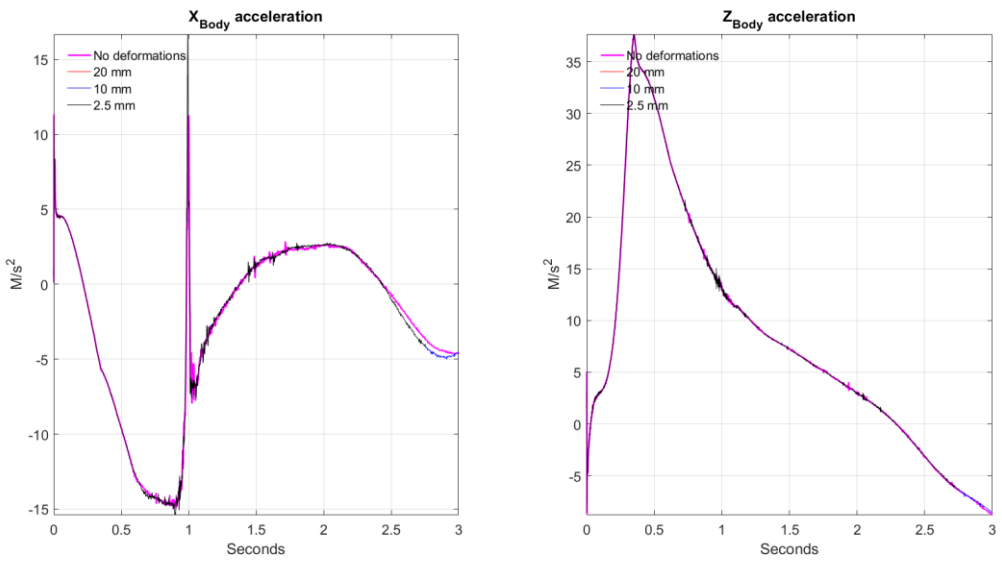

Figure 12.6: Accelerations from Star-CCM+ with two-way coupling, when Abaqus solves for the hull. Shell thickness 5 mm is not included

Figure 12.6 shows that it is only the air cavity closure which is experiences differences, as in section 11.4. The accelerations obtained is equal for all shell thicknesses.

12.5 Stresses

In the same manner, as in previous sections, the material used is only modelled with elastic properties. During the water entry phase, the hull experiences large local stresses, as the body becomes more and more submerged the stress on the hull will decrease.

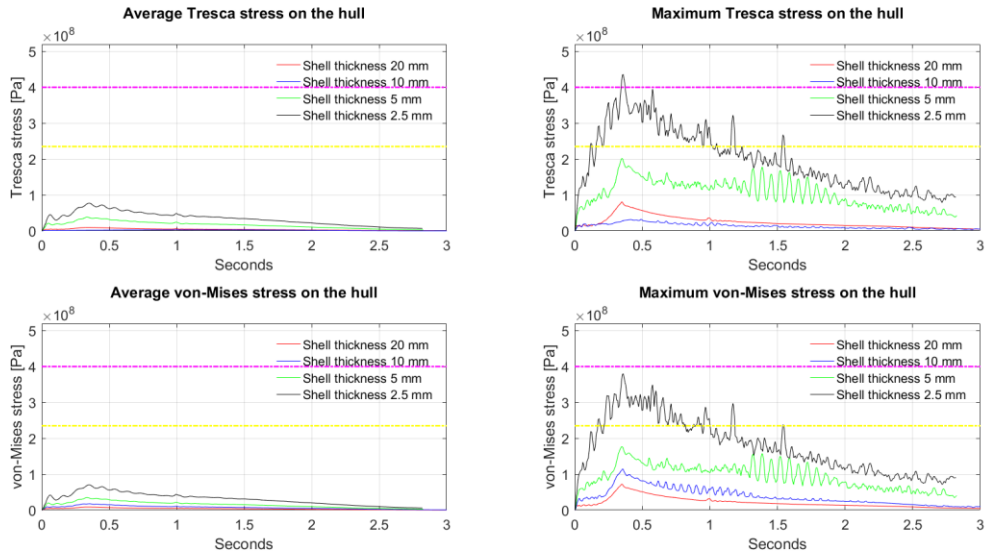

Figure 12.7: Average and maximum von-Mises and Tresca stress on the hull, where yellow is the yield stress and purple is the ultimate stress

Figure 12.7 shows that the average von-Mises and Tresca stress on the hull is well within the yield stress, but this is expected due to large local stresses will dominate, as the body moves into the water. It is only the shell thickness of 2.5 mm which enters the plastic zone, and exceeds the ultimate strength by using the Tresca criterion. This happens just as the aft hits the water surface.

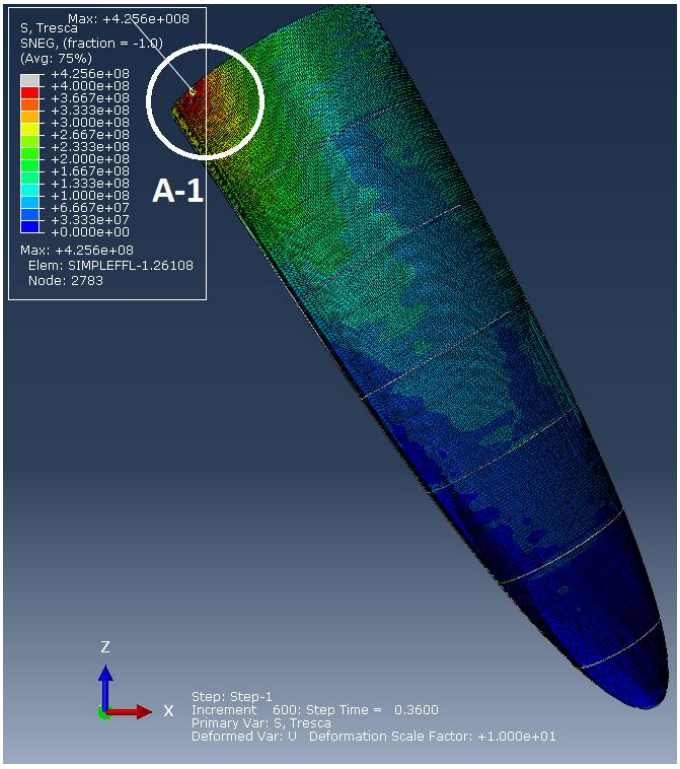

Figure 12.8: Location of maximum Tresca stress at Δt = 0.36 s

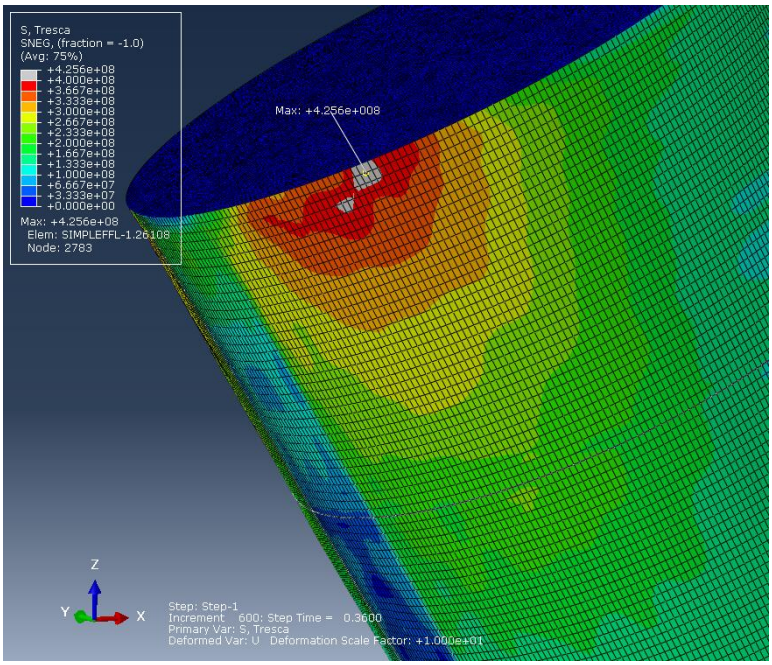

Figure 12.9: Cut A-1 from Figure 12.8, where the grey area is the area which exceeds ultimate strength

By comparing Figure 6.9 with Figure 12.8 and Figure 12.9 it possible to see the resemblance. The large stress occurs due to the splash crown.

As seen by Figure 12.7 there are some oscillations in the maximum stresses plots, these oscillations is not necessarily real, but a consequence of finding the maximum stress on any node for a given time.

12.6 Displacements

Due to the large difference of where the forces are acting on the hull, the displacements of specific nodes throughout the dive are not conducted. By using the results from Figure 12.2 the maximum displacements in Table 12.1 are obtained with the node with the corresponding displacement. Figure 12.10 shows the location of the nodes.

SHELL THICKNESS	**20 mm**	**10 mm**	**5 mm**	**2.5 mm**
MAX DISPLACEMENT [mm]	0.0022	0.0042	0.0081	0.0155
NODE NUMBER	98 088	98 088	98 088	104 024

Table 12.1: Displacements with two-way coupling for the hull

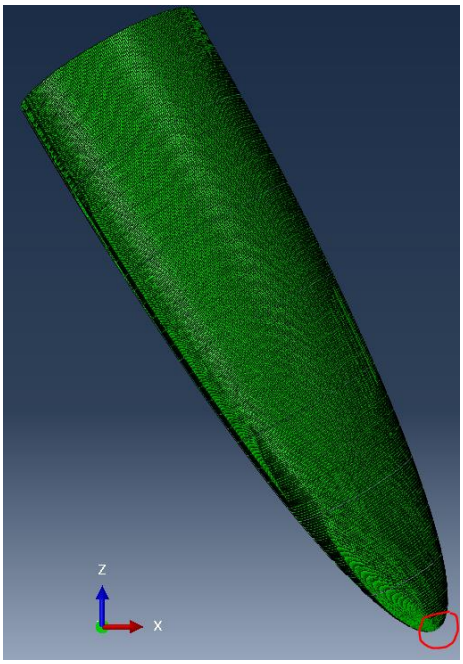

Figure 12.10: The red circle shows the location of the nodes where maximum displacements for the hull are

As seen in Figure 12.10 and Table 12.1 the maximum displacement occurs in the front of the lifeboat. It is the shell thickness of 2.5 mm which has the largest displacements, as expected. The maximum displacement is of 15.5 mm, which is not nearly close to 0.22 m.

13 Loads on the aft with compressible air effects and one-way coupling

As stated in section 6.4 in order to capture the pressures from the air cavity closure correctly and use FEM applications for the structural loads on the aft, the air should be modelled as compressible. This is concluded by Tregde (2015), Berchiche, et al. (2015) and Andrea Califano & Brinchmann (2013) in their studies with the usage of CFD for lifeboats. Beforehand in section 10 - 12 the air was modelled as incompressible, the results presented in this section, the air is modelled as compressible with polytrophic gas relation.

The results are obtained with a one-way coupling between the two programs, and due to the large computational time, because of the extended number of inner iterations, the solution time differs for shell thickness of 5 mm. The exchange rate of inputs is set to two times between each time step, as in section 10. The shell thickness of 2.5 mm is not included in this section.

13.1 Compressible air properties

With the use of equation [57] in section 9.2.5 for the air properties in the CFD simulation, Andreas Svendsen (2017) calculated the damping ratio, ξ, to be 0.064 for the polytrophic gas relation, as seen in Figure 13.1. Polytrophic and adiabatic gas relations gave higher eigenfrequencies than isothermal, which is expected to be underpredicted. The polytrophic gas relation gave the most realistic damping ratio. (Svendsen, 2017)

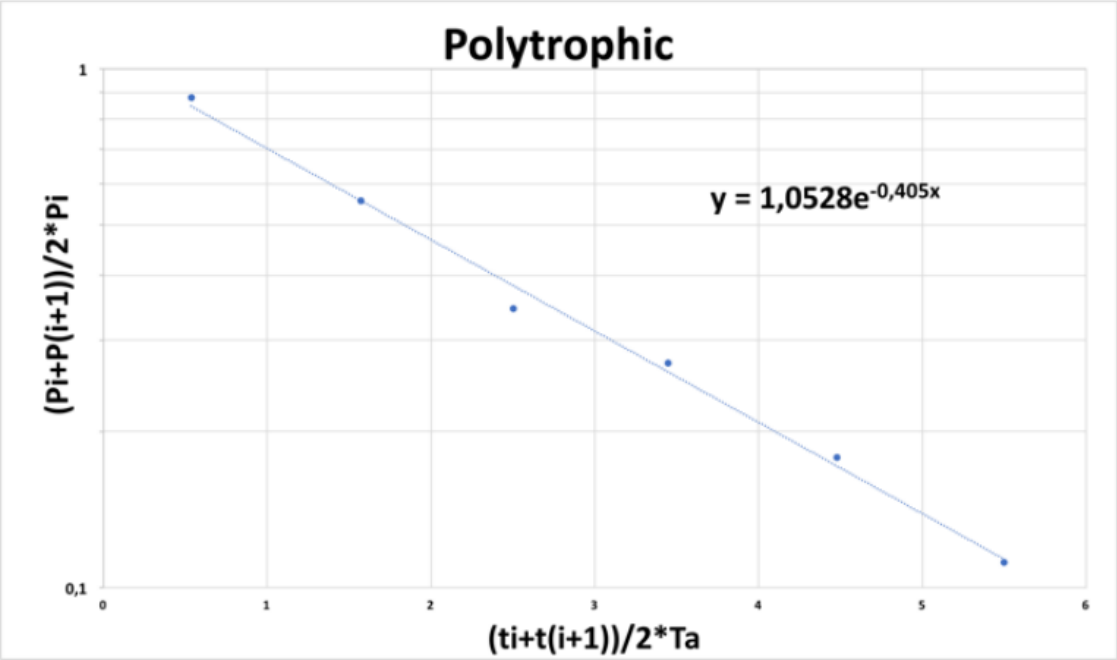

Figure 13.1: None dimensional pressure peaks plotted log linear against none dimensional period for polytrophic condition (Svendsen, 2017)

13.2 Validation of forces and solver

Since the air is now modelled as compressible a new validation of the forces is conducted. In the same manner as in section 10.1, the forces are mapped from Star-CCM+ onto the FEM model in Abaqus. The same tendency of the forces between the two programs is expected.

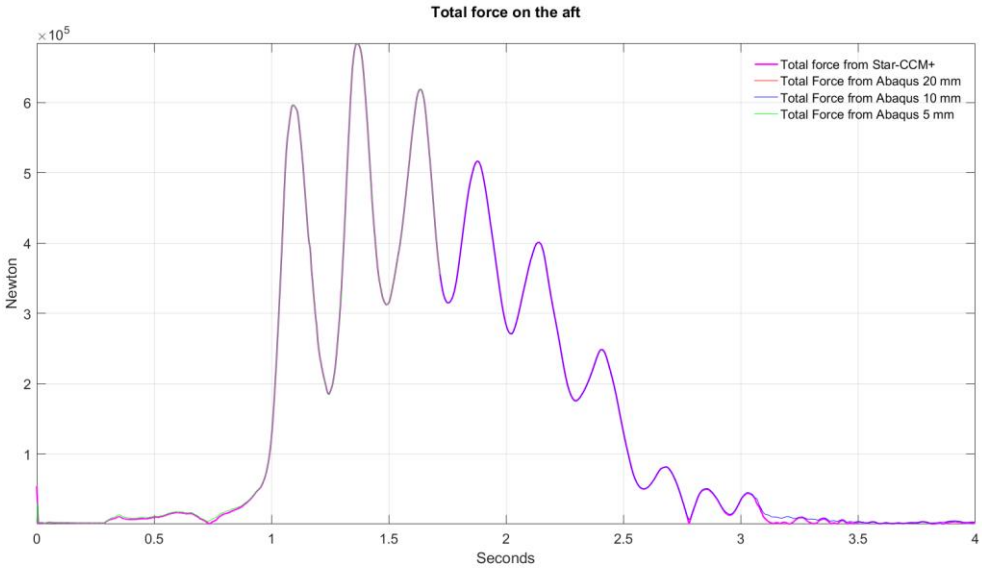

Figure 13.2: Total force on the aft part with compressible air, Star-CCM+ versus Abaqus

As seen in Figure 13.2 the forces have the same tendency, but with small discrepancies at 3.1 s – 3.5 s for all the shell thicknesses. The difference is small and therefore it is concluded that the interaction between the two programs is well-established.

In section 10 the forces from the air cavity closure could be treated as an impulse force. As seen in Figure 13.2 this is not the case. The forces oscillate with a period of 0.273 s, due to the behaviour of the air bubble on the aft. These oscillations will affect the stresses in much of the same manner.

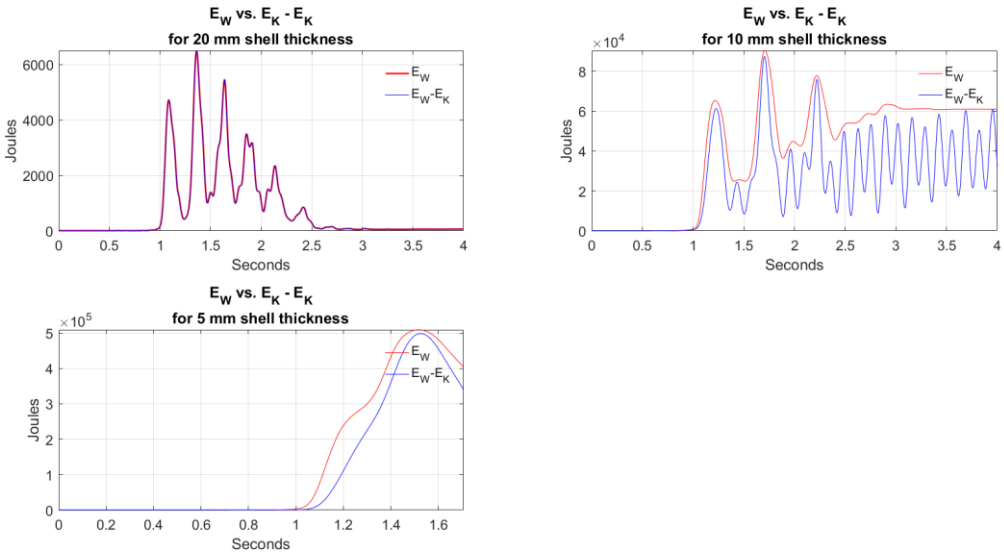

Figure 13.3: External work versus external work minus kinetic energy for the quasi-static solver check, when air is modelled as compressible

As seen by Figure 13.3 the difference in E_W and $E_W - E_k$ is minimal for the 20 mm shell thickness, the difference increases as the shell thickness decreases. This shows that the solution for 20 mm shell thickness follows the quasi-static approach. While for the other shell thicknesses the inertia term in equation [44] is more pronounced.

13.3 Stresses

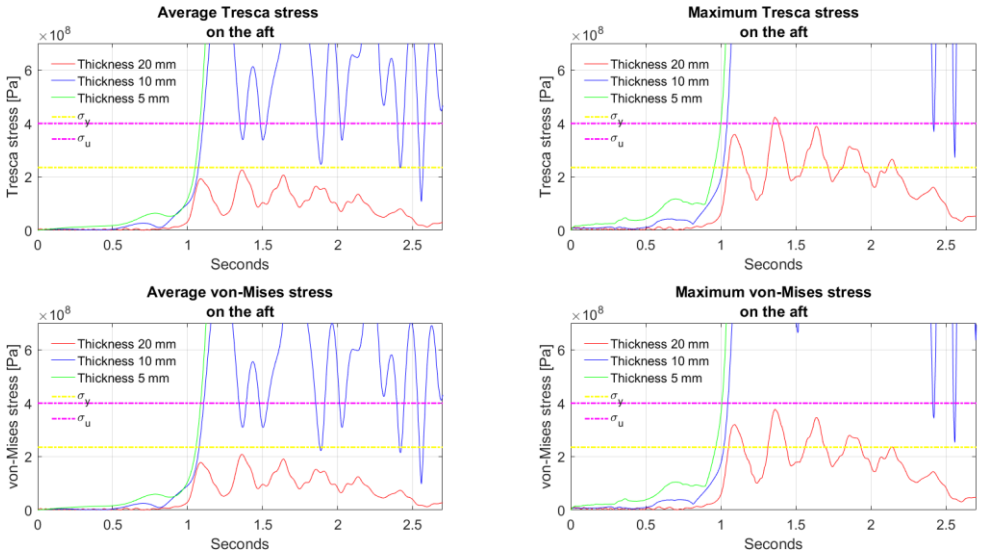

Figure 13.4: Von-Mises and Tresca stress on the aft when the air is modelled as compressible

As seen by Figure 13.4 the average von-Mises and Tresca stresses on the 20 mm shell thickness is within the elastic zone of the aft. The 20 mm shell thickness will withstand the forces from the air cavity closure, as seen by the maximum von-Mises and Tresca stresses, but as the hydrostatic pressure increases, combined with the oscillations of the air bubble, the forces on the aft increases such that the material enters the plastic zone. By using the Tresca criterion it is seen that the stresses exceed the ultimate strength, while for von-Mises it does not. For the shell thickness of 10 mm and 5 mm it is seen in Figure 13.4 that the von-Mises and Tresca stress exceeds the ultimate strength.

a)

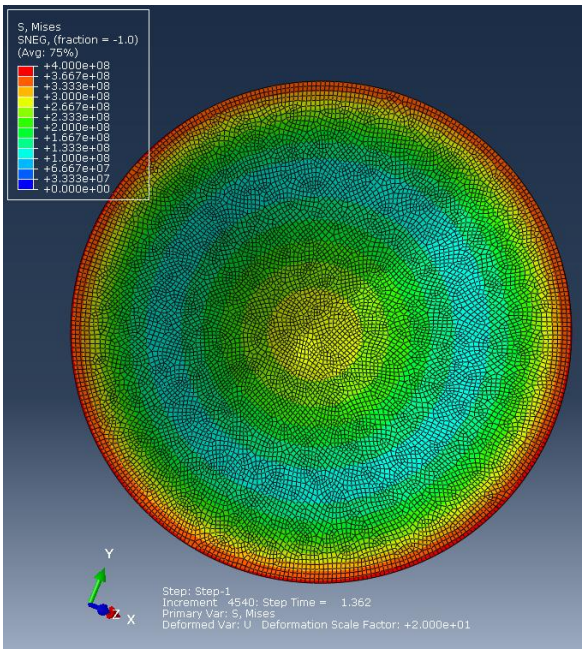

b)

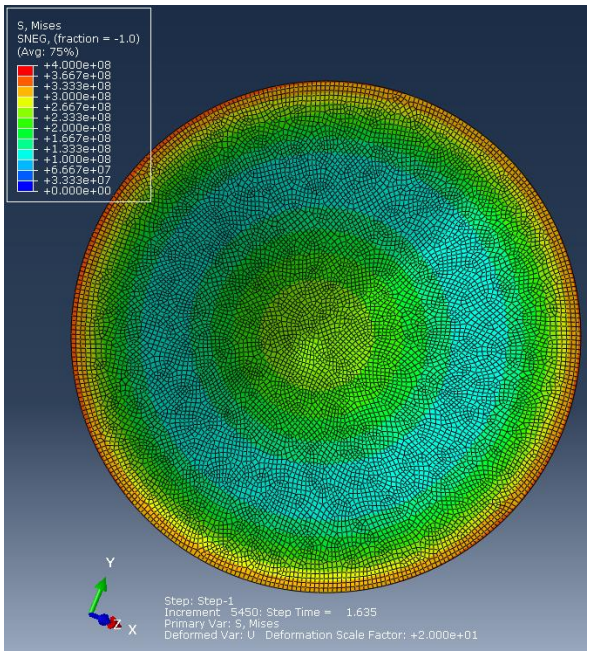

c)

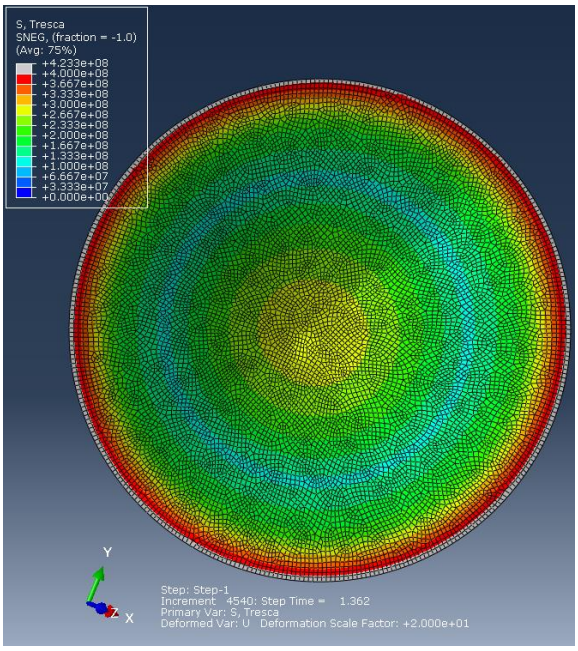

d)

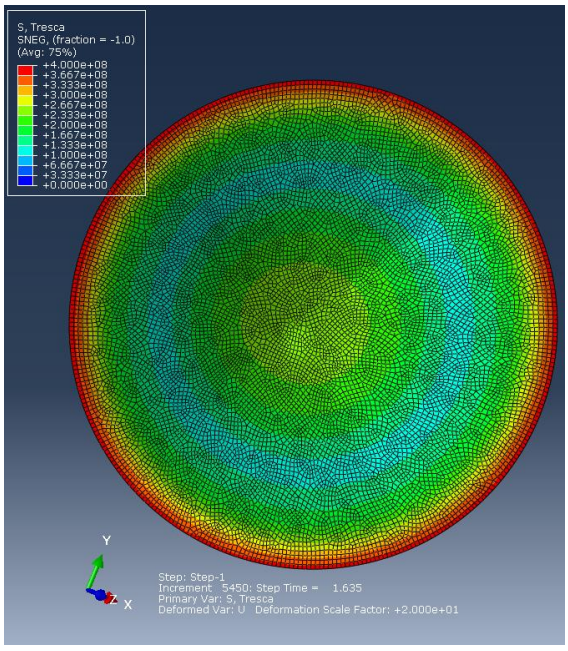

Figure 13.5: Stresses on the aft with a deformation scale of 20, where the grey area is above the ultimate strength, a) shows von-Mises stress at Δt = 1.362 s, b) shows von-Mises stress at Δt = 1.635 s, c) shows Tresca stress at Δt = 1.362 s, and d) shows Tresca stress at Δt = 1.635 s

Figure 13.5 shows the largest stresses of the two largest maximum von-Mises and Tresca stress peaks from Figure 13.4. It is seen that the largest stresses occur on the outer diameter of the lifeboats aft.

13.4 Displacements

In the same manner, as in section 10.3, the displacements are obtained from Abaqus with each unique node displacement with the same coordinate system, n_{nodes}, and the same nodes, 8726, 8741, 8757 and 8759.

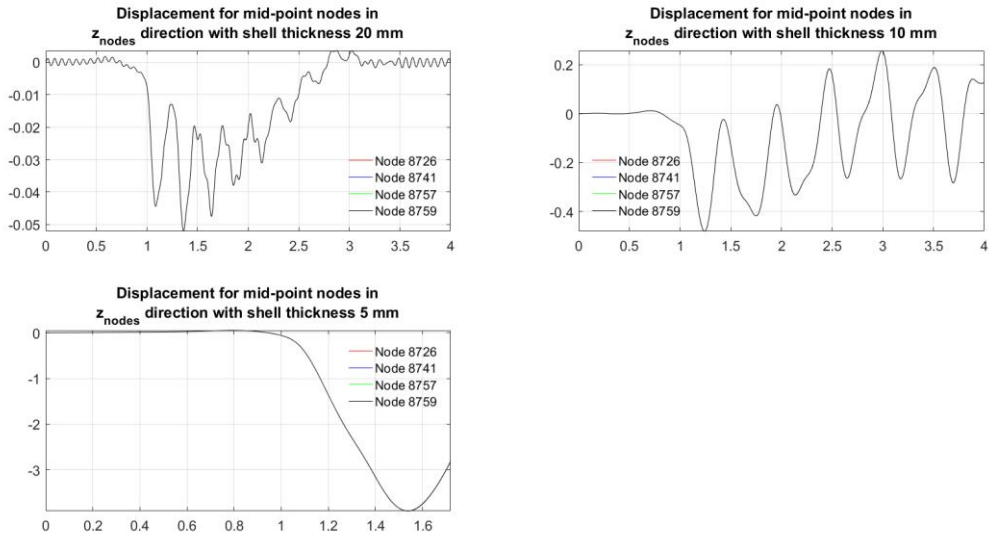

Figure 13.6: Displacements of node 8726, 8741, 8757 and 8759 for shell thickness 20 mm, 10 mm and 5 mm in z_{nodes} - direction

SHELL THICKNESS	**20 mm**	**10 mm**	**5 mm**
OSCILLATION PERIOD $[s]$	0.276	0.51	-
MAX DISPLACEMENT $[m]$	-0.0521	-0.4801	-3.9038
NODE 8726 $[m]$	-0.0521	-0.4799	-3.9008
NODE 8741 $[m]$	-0.0521	-0.4798	-3.9019
NODE 8757 $[m]$	-0.0521	-0.4799	-3.9038
NODE 8759 $[m]$	-0.0521	-0.4801	-3.9037

Table 13.1: Oscillation period and displacements measured in z_{nodes}, when the air is modelled as compressible

The increase in T_n, as seen in Table 13.1, compared with the eigenperiods in Table 8.6, is due to the increase in added mass from the air and water. The 20 mm shell thickness oscillates with the same

period as the force, which also indicates a more quasi-static solution than in section 10. As seen in Figure 13.7 the amount of water in the air bubble is different between the two air properties. The density of the air will change throughout the path of the lifeboat, when the air is modelled as compressible.

a) b)

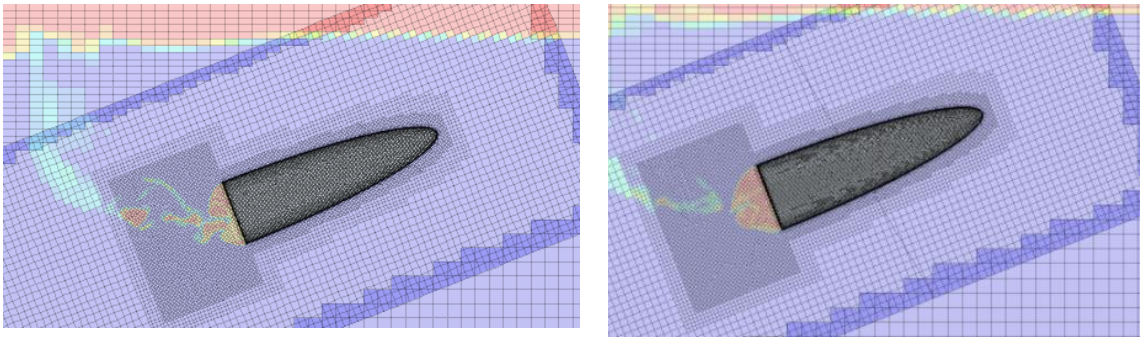

Figure 13.7: Shows the difference in the air bubble on the aft at solution time 1.3608 s where a) is with the air modelled as compressible and b) is the air is modelled as incompressible

Here the duration of the load, T_d, is taken as the time at 0.993 s until 1.245 s, which is 0.252 s, this gives the ratios of $\frac{T_d}{T_n}$ as seen in Table 13.2. This goes under the assumption that 0.993 s is the start of the wetting period and 1.245 s is the time where the second oscillation starts, where it is assumed that most of the aft is wetted.

SHELL THICKNESS	**20 mm**	**10 mm**
$\boldsymbol{T_d/T_n}$	0.913	0.494

Table 13.2: $\frac{T_d}{T_n}$ ratios for shell thicknesses with T_d period taken as 0.252 s when air is modelled as compressible

As seen in Table 13.2 the ratio, T_d/T_n, for shell thickness of 20 mm, is much larger than when air is modelled as incompressible, and by using Figure 9.2 it is possible to determine that hydroelastic effects are of low magnitude. While for shell thickness of 10 mm hydroelastic effects is of importance, but as seen in Table 13.1 the maximum displacement is over 0.22 m, and therefore not a realistic result.

14 Error sources

- Since it is used the overset mesh application in Star-CCM+ there could be interpolation errors due to the difference in cell size between the lifeboat, overset and the overlap.
- The boundary conditions in the FEM model has too large influence on specific parameters, such as Von-Mises and Tresca stress, as seen in Figure 10.4 and Figure 13.4, where the boundary conditions are included on the outer diameter. This results in larger stresses on the parts studied.
- The two distorted elements as mentioned in section 8.4 can have larger impact on the results then assumed.
- The Abaqus result files are extremely large, approximately 40Gb, which makes the post-processing hard. Therefore, post-processing scripts has been used to obtain displacements, forces, stresses etc. These post-processing scripts can have missed out on elements or nodes when creating outputs. In other words, typing mistakes.
- The dynamic effects are larger such that the quasi-static approach does not cover the full structural behaviour, and that the dynamic implicit quasi-static solver is not well documented such that the dynamic effects accounted for are not accurate.
- The Y^+ model, All Y^+, used will contribute to an uncertain result due to the unknown calculation method of Y^+ values.
- The use of different platforms, Linux or Windows, can affect the results obtained. This is mainly for where the mesh discretization Δx_3 has been used.
- By utilizing equation [50] the y_i and y_{i+n} is taken as average of the first and second oscillation. This was done to account for the hydrostatic pressure which makes the plate deformation in negative z_{nodes} direction larger than in the positive z_{nodes} direction. This will influence the response obtained from equation [48].

15 Conclusions and discussion

In the sensitivity analysis it was found good relations of number of inner iterations and time step corresponding to the mesh discretization's used. The convergence study shows a good order of accuracy in the global perspective, but for local quantities this was not the case. A considerable influence of this may be that the coarsest mesh discretization, Δx_3, was too coarse. By reducing the cell size to 0.10 m or 0.12 m the order of accuracy may have been improved. On the other hand, Δx_3 was very useful in the matter of getting results with low waiting period. Such that problems in the CFD simulations was discovered quickly, and with very low CPU cost connected to finding these problems.

The CFD simulation of the initial conditions for the lifeboat creates the same characteristic phenomena as a real lifeboat. This includes the air cavity formation, pressures, accelerations, velocity and trajectory. The air cavity formation is classified as a deep seal closure and since the air is modelled as incompressible the pressure from this closure creates an instant peak in the x_{body} acceleration and for the pressure on the aft. The duration of this impact is low, which means that it can be seen as an impulse for this condition. In the water exit phase the lifeboat experiences a second slamming, which is blunter than for the initial slamming in the water-entry phase. This is due to the pop-up height of 1.23 m, and this pop-up height corresponds well with theory. The lifeboat motion follows the preferred pattern, motion pattern 1, as suggested by DNV-GL.

The parameter investigation shows that the highest impact on focused results, such as accelerations, pressures, velocity and motion, is when the water entry velocity is changed. A change in ± 5 m/s, in the body fixed reference frame, created the highest and lowest values for air cavity closure time, x_{body} acceleration peak magnitude, angular acceleration in y_{body} - direction, pop-up height, water exit time, horizontal sailing distance and velocity at 6 s. The large angular acceleration for the highest velocity could result in a whiplash of the passengers as the seating arrangement is typically in the negative x_{body} - direction in a lifeboat.

The change in water entry angle shows greatest effect on the pressure on the aft. This is due to the large difference in submersion of the three conditions, whereas the hydrostatic pressure will influence the average pressure. The difference, with respect for the initial conditions, in submersion is -0.574 m and 0.993 m for the lowest and highest water entry level, respectfully.

The change in COG_z does not have much influence on most of the focused results. This indicates that the different weight distribution by passengers in z_{body} direction is not the most crucial factor in lifeboat diving.

Due to the unphysical large peak from the air cavity closure, when the air is modelled as incompressible, it is only the 20 mm shell which gives any indication of realistic results, even though the maximum von-Mises and Tresca stresses for this shell thickness is over the yield and ultimate strength. The three other shell thicknesses have too large stresses and displacement to be considered. As a result of the large von-Mises and Tresca stresses, and the large displacements, it is possible to conclude with that a filter of the forces mapped on the FEM model should be applied. This would filter out the large unrealistic effect of the air cavity closure when the air is modelled as incompressible. By using Figure 9.2, and the $\frac{T_d}{T_n}$ ratio of 0.404, it is seen that hydroelastic effects matter and that an hydroelastic analysis should be conducted. The maximum response, Figure 10.9, calculated with the particular solution, is much larger than the output from Abaqus, which supports the theory of the inertia term is not fully accounted for. But to get the most realistic results for the forces on the aft the air should be modelled as compressible, as Andrea Califano & Brinchmann (2013), and Vidar Tregde (2015) also concludes with.

As the results from the two-way couplings are very similar, but different from the results obtained by mesh discretization Δx_3 in the convergence study, it seems like the difference between a Linux based platform and Windows based platform can influence the results. This is because Vilje is Linux based, and it is where the two-way couplings have been solved, and the remote desktops at NTNU uses Windows, where Δx_3 has been solved. (IMT Software Wiki, 2014) This will also affect the order of accuracy as the difference for local values are affected, as seen in the figures from Star-CCM+ in section 11 and 12. By using the results as they are from Star-CCM+, with the two-way coupling, the displacements from the structure, aft and hull, have very little influence on the acceleration, pressure and trajectory. This indicates either that the hydroelastic effects has little contribution for the lifeboat dive, the inertia term has been supressed too much by the Abaqus solver, or that the displacements from the Abaqus model has not been used in the Star-CCM+ model. Without more tests of the two-way coupling it is hard to conclude with which of the three options are correct. As the displacements from Abaqus, for a shell thickness of 2.5 mm in the hull, had displacements up to 0.0155 m, it is expected that this would not give much influence on the results in Star-CCM+. While the displacements from the 20 mm shell thickness, in the two-way coupling, it was expected to have

an influence in the results. This can also be connected with the solver used in Abaqus, where the magnitude of the inertia term is unknown.

When calculating the stresses acting on the lifeboat hull it is seen that a quasi-static approach seems like an accurate method. By being conservative, and use the Tresca yield criterion, it is seen that a hull of 2.5 mm is not sufficient to withstand the forces from the water impact, where the splash crown creates large stresses on the hulls aft region.

As the air is modelled as compressible it is seen that the solution becomes more quasi-static, due to the ratio of T_d/T_n, the small difference between E_W and $E_W - E_K$ and that the displacements has the same tendency as the forces. By comparing the displacements in Figure 10.7 and Figure 13.6, it seen that the with incompressible air the displacements oscillates almost around zero, while with compressible air this is not the case. This indicates that the amount of water inside the air bubble when the air is modelled as incompressible is little, which implies that the aft oscillates almost in the same manner as if it was completely dry. When the air is modelled as compressible the aft has larger natural periods, which due to the added mass. By comparing the von-Mises and Tresca stresses, Figure 10.3 and Figure 13.4, between the two air properties, it is seen that the results are better for air modelled as compressible. Even though the results are of a more favourable magnitude the shell thickness of 20 mm still exceeds the ultimate strength by using Tresca yield criterion.

From all the structural results, it is seen that a minimum thickness of the hull should be 5 mm, while for the aft it should be above 20 mm. By applying stiffeners on the aft a thickness of 20 mm could be sufficient. It is also seen that a quasi-static approach for the aft and hull is sufficient, when the air is modelled as compressible for the aft and incompressible for the hull. The boundary conditions applied to the FEM model seems to have an influence on the yield criterions for the aft, while for the hull values they are more reasonable.

16 Further work

Due to assumptions and simplifications further work is necessary to capture more aspects around free-falling lifeboats.

Whereas the order of accuracy was not satisfactory, with respect to the local quantities, this should be redone. A suggested method is to have Δx_2 as the coarsest mesh and create a new mesh between Δx_1 and Δx_2. While the Δx_3 is only used for debugging the simulations.

As the incompressible air assumption for the parameter investigation gave good results, this should be done with compressible air as well. This gives also the opportunity to do a structural assessment of the forces on the aft.

Since the environmental conditions is often rough when it is necessary to use free-falling lifeboats, waves should be implemented into the simulations. This includes air modelled as incompressible and compressible, and structural assessment.

A parameter investigation of different geometries, such as longer, wider, heavier etc. This can give indications of favourable length over width ratios for lifeboats.

Use a fully dynamic solver for the FEM model, such that the full response of the structure from the forces is captured. This includes also a two-way coupling between the two programs when the air is modelled as compressible.

References

Bell, K., 2011. Matrisestatikk. I: *Matrisestatikk - Statiske beregninger av rammekonstruksjoner.* Trondheim: Tapir Akademiske Forlag, pp. 195-196.

Berchiche, N., Östman, A., Hermundstad, O. A. & Reinholdtsen, S.-A., 2015. *Experimental validation of CFD simulations of Free-Fall Lifeboats launches in Regular Waves,* s.l.: s.n.

Califano, A. & Brinchmann, K., 2013. *Evaluation of Loads During a Free-Fall Lifeboat Drop,* s.l.: ASME.

Case, J., Chilver, L. & Ross, C. T. F., 1999. Strength of materials and structures. I: s.l.:Butterworth-Heinemann, pp. 144-149.

Colicchio, G., Greco, M. & Faltinsen, O. M., 2006. *A BEM-level set domain-decomposition strategy for non-linear and fragmented interfacial flows,* s.l.: INTERNATIONAL JOURNAL FOR NUMERICAL METHODS IN ENGINEERING.

Consultance, M., 2017. *Marin Consultance.* [Internett]
Available at: http://www.mcl.co.tt/product/norsafe-free-fall-lifeboat/

DNV-GL, 2010. *Environmental Conditions and Environmental Loads,* s.l.: s.n.

DNV-GL, 2016. *Design of free-fall lifeboats,* s.l.: DNV-GL.

Engineering ToolBox, u.d. *Engineeringtoolbox.* [Internett]
Available at: http://www.engineeringtoolbox.com/fluid-density-temperature-pressure-d_309.html
[Funnet 01. May 2017].

Faltinsen, O. M., 1990. *SEA LOADS ON SHIPS AND OFFSHORE STRUCTURES.* s.l.:Cambridge university press.

Faltinsen, O. M., 2005. *Hydrodynamics of High-Speed Marine Vehicles.* s.l.:Cambridge University Press.

Faltinsen, O. M. & Greco, M., 2013. *CFD and Wave and Current Induced Loads on Offshore.* s.l.: NTNU.

Faltinsen, O. M. & Timokha, A. N., 2009. *Sloshing.* s.l.:Cambridge university press.

Fouques, S. et al., 2013. *Establishment of Operational Criteria for Safe Launch of Free-Fall Lifeboats from a Turret-Moored FPSO,* s.l.: s.n.

Fouques, S. & Hermundstad, O. A., 2016. *Structural Integrity Assessment of Free-Fall Lifeboats by combining fast Monte-Carlo simulations with CFD by means of Proxy Load variables,* s.l.: ASME.

Fouques, S. et al., 2014. *Human Injury probability dyring water entry of Free-Fall Lifeboats: Operational Criteria based on Long-Term simulations using Hindcast Data,* s.l.: s.n.

Gekle, S. et al., 2008. *Noncontinous Froude Number Scaling for the Closure Depth of a Cylindrical Cavity ,* s.l.: The American Physical Society.

Greco, M., 2012. *TMR4215 - Sea Loads - Lecture Notes,* s.l.: s.n.

Hirt, C. W. & Nichols, B., 1979. *Volume of fluid (VOF) Method for the dynamics for free boandaries ,* Los Alamos: Los Alamos Scientific Laboratory .

IMT Software Wiki, 2014. *Tips and tricks.* [Internett]
Available at: http://www.ivt.ntnu.no/imt/software/tips_and_tricks
[Funnet May 2017].

J. Andreson, G. D. J. D. E. D. R. G. J. V., 2009. *Computional Fluid Dynamics.* Berlin: Springer.

Jin, J., Ringen, E. & Reinholdtsen, S.-A., 2014. *Forward Distance Performance of a Free Fall Lifeboat in a Seaway,* s.l.: ISOPE.

Kim, G.-H. & Park, S., 2016. *Development of numerical simulation tool for efficient and robust prediction of ship resistance,* s.l.: International Journal of Naval Architecture and Ocean Engineering.

Larsen, C. M., 2016. *Marin Dynamikk.* 5. red. s.l.:NTNU.

Luxcey, N. et al., 2014. *Influence of Wave-induced Skid Mtions on the launch of Free-Fall skid Lifeboats from Floating Hosts: Experimental and Numerical investigations,* s.l.: s.n.

Mathisen, K. M., 2016. *Lecture Notes.* s.l.: s.n.

NTNU HPC Group, 2016. [Internett]
Available at: https://www.hpc.ntnu.no/display/hpc/About+Vilje

Ommundsen, A., 2014. *Air Cavity Dynamics of Free Fall Lifeboats: Hydrodynamic Study,* s.l.: s.n.

Oñate, E., 2009. *Structural Analysis the Finite Element Method.* Vol. 1 red. s.l.:Springer.

Reuben, R., 1994. Materials in Marine Technology. I: s.l.:Springer-Verlag, p. 29.

Sauder, T. et al., 2014. *Effect of Wind Loads on the performance of Free-Fall Lifeboats,* s.l.: s.n.

Sauder, T. & Fouques, S., 2009. *Theoretical Study of the Water Entry of a Body in Waves. Application to Safety of Occupants in Free-Fall Lifeboats,* s.l.: s.n.

Simulia - Abaqus 6.14, 2014. *Abaqus Analysis User's Guide.* [Internett]
Available at: http://abaqus.software.polimi.it/v6.14/books/usb/default.htm
[Funnet May 2017].

Simulia - Abaqus 6.14, 2016. *Theory Guide.* [Internett]
Available at: http://50.16.225.63/v6.14/books/stm/default.htm
[Funnet May 2017].

Simulia, 2014. *Abaqus 6.14 Verification Guide.* [Internett]
Available at: http://129.97.46.200:2080/v6.14/books/ver/default.htm
[Funnet 08 May 2017].

Steve CD adapco, 2016. *User guide Star-CCM+ version 11.06,* s.l.: https://stevedocs.cd-adapco.com/starccmplus_latest_en/index.html?param=gYuRe#page/STARCCMP%2FGUID-899D7E79-198D-4E90-B064-F085542B954F%3Den%3D.html%23.

Svendsen, A. G., 2017. *Hydrodynamic effects relevant for free falling lifeboat modelled with compressible air,* s.l.: NTNU.

Tregde, V., 2015. *Compressible Air Effects in CFD Simulations of Free Fall Lifeboat Drop,* s.l.: s.n.

Truscott, T. T., Epps, B. P. & Belden, J., 2013. *Water Entry of Projectiles,* s.l.: s.n.

Truscott, T. T., Epps, B. P. & Munns, R. H., 2016. *Water exit of buoyant spheres,* s.l.: American Physical Society .

White, F. M., 2006. *Viscous fluid flow.* Singapore: McGraw-hill companies .

Yan, H., Liu, Y., Kominiarczuk, J. & Yue, D. K. P., 2009. *Cavity dynamics in water entry at low Froude numbers,* s.l.: Cambridge university.

Ytrehus, T., u.d. *The gouverning conservation equations in fluid mechanics,* Trondheim: NTNU.

Appendix

See electronic attachment for the input files used for the FEM model with a shell thickness of 20 mm, for aft and hull.